This electronic thesis or dissertation has been downloaded from the King's Research Portal at https://kclpure.kcl.ac.uk/portal/

# NOVEL ANTENNA DESIGNS FOR BODY-CENTRIC APPLICATIONS

Yeboah-Akowuah, Bright

*Awarding institution:*
King's College London

**The copyright of this thesis rests with the author and no quotation from it or information derived from it may be published without proper acknowledgement.**

END USER LICENCE AGREEMENT

**Unless another licence is stated on the immediately following page** this work is licensed

under a Creative Commons Attribution-NonCommercial-NoDerivatives 4.0 International

licence. https://creativecommons.org/licenses/by-nc-nd/4.0/

You are free to copy, distribute and transmit the work

Under the following conditions:

- Attribution: You must attribute the work in the manner specified by the author (but not in any way that suggests that they endorse you or your use of the work).
- Non Commercial: You may not use this work for commercial purposes.
- No Derivative Works - You may not alter, transform, or build upon this work.

Any of these conditions can be waived if you receive permission from the author. Your fair dealings and other rights are in no way affected by the above.

**Take down policy**

If you believe that this document breaches copyright please contact librarypure@kcl.ac.uk providing details, and we will remove access to the work immediately and investigate your claim.

Download date: 05. May. 2023

King's College London

PhD Thesis

# NOVEL ANTENNA DESIGNS FOR BODY-CENTRIC APPLICATIONS

*Author:*
BrightYeboah-Akowuah

*Supervisors:*
Dr. Kosmas Panagiotis
Dr. Efthymios Kallos

*A report submitted in fulfilment of the requirements for the degree of Doctor of Philosophy (PhD)*

*in the*

Centre for Telecommunications Research
School of Natural and Mathematical Sciences

February 2017

# Declaration of Authorship

I, BrightYeboah-Akowuah, declare that this thesis titled, 'NOVEL ANTENNA DESIGNS FOR BODY-CENTRIC APPLICATIONS' and the work presented in it are my own. I confirm that:

- This work was done wholly or mainly while in candidature for a research degree at this University.
- Where any part of this thesis has previously been submitted for a degree or any other qualification at this University or any other institution, this has been clearly stated.
- Where I have consulted the published work of others, this is always clearly attributed.
- Where I have quoted from the work of others, the source is always given. With the exception of such quotations, this thesis is entirely my own work.
- I have acknowledged all main sources of help.
- Where the thesis is based on work done by myself jointly with others, I have made clear exactly what was done by others and what I have contributed myself.

Signed: 

Date: 06 th February 2017

# *Abstract*

There is an increasing need for small, conformal and multifunctional antennas that can satisfy all sorts of communication needs and varieties of portable devices and sensors for monitoring and information gathering. One area that has received much attention in recent years include antennas for body-centric applications that can be integrated into body-worn and implantable medical devices (IMDs). Continuous reduction in size for body-worn and IMDs require ultra-small antennas for embedded applications. However, the designers of body-centric antennas are faced with numerous challenges in dealing with issues related to miniaturisation, biocompatibility, patient safety, detuning and additional challenges imposed by the human body, which significantly affects the performance of the antennas. In order to have efficient wireless communication systems, it is important to understand and characterise the effects of the human body on antenna elements, the radio propagation channel parameters and the overall system performance.

The thesis is focused on design and development of antennas for body-centric applications, which involve on-body, off-body and implantable devices. Numerical simulations of the proposed antennas on human tissue-mimicking materials (phantom) were performed to determine how the human tissues affect the antenna performance. A series of measurements have been made on human body phantom made in the laboratory as well as real on-body human subject applications.

Based on the numerical and statistical data obtained from these studies various antenna designs have been proposed for body-centric applications including applications in implantable devices in the Medical Implant and Communication Service band (MICS) 402-405 MHz, on-body applications in the Industrial, Scientific and Medical (ISM) band at 2.45 GHz and Ultra-wideband (UWB) spectrum 3.1 GHz - 10.6 GHz for on-body and microwave imaging applications.

# *Acknowledgements*

First and foremost, I want to thank the almighty God for giving me the strength to complete this study. As I believe God is a spirit and His works manifest through mankind, hence my sincere appreciation and profound gratitude to my supervisors, Dr. Kosmas Panagiotis and Dr. Efthymios Kallos for their invaluable contributions, patience and assistance towards this work. This study would not have been successful without the major roles played by my supervisors. Many thanks also go to my colleagues especially Syed Ahsan for his fruitful suggestions and discussions during the course of this study.

Another appreciation goes to Prof. Yifan Chen and his staff of South University of Science and Technology of China (SUSTC) for hosting me for a whole month in China. I also acknowledge my sponsor STSM COST Action that paid for the trip and made it possible for me to carry out antenna measurements in China.

Last but not the least thanks go to my family who had to endure my absence for some time during the course of my studies. The continuous prayers and care showed by my family provided me with the needed strength to complete this study.

# Contents

# List of Figures

# List of Tables

# Abbreviations

| | |
|---|---|
| **AIMD** | Active Implantable Medical Device |
| **BCWC** | Body-centric Wireless Communication |
| **CPW** | Coplanar Waveguide |
| **CS MSA** | Circular Slot Microstrip Antenna |
| **CST** | Computer Simulation Technology |
| **dB** | Decibel |
| **EBG** | Electron Band Gap |
| **ERP** | Effective Radiated Power |
| **ETSI** | European Telecommunication Standards Institute |
| **FCC** | Federal Communications Commission |
| **FDTD** | Finite-Difference Time-Domain |
| **FIT** | Finite Integral Technique |
| **HIPERLAN** | High Performance Local Area Network |
| **IMDs** | Implantable Medical Devices |
| **ISM** | Industrial , Scientific and Medical |
| **ITU-R** | International Telecommunication Union- Recommendations |
| **MICS** | Medical Implant and Communication Service |
| **PIFA** | Planar inverted-F Antenna |
| **PSD** | Power Spectral Density |
| **Rx** | Receiver |
| **SAR** | Specific Rate Absorption |
| **Tx** | Transmitter |
| **UWB** | Ultra Wideband |
| **VNA** | Vector Network Analyser |
| **VSWR** | Voltage Standing Wave Ratio |
| **WBAN** | Wireless Body Area Network |
| **WLAN** | Wireless Local Area Network |
| **WCE** | Wireless Capsule Endoscopy |
| **WPAN** | Wireless Personal Area Network |

*Dedicated to my children William Yeboah-Akowuah, Bright Yeboah-Akowuah (Junior), Felicia Yeboah-Akowuah and the triplets (David, Daniel and Danny Yeboah-Akowuah)*

Portions of the work detailed in this thesis have been presented in international conference and scholarly publications, as follows:

1. **B. Yeboah-Akowuah**, P. Kosmas and Y. Chen, "A low profile microstrip patch antenna for body-centric communications at 2.45 GHz band,"2015 9th European Conference on Antennas and Propagation (EuCAP), Lisbon, 2015, pp. 1-3.

2. **B. Yeboah-Akowuah**, P. Kosmas and Yifan Chen, "Compact UWB antenna array for microwave imaging," 2015 9th European Conference on Antennas and Propagation (EuCAP), Lisbon, 2015, pp. 1-3.

3. W. Yamada, M. Sasaki, T. Sugiyama, O. Holland, S. Ping, **B. Yeboah-Akowuah**, J. Hwang and H. Aghvami "Indoor propagation model for TV white space," Cognitive Radio Oriented Wireless Networks and Communications (CROWNCOM), 2014 9th International Conference , Oulu, 2014, pp. 209-214.

4. **B. Yeboah-Akowuah**, E. Kallos, G. Palikaras, Y. Chen and P. Kosmas, "A novel compact Planar Inverted-F Antenna for biomedical applications in the MICS band," Antennas and Propagation (EuCAP), 2014 8th European Conference , The Hague, 2014, pp. 822-824.

5. S. Ahsan, **B. Yeboah-Akowuah**, P. Kosmas, H.C. Garcia, G. Palikaras, and E. Kallos "Balanced Antipodal Vivaldi Antenna for microwave tomography," Wireless Mobile Communication and Healthcare (Mobihealth), 2014 EAI 4th International Conference , Athens, 2014, pp. 316-319.

6. **B. Yeboah-Akowuah**, P. Kosmas and Y. Chen, "A Q-Slot Monopole for UWB Body-Centric Wireless Communications," IEEE Transactions on Antennas and Propagation. Accepted on (30/11/2016)

# Chapter 1

# Introduction

Emerging wireless technologies and applications are making great impacts on our lives for the past two decades or so. One of the challenges many people face around the world is the issue of mobility owing to poor health conditions. To make matters worse, it is more difficult to continuously monitor people round the clock especially those with long-term health conditions. With the widespread use of portable devices such as smartphones and smart wearable watches the concept of collecting personal data in those devices becomes more realistic to support remote monitoring services. These devices could perform various preventive functions to maintain and improve lives through variety of communication links. It has become imperative to establish reliable communication links with such devices for various purposes.

It is expected that remote monitoring technologies using wireless sensors and wearable devices will be deployed in the near future to provide services such as diabetes care, high blood pressure, cardio-vascular diseases and care for the aged. The current monitoring systems made available by many service providers use basic manual infrastructure where in most cases customers or patients manually collect data and send them to providers. Besides the healthcare applications of sensors and wearable devices, there are other areas such as sports, military and agriculture that have been identified to benefit from body-centric technology. In all cases, the future sensor networks and wearable devices are expected to automatically collect physiological data and transmit them over communication interfaces.

One of the key components of any wireless system involves the use of an antenna to transfer or receive electromagnetic waves in free space or in a particular medium. Traditionally most antennas are designed to operate in free space, but the emergence of wireless technologies have led to a lot of on-going research activities to design antennas for on-body and implantable medical devices (IMDS) [1–4]. These antennas are intended for for body-worn devices and embedded applications inside the human body, therefore, it is necessary to model and characterise such antennas for such applications.

Human body and its associated tissues are sometimes described as hostile and difficult environment for body-centric devices and for that matter the antenna element. The

human body is a very complex structure, dispersive and highly lossy that affects the performance of antennas. Due to the complex nature of human tissues, designing body-centric antennas for on-body and embedded applications or any other application where the antenna is in close proximity to the human body pose great challenges and difficulties for antenna designers. It is, therefore, imperative to understand the true impact of biological tissues on body-centric antennas.

In recent years many patch antennas in various configurations have been proposed for body-centric applications. However, some of these antennas are too big to be considered for wearable and implantable devices. For this study, novel ways of designing miniaturised antennas without compromising the performance such as gain and radiation efficiency will be investigated. For instance, the proposed Compact Spiral PIFA has overall volume of 251 $mm^3$ which is a reduction of about 97% compared to the reported work in [5] with a volume of 10240 $mm^3$ and also a third of recently reported PIFA with volume of 692 $mm^3$ [6], and half a fraction of 458 $mm^3$ reported in [7]. In addition to designing compact antennas for these operation bands, the study presents optimal designs with respect to important antenna metrics such as radiation efficiency and gain, as well as biocompatibility, bandwidth, and time-domain stability for UWB operation.

The motivation of this study stems from the fact that reliable, miniaturised, low-power, portable and off the shelf antennas can play crucial roles in supporting body-centric applications.

## 1.1 Research Objectives

The primary aim of this study focuses on the design of low profile antennas for body-centric communications i.e in-body communication, off-body communication and on-body communication. The aims of the study are achieved through numerical simulations and investigations, experimental characterisation and analysis of the antenna elements proposed. The main objectives of the study include:

Designing novel antennas that are ultra small, efficient and stable for body-centric applications, which operate in the following bands:

- MIC band (402-405 MHz)→ In-body communication (implantable devices)
- ISM band (2.45 GHz)→ On-body communication (wearable devices)
- UWB (3.1-10.6 GHz)→ On-body and off-body communications (Wearable devices and microwave imaging)

- Investigating the performance of body-worn antennas with respect to body positions to establish reliable communication links for body-centric communication.

- To design printed monopoles for on-body and microwave imaging applications.

- Provide antenna design guidelines for narrowband and ultra-wideband for body-centric wireless communications.

- To evaluate the performance of implantable antennas in human mimicking phantom to establish the influence of body tissues on antenna parameters.

## 1.2 Organisation of the thesis

The rest of the thesis is organised as follows :

Chapter **2** Presents literature review and the fundamentals of antenna theory. It starts with the review of the state-of-the-art of body-centric antennas that include medical implantable communication service (MICS) band, ultra wideband (UWB) and industrial, scientific and medical (ISM) band. It then follows with the background information and fundamental parameters use to access the quality of antennas.

Chapter **3** introduces a new printed rectangular monopole antenna (PRMA) with Q-slot designed for operations in UWB spectrum (3.1 - 10.6 GHz). The chapter also assesses the performance of the antenna for on-body and microwave imaging applications. The frequency and time-domain characteristics of the antenna are also presented. The antenna was also characterised based on several spatially dependent metrics such as fidelity and impulse response.

Chapter **4** presents two UWB monopoles for microwave imaging application. The chapter also provides design guidelines and optimisation of the antenna. Experimental studies and results in the form of array are presented.

Chapter **5** presents an ISM band 2.45 GHz antenna for wearable applications. The chapter provides parametric studies of the antenna and means to control its resonant frequency with a circular slot. Experimental results on real human subjects have been presented.

Chapter **6** introduces two implantable antennas in different configurations designed to operate in MICS band (402 - 405 MHz). The chapter provides techniques of designing miniaturised antennas for implantable devices. The chapter also discusses the operation

principles of the proposed antennas. The goal is to propose implantable antennas and design techniques that can be exploited by other researchers in the future.

Chapter **7** provides the conclusion and the main contributions as well as the findings of this study. It will also provides future works and suggestions that could be taken into consideration to further the subject and the knowledge of body-centric antennas and applications.

# References


[1] K. Jaehoon and Y. Rahmat-Samii, "Implanted antennas inside a human body: simulations, designs, and characterizations," *Microwave Theory and Techniques, IEEE Transactions*, vol. 52, pp. 1934–1943, 2004.

[2] P. Soontornpipit, C. M. Furse, and C. Y. Chung, "Design of implantable microstrip antenna for communication with medical implants," *Microwave Theory and Techniques, IEEE Transaction*, vol. 52, pp. 1944–1951, 2004.

[3] A. Kiourti, J. R. Costa, C. A. Fernandes, A. G. Santiago, and K. S. Nikita, "Miniature implantable antennas for biomedical telemetry: from simulation to realization," *IEEE Trans Biomed Eng*, vol. 59, pp. 3140–7, Nov 2012.

[4] M. L. Scarpello, I. Kazani, C. Hertleer, H. Rogier, and D. V. Ginste, "Stability and efficiency of screen-printed wearable and washable antennas," *Antennas and Wireless Propagation Letters,IEEE*, vol. 11, pp. 838–841, 2012.

[5] Y. Rahmat-Samii, "Wearable and implantable antennas in body-centric communications," in *Antennas and Propagation, 2007. EuCAP 2007. The Second European Conference on*, pp. 1–5, Nov 2007.

[6] C. Liu, Y. X. Guo, and S. Xiao, "Compact dual-band antenna for implantable devices," *IEEE Antennas and Wireless Propagation Letters*, vol. 11, pp. 1508–1511, 2012.

[7] L. Xu, Y. Guo, and W. Wu, "Dual-band implantable antenna with open-end slots on ground," *IEEE Antennas and Wireless Propagation Letters*, vol. 11, pp. 1564–1567, 2012.

# Chapter 2

# Literature Review of Body-Centric Wireless Communication

## 2.1 Body-Centric Wireless Communication

Body-centric wireless communications (BCWC) incorporate a number of important technologies in the design process ranging from antenna designs, biosensors, integrated circuits and portable systems. The body-centric networks are aimed at providing wireless connectivity between human body and the surroundings through wearable and implanted antennas. BCWC is expected to be part of future fourth-generation mobile communications systems and natural progression of body-area networks (BANs) and personal area net works (PANs) [1, 2].

Body-centric communications can be classified into three main domains (Fig 2.1) i.e in-body, on-body, and off-body. In-body communications take place between medical implants and sensor networks. On-body communications take place between wireless communication link within on-body networks and wearable systems. The off-body communications take place from off-body to an on-body device or system, for example, human-to-human or human-to-base units.

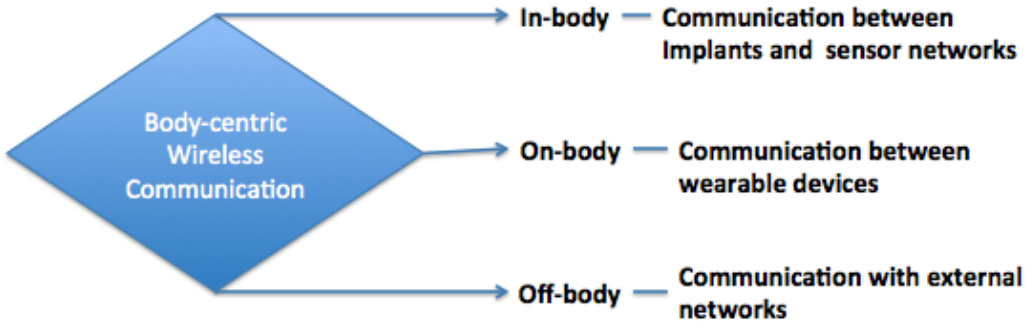


FIGURE 2.1: Domains of body-centric wireless communication.

In practice, an integrated system utilises all three classes of body-centric communication, and strict boundaries between them may not be established. Antennas and propagation are the most basic points for body-centric wireless communications. We will review antennas for body-centric communications in the subsequent sections.

## 2.2 Review of Antennas for Medical Implantable Communication Service (MICS) Band

The International Telecommunication Union-Recommendations (ITU-R) allocated the frequency band of 402-405 MHz for implant devices in 1998 [3]. The standard for MICS is defined by Federal Communications Commission (FCC) in USA [4] and European Telecommunication Standards Institute (ETSI) [5]. The policy document primarily defines two applications for MICS, communication between a base station and an implanted device and communication between medical implants within the same body.

For effective MICS operations, the regulatory bodies recommend the effective isotropic radiated power (EIRP) in the range of -20 dBm (10 $\mu$W) to -16 dBm (25 $\mu$W), which assumes that the transmit power is radiated equally in all directions by the transmitter. Thus an amount of power emitted from an isotropic antenna to obtain the same power density in the direction of the antenna pattern peak with gain $G_t$. EIRP is simply the gain of the transmitting antenna multiplied by the net power accepted by the antenna from the connected transmitter as illustrated in Fig. 2.2 [6]. As shown, the maximum radiation intensity $U_m$ from a transmitting antenna with input power $P_t$ is in the direction of maximum radiation, with the gain $G_t$:

$$G_t = \frac{4\pi U_m}{P_t} \tag{2.1}$$

$$EIRP = \frac{P_t 4\pi U_m}{P_t} = 4\pi U_m \tag{2.2}$$

$$EIRP = P_t G_t \tag{2.3}$$


(*a*) Directional antenna with input power $P_t$ and gain $G_t$.

(*b*) Isotropic antenna with input power $P_tG_t$ and unity gain.

FIGURE 2.2: Illustration of EIRP. In both case, EIRP $= 4\pi U_m$ [6].

Many applications employ implantable antennas, for example, wireless capsule endoscopy (WCE) and glucose monitoring of people with diabetes as shown in Fig. 2.3 [7, 8]. For the wireless capsule endoscopy, the system consists of several components including an antenna/transmitter which transmits the capsule recorded images to the belt-pack receiver. The glucose monitoring device offers non-invasive measuring of blood sugar level without the need to piece the skin and possibly send the results to an external unit, a technology being developed by MediWise UK [8]. Furthermore, in [9], a circumference antenna, which is a monopole antenna that is mounted around the edge of the pacemaker case has been used for cardiac devices as shown in Fig. 2.4.

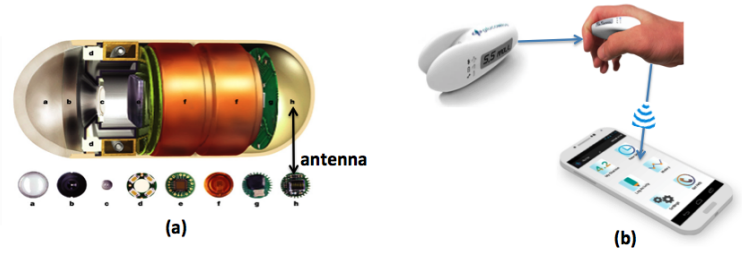


FIGURE 2.3: (a) Wireless endoscope capsule system [7] (b) Blood glucose level monitoring system [8] .

FIGURE 2.4: Circumference antenna on a pacemaker [9] .

The current progress and achievements of implantable medical devices (IMD) employ different types of antennas designed to meet the regulatory standards and also to provide wireless biomedical telemetry. The current approach uses inductive link and radio-frequency to provide biomedical communications [10–12]. The disadvantage of the existing approach is low data rate, short range communication channel and close contact of the patient's body near the internal coil. Current research activities are oriented towards radio frequency-linked (RF-link) implantable medical devices [13–24].

Various regular shaped configurations such as circular, square and spiral planar inverted-F antenna (PIFA) have been reported in the literature [21, 25–28] as shown in Fig. 2.5. The recent developments are geared towards antennas that can operate in both MICS and ISM bands. For example, in [29] a dual band implantable antenna operating at MICS band 402 MHz and ISM band 2.4 GHz has been proposed (See Fig. 2.6).

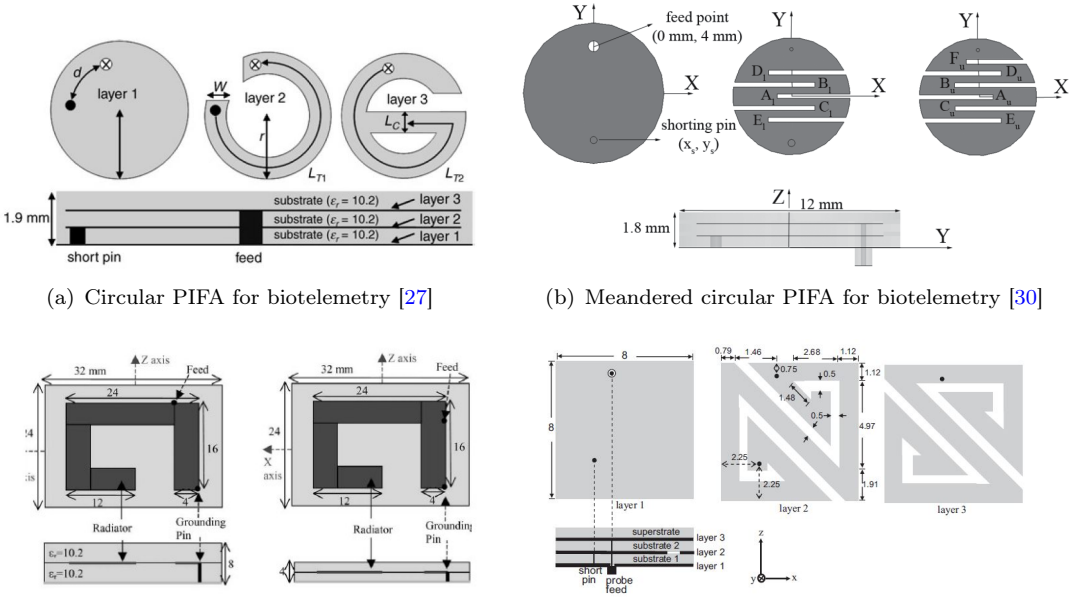


(a) Circular PIFA for biotelemetry [27]

(b) Meandered circular PIFA for biotelemetry [30]

(c) Spiral PIFA for implantable device [25]

(d) Implantable stacked PIFA for MICS band [28]

FIGURE 2.5: Examples of Implantable PIFAs for biotelemetry available in the open literature.

In [6, 31, 32], it has been established that the resonant length of a microstrip patch antenna is approximately half wavelength at the operating frequency. However, in [25, 26, 33], the studies show that using planar inverted-F antenna (PIFA), resonant length could be reduced to a quarter wavelength. For this study we will consider PIFA for implantable applications which will be the subject of discussion in chapter **6**. PIFA provides compactness and miniaturisation techniques suitable for implantable applications.

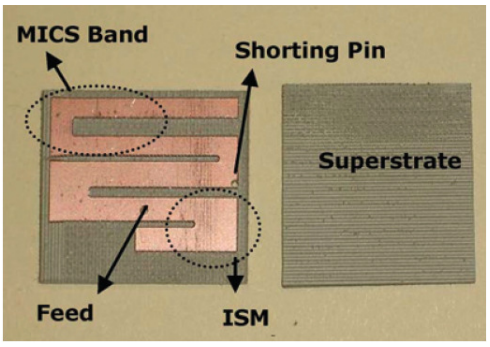


FIGURE 2.6: Dual band implantable antenna operating at 402 MHz and 2.4 GHz proposed in [29].

## 2.3 Review of Industrial, Scientific and Medical Band (ISM) Antennas for Body-centric Communication

The industrial, scientific and medical (ISM) radio bands are unlicensed bands for many communication devices such as bluetooth, household microwave ovens and other short-range wireless devices. Depending on the regional regulations, different countries use different ISM radio frequency for communication as shown in Table 2.1 [34] . For example, these frequencies 433.1-434.8 MHz, 868-868.6 MHZ are only available in Europe. Other frequencies such as 608-614 MHz and 1395-1400 MHz are available in United States (U.S). The most commonly use frequency worldwide is 2.4 GHz.

TABLE 2.1: ISM Communication Standards [34]

| Frequency range (MHz) | | Bandwidth | Centre frequency | Availability |
|---|---|---|---|---|
| 6.765 | 6.795 | 30 kHz | 6.780 MHz | Subject to local acceptance |
| 13.553 | 13.567 | 14 kHz | 13.560 MHz | Worldwide |
| 26.957 | 27.283 | 326 kHz | 27.120 MHz | Worldwide |
| 40.660 | 40.700 | 40.700 MHz | 40 kHz | Worldwide |
| 433.050 | 434.790 | 434.790 MHz | 1.74 MHz | Europe,Africa,Middle East |
| 902 | 928 | 928.000 MHz | 26 MHz | Americas,Greenland, and Pacific Island |
| 2400 | 2425 | 2.5 GHz | 100 MHz | Worldwide |
| 5725 | 5875 | 5.875 | 150 MHz | Worldwide |
| 24000 | 24250 | 250 MHz | 24.125 MHz | Worldwide |
| 61000 | 61500 | 500 MHz | 61.250 GHz | Subject to local acceptance |
| 122000 | 123000 | 1 GHz | 122.500 GHz | Subject to local acceptance |
| 244000 | 246000 | 246 GHz | 2 GHz | Subject to local acceptance |

Of late the ISM bands have been shared with other technologies such as wireless local area network (WLAN), ZigBee, high performance radio local area network ((HIPERLAN), IEEE 802.1/Wi-fi and wireless personal area network (WPAN) based on IEEE 802.15 standard. For WPAN, the aim is to facilitate network for interconnecting devices centred around home or business systems. The newest technology to use the ISM band is z-waves

designed to provide low-power and high data rate transmission in consumer and other commercial products [35–37].

Significant increase in the use of bluetooth, WLAN as well as ZigBee technologies for body-worn devices necessitate the design of antennas that can provide different performance and possibly multi-band functionalities. Many studies have been conducted on the operations of antennas located in close proximity of the body [38–42]. For many applications, printed antennas provide some desirable features such as physical robustness, ease of construction and integration, low cost and in some cases conformity. Extensive studies conducted in [43, 44] for on-body applications using monopole antennas show good performances with respect to path loss, due to their omnidirectional radiation patterns.

Recently, one area that has received much attention is the integration of wireless devices in garments. In [45], a textile wearable dipole antenna has been proposed. Also in [46], a patch antenna printed on a flexible pad of foam was integrated into protective clothing for fire-fighters. In all cases, this off-body communication requires the development of suitable antennas that combine flexibility with robustness and reliability and also to reduce the radiation towards the human body and minimise detuning. To reduce the effect of human body on the antenna, electro-textiles i.e electrically conductive textiles for flexible integration with clothing have been proposed [47, 48]. Furthermore, Langley *et.al* [49], proposed a flexible dual-band patch antenna (2.45 and 5.80 GHz) printed on an Electromagnetic Band Gap (EBG) textile substrate (See Fig. 2.7) with the results demonstrating a reduction in of radiation into the body.

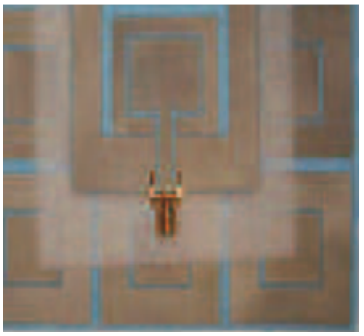

FIGURE 2.7: Dual-band coplanar antenna on EBG plane [49].

Although significant progress has been made for narrowband antennas, more especially at ISM band 2.45 GHz, some of the proposed antennas are too big for practical applications and also no easy mechanisms to control their properties. Furthermore, a complete parametric study addressing the effects of the human body on the performance parameters for a wider number of antennas are required in order to understand what are the requirements to design suitable antennas for body-centric wireless communications.

For this study we propose a very simple structure that operates at ISM band 2. 45 GHz with an easy mechanism to control its resonant frequency. The proposed structure also show resilient in the close proximity to human body.

## 2.4 Review of Ultra-Wideband (UWB) Antennas for Body-Centric Communicaion

On 14th February, 2002 the Federal Communications Commission (FCC) of U.S.A approved unlicensed use of UWB spectrum 3.1 GHZ- 10.6 GHz and released it on 22nd April, 2002 [50]. In the first report, FCC Part-15 rule defined UWB as a system with bandwidth greater than 500 MHz or the relative bandwidth should be 20% more than the centre frequency. The Commission also defines a UWB device as any device where the fractional bandwidth is greater than 0.25 or occupies 1.5 GHz or more of spectrum. The formula proposed by the Commission for calculating fractional bandwidth is (2.4):

$$FWB = \frac{2(f_H - f_L)}{f_H + f_L} \tag{2.4}$$

where $f_H$ is the upper frequency of the -10 dB emission point and $f_L$ is the lower frequency of the -10 dB emission point. The centre frequency of the transmission was defined as the average of the upper and lower -10 dB points, i.e., $\frac{(f_H+f_L)}{2}$.

The order establishes technical standards for three types of UWB devices :

1. Imaging systems that include;
   (i) Ground penetrating radar, wall imaging and medical imaging
   (ii) Through wall imaging and surveillance systems
2. Vehicular radar systems
   (i) Provides for the operation of vehicular radar, collision avoidance, suspension systems etc.
3. Communication and Measurement Systems
   (i) Indoor Systems
   (ii) Outdoor Hand-held Systems

For UWB systems, a very wide bandwidth of 7.5 GHz between 3.1 GHz and 10.6 GHz is available and the power emission level up to -41.3 dBm/MHz. Fig. 2.8 shows UWB

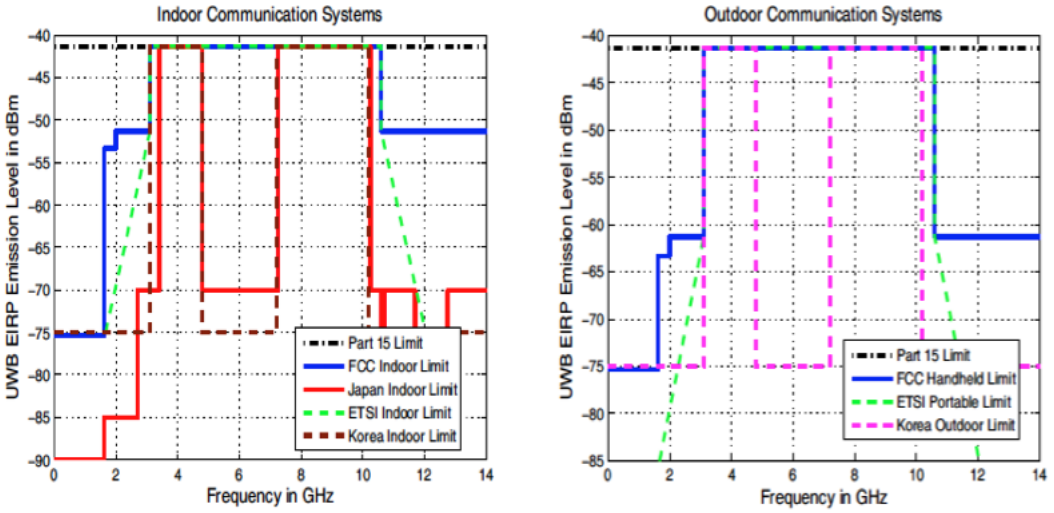


FIGURE 2.8: UWB regulations for various parts of the world [50–52].

emission limits for indoor and outdoor communications systems for various parts of the world. The emission limits for various types of UWB systems are listed in Table 2.2.

In UWB communications, the antennas proposed for BCWC applications must take into considerations the main characteristics of UWB technology such as the operational bandwidth 3.1-10.6 GHz, the emission power level and short-pulse signal with minimum distortion over the frequency range. In addition to these requirements, UWB antennas must also consider other constraints such as group delay and fidelity. To achieve greater accuracy, antennas for body-centric communications must be designed in the presence of the human body, as body tissues absorb a great portion of the power supplied to the antenna and affect the antenna input impedance, radiation patterns and resonant frequency.

TABLE 2.2: Emission limits for the various types of UWB systems

| Frequency range (MHz) | 960-1610 | 1610-1990 | 1990-3100 | 3100-10600 | Above 10600 | 1164-1240<br>1559-1610 |
|---|---|---|---|---|---|---|
| Ground penetrating radar ,wall imaging,through wall imaging systems | -65.3 | -53.3 | -51.3 | -41.3 | -51.3 | -75.3 |
| UWB bandwidth below 960 MHz | -65.1 | -53.3 | -51.3 | -51.3 | -51.3 | -75.3 |
| UWB bandwidth 1990-10600 MHz | -46.3 | -41.3 | -41.3 | -41.3 | -51.3 | -56.3 |
| Surveillance Systems | -53.3 | -51.3 | -41.3 | -41.3 | -51.3 | -63.3 |
| Medical Imaging Systems | -65.3 | -53.3 | -51.3 | -41.3 | -51.3 | -75.3- 53.3 |
| Indoor UWB Systems | -75.3 | -53.3 | -51.3 | -41.3 | -51.3 | -85.3 |
| Hand held UWB Systems | -75.3 | -63.3 | -61.3 | -41.3 | -61.3 | -85.3 |
| Vehicular radar systems | -75.3 | -61.3 | -41.3 | -51.3 | -61.3 | -85.3 |

Many UWB antennas for body-centric communications have been reported in the literature (see Fig. 2.9) [53–58]. In [59], Haga *et al.* presented a cavity slot antenna for on-body application with results showing that the proposed antenna has a relatively high efficiency of more than 50% even in the vicinity of the human body. Characterisation of

UWB antenna for body-worn application was conducted by Klemm *et al.* [60] through numerical modelling. The study used aperture-stacked antenna which shows high fidelity values in different directions suggesting that the antenna could be a good candidate for UWB wireless body area networks.

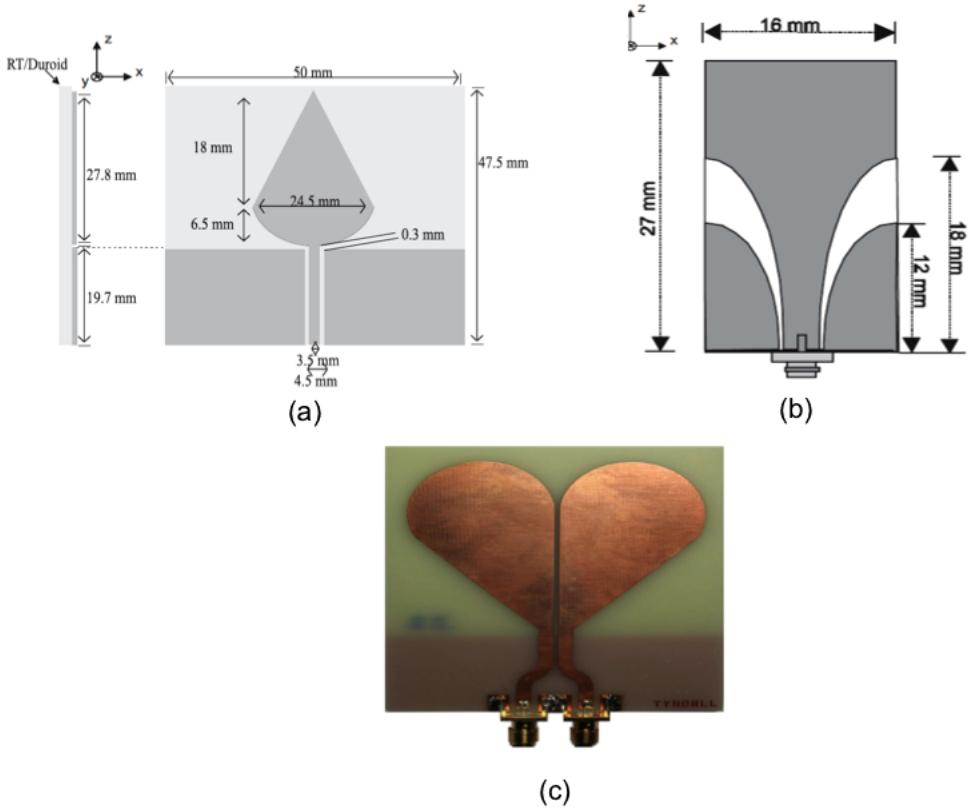


FIGURE 2.9: UWB antennas for body-centric wireless communication (a) CPW-fed planar inverted cone antenna (PICA) [57], (b) CPW-fed tapered slot antenna (TSA) [58] and (c) Folded planar differential antenna [56].

Other studies have shown that using printed monopoles, the antennas can have wideband characteristics and electrical lengths which are much shorter than $\frac{\lambda}{4}$ at the lowest operating frequency [61, 62]. Various regular shaped printed monopole antennas have been reported in the open literature suitable for UWB applications [63–67]. Unlike planar disc monopoles which are mounted perpendicularly on ground plane, the printed monopoles offer easy integration on printed circuit board, reduce size on dielectric substrate and fabrication.

As printed monopoles provide relatively ultra-wide frequency band and radiation patterns similar to dipole antennas, as well as simple structure and low fabrication cost, in this study, we have proposed a printed rectangular monopole antenna with Q-slot in chapter **3** and printed spline curve monopoles in chapter **4** for our on-body and microwave imaging applications.

### 2.4.1 Review of Antennas for Microwave Imaging

In the last decade, there has been renewed interest in microwave imaging for medical applications more especially breast cancer detection [68–71]. The current approach in detecting breast cancer is mammography i.e using X-ray to map the densities of the breast to detect tumours [72]. However, concerns have been raised about the ionising nature of x-ray diagnostic techniques and the rate of false negatives. Microwave imaging on the other hand offers a complementary or an alternative solution to detect breast cancer.

The general approach for microwave imaging system is that the object under test, for example, the breast is illuminated with UWB pulses from a number of antennas. The scattered signals are received by the surrounding antennas. The retrieved waveforms contain relevant information about the scattering object, such as the distance and size. By collecting and post-processing the backscatters with imaging algorithm, a high-resolution dielectric map of the breast can be generated.

In recent years, many different types of antennas such as monopole antennas, bow-tie antennas, patch antennas, vivaldi antennas and pyramidal horn antennas have been proposed for imaging applications [73–77]. In [78], Bassi *et al.* proposed a pair of two identical printed monopoles for an integrated radar-based microwave imaging for breast cancer detection. The antennas were integrated with a custom hardware using integrated circuit implemented in a 65-nm CMOS technology. The results show that custom hardware design can replace commercial microwave laboratory equipment with advantages in terms of performance, size, and cost of the imaging setup.

In [79], Benjamin *et al.* from University of Bristol developed a multi-static system using 60 patch antenna elements arranged in a hemispherical fashion as shown in Fig. 3.28. The stacked patch antennas were located on top of the system with 60 switches below the system to select the antenna to be the transmitter or receiver at a time. The results show viability of detecting tumour as small as 4 mm- 6 mm using 3D breast phantom. In a related development, Hagness *et al.* [80] from University of Wisconsin also presented presented a mono-static UWB system with an UWB pyramidal horn antenna for breast tumour detection. The system used a single horn antenna to scan through an array of antennas around a breast phantom, with each position of the array transmitting signal and receiving the backscatter. The results were processed using confocal imaging algorithm.

This subsection has reviewed different types of antennas for microwave imaging being monopole antennas, patch antennas, horn antennas and vivaldi antennas. Some of the antennas have complex structures with sizes relatively large. In many UWB applications,

antennas with compact size are desired. Therefore, in this study, we propose novel monopole antennas, compact in size with spline curve radiators for our UWB microwave imaging applications. The size of the proposed antennas are comparable to those reported in the open literature [56–58].

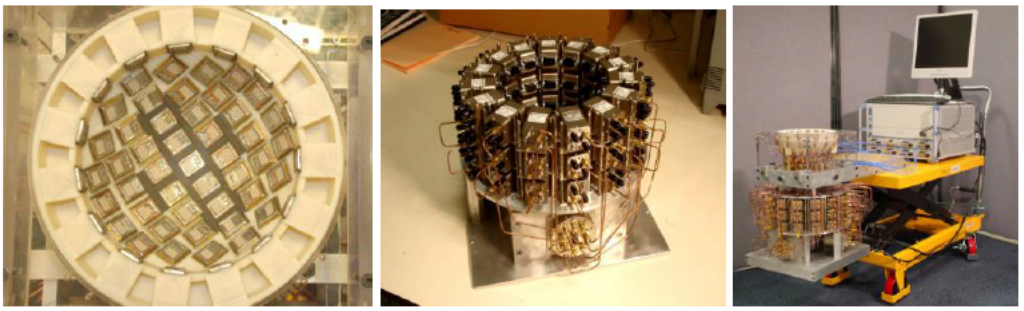

(a) (b) (c)

FIGURE 2.10: Multi-static imaging system (a) Sixty element antenna array, (b) Tx/Rx electromechanical switching interface and (c) The whole imaging system [79].

## 2.5 Fundamentals of Antenna Theory

An antenna is a key component for radio-linked communications. According to IEEE standard definition an antenna is "that part of a transmitting or receiving system that is designed to radiate or receive electromagnetic waves" [81]. Thus, an antenna is part of the wireless communication system acting as a transitional structure between free-space and a guiding device.

Many individuals, institutions and organisations are involved in the design, manufacture, measurement and use of antennas for many applications. In all cases, the quality and performance of an antenna is assessed and evaluated using some parameters such as return loss, gain, impedance, polarisation, bandwidth, directivity and efficiency. The following subsections will define some of the most commonly used parameters.

### 2.5.1 Return Loss

Antenna return loss measures the difference between the input power and the power reflected from a discontinuity in a transmission circuit. Usually the return loss is expressed as the ratio in decibels of the power incident on the antenna terminal to the power reflected from the terminal;

$$R_L(dB) = 10\log_{10}\left(\frac{P_{in}}{P_{ref}}\right) \tag{2.5}$$

where $R_L(dB)$ is the return loss, $P_{in}$ is the the incident power, $P_{ref}$ is the reflected power.

### 2.5.2 Impedance

An antenna's impedance is the ratio of the voltage to the current at the input terminals of the antenna. Mathematically, impedance is expressed as;

$$Z_{in} = \frac{V}{I} \tag{2.6}$$

where $Z_{in}$ is the impedance, $V$ is the voltage and $I$ is the current. The input impedance is a function of frequency and depends on other factors such as the antenna's geometry, its methods of excitation and its proximity to surrounding environments.

### 2.5.3 Radiation Pattern

One of the important parameters of any antenna is its radiation pattern, defined as "a mathematical function or a graphical representation of the radiation properties of the antenna as a function of space coordinates. In most cases, the radiation pattern is determined in the farfield region and is represented as a function of the directional coordinates. Radiation properties include power flux density, radiation intensity, field strength, directivity, phase or polarisation" [31]. For a linearly polarised antenna, its performance is often described in terms of its principle E-plane and H-plane patterns. Basically, there are three commonly patterns that are used to describe antennas. Isotropic antennas have equal radiation in all directions, but this is a hypothetical scenario that will be difficult to achieve in practice. Antennas with directional radiation patterns radiate or receive electromagnetic waves more effectively in some directions than others. Finally, antennas with omni-directional radiation patterns essentially have a non-directional pattern in a given plane and a directional pattern in any orthogonal plane.

### 2.5.4 Directivity and Efficiency

Directivity $D$ is defined as the ratio of the radiation intensity $U$ in a given direction from the antenna to the radiation intensity over that of an isotropic source [6, 31]. In case of

isotropic source, the radiation intensity $U_o$ is equal to the total radiated power $P_{rad}$ by the antenna divided by $4\pi$;

$$D = \frac{U}{U_o} = \frac{4\pi U}{P_{rad}} \tag{2.7}$$

Radiation efficiency ($e_{rad}$) on the other hand is the ratio of the total radiated power to the net power accepted by the antenna;

$$e_{rad} = \frac{P_{rad}}{P_{in}} \tag{2.8}$$

### 2.5.5 Gain

Another useful measure describing the performance of an antenna is the gain $G$. It is directly linked with the directivity of antenna, but it takes into account the efficiency of the antenna as well as the directional properties. It is simply defined as "the ratio of the intensity, in a given direction, to the radiation intensity that would be obtained if the power accepted by the antenna were radiated isotropically" [31]. Another useful definition of gain is that it is the product of the directivity and the radiation efficiency, written as;

$$G(\theta, \phi) = \frac{4\pi U(\theta, \phi)}{P_{in}} \tag{2.9}$$

$$G = e_{rad} D \tag{2.10}$$

Thus, the gain of an antenna is equal to its purely directional characteristic of directivity multiplied by radiation efficiency.

## 2.6 Summary

This chapter reviews start-of-the-art of body-centric wireless communication. It provides a review of relevant works already reported in the literature which are of relevance to this work. We looked at three different spectra i.e. Medical Implantable Communication Service (MICS) Band 402-405 MHz, Industrial, Scientific and Medical Band (ISM) 2.45 GHz and Ultra-Wideband (UWB) 3.1-10.6 GHz.

For MICS band, we have proposed two types of PIFAs i.e a spiral PIFA and meandered circular PIFA for implantable applications. With the identical configuration, we used mirror image approach to achieve similar results at the operating frequency and combined with miniaturisation techniques such as using high permittivity substrate, shorting pin and stacking of the radiators, the proposed antennas are compact in size and volume.

In the ISM band at 2.45 GHz, we have proposed a very simple structure with an easy mechanism to control its resonant frequency. The proposed structure also show resilient in the close proximity to human body. For UWB spectrum, we have proposed three monopoles for on-body and microwave imaging applications. The advantages of the antennas have been explained in the respective chapters **3** and **4**.

# References


[1] P. S. Hall and Y. Hao, *Antenna and Propagation for Body-Centric Wireless Communications*. Norwood, MA, USA , Artech House, 2006.

[2] P. S. Hall and Y. Hao, "Antennas and propagation for body centric communications," in *First European Conference on Antennas and Propagation, Nice,France*, pp. 1–7, November, 2006.

[3] "International Telecommunications Union-Recommendations(ITU-R),Radio Regulations,sa.1346, itu, geneva, switzerland, http://itu.int/home,"

[4] "Medical implant communications service (mics) federal register,rules and regulations," vol. vol. 64 no. 240 ed, Dec. 1999.

[5] "European telecommunication standards for Mics." Website, Retrieved on 14th September, 2015. http://portal.etsi.org/tb/status/status.asp.

[6] W. L. Stutzman and G. A. Thiele, *Antenna Theory and Design*. John Wiley and Sons, Inc., third ed., 2013.

[7] W. A. Qureshi, "Current and future applications of the capsule camera," *Nature Reviews Drug Discovery*, vol. 3, pp. 447–450, May 2004.

[8] "Glucowise." Website, Accessed on 4th January, 2017. http://www.gluco-wise.com.

[9] M. Amundson, J. V. Arx, W. Linder, P. Rawat, and W. Mass, "Circumferential antenna for an implantable medical device," Sept. 24 2002. US Patent 6,456,256.

[10] Z. Tang, B. Smith, J. Schild, and P. Peckham, "Data transmission from an implantable biotelemetry by load-shift keying using circuit configuration modulator," *Biomedical Engineering, IEEE Transactions*, vol. 42, pp. 524–528, May 1995.

[11] W. Scanlon, N. Evans, and Z. McCreesh, "RF performance of a 418 M Hz radio telemetry packaged for human vaginal placement," *Biomedical Engineering, IEEE Transactions on*, vol. 44, pp. 427–430, May 1997.

[12] P. Valdastri, A. Menciassi, A. Arena, C. Caccamo, and P. Dario, "An implantable telemetry platform system for in vivo monitoring of physiological parameters," *Information Technology in Biomedicine, IEEE Transactions*, vol. 8, pp. 271–278, Sept 2004.

[13] A. Kiourti and K. Nikita, "A review of implantable patch antennas for biomedical telemetry: Challenges and solutions"," *Antennas and Propagation Magazine, IEEE*, vol. 54, pp. 210–228, June 2012.

[14] S. Soora, K. Gosalia, M. Humayun, and G. Lazzi, "A Comparison of Two and Three Dimensional Dipole Antennas for an Implantable Retinal Prosthesis," *Antennas and Propagation, IEEE Transactions*, vol. 56, pp. 622–629, March 2008.

[15] E. Chow, M. Morris, and P. Irazoqui, "Implantable RF Medical Devices: The Benefits of High-Speed Communication and Much Greater Communication Distances in Biomedical Applications," *Microwave Magazine, IEEE*, vol. 14, pp. 64–73, June 2013.

[16] F. Merli, B. Fuchs, J. Mosig, and A. Skrivervik, "The effect of insulating layers on the performance of implanted antennas," *Antennas and Propagation, IEEE Transactions*, vol. 59, pp. 21–31, Jan 2011.

[17] Z. N. Chen, G. C. Liu, and T. See, "Transmission of rf signals between mics loop antennas in free space and implanted in the human head," *Antennas and Propagation, IEEE Transactions*, vol. 57, pp. 1850–1854, June 2009.

[18] K. Gosalia, M. Humayun, and G. Lazzi, "Impedance matching and implementation of planar space-filling dipoles as intraocular implanted antennas in a retinal prosthesis," *Antennas and Propagation, IEEE Transactions*, vol. 53, pp. 2365–2373, Aug 2005.

[19] A. Kiourti and K. Nikita, "Miniature scalp-implantable antennas for telemetry in the mics and ism bands: Design, safety considerations and link budget analysis," *Antennas and Propagation, IEEE Transactions*, vol. 60, pp. 3568–3575, Aug 2012.

[20] F. Merli, L. Bolomey, J. Zurcher, G. Corradini, E. Meurville, and A. Skrivervik, "Design, realization and measurements of a miniature antenna for implantable wireless communication systems," *Antennas and Propagation, IEEE Transactions*, vol. 59, pp. 3544–3555, Oct 2011.

[21] A. Kiourti, J. Costa, C. Fernandes, A. Santiago, and K. Nikita, "Miniature implantable antennas for biomedical telemetry: From simulation to realization," *Biomedical Engineering, IEEE Transactions*, vol. 59, pp. 3140–3147, Nov 2012.

[22] L. Changrong, Y. X. Guo, and X. Shaoqiu, "Compact dual-band antenna for implantable devices," *Antennas and Wireless Propagation Letters, IEEE*, vol. 11, pp. 1508–1511, 2012.

[23] L. J. Xu, Y. X. Guo, and W. Wu, "Dual-band implantable antenna with open-end slots on ground," *Antennas and Wireless Propagation Letters, IEEE*, vol. 11, pp. 1564–1567, 2012.

[24] L. Changrong, Y. X. Guo, S. Hucheng, and X. Shaoqiu, "Design and safety considerations of an implantable rectenna for far-field wireless power transfer," *Antennas and Propagation, IEEE Transactions*, vol. 62, pp. 5798–5806, Nov 2014.

[25] J. Kim and Y. Rahmat-Samii, "Implanted antennas inside a human body: Simulations, designs, and characterizations," *IEEE Trans. Microw. Theory Tech*, vol. 52, pp. 1934–1943, Nov 2004.

[26] J. Kim and Y. Rahmat-Samii, "Planar inverted-f antennas on implantable medical devices:meandered type versus spiral type," *Microwave and Optical Technology Letters*, vol. 48, no. 3, pp. 567–572, 2006.

[27] C. M. Lee, T. C. Yo, C. H. Luo, C. Tu, and Y. Juang, "Compact broadband stacked implantable antenna for biotelemetry with medical devices," *Electronics Letters*, vol. 43, pp. 660–662, June 2007.

[28] W. Liu, S. H. Chen, and C. M. Wu, "Bandwidth enhancement and size reduction of an implantable pifa antenna for biotelemetry devices," *Microwave and Optical Technology Letters*, vol. 51, no. 3, pp. 755–757, 2009.

[29] T. Karacolak, A. Z. Hood, and E. Topsakal, "Design of a dual-band implantable antenna and development of skin mimicking gels for continuous glucose monitoring," *IEEE Transactions on Microwave Theory and Technique*, vol. 56, p. 1001?1008, April 2008.

[30] A. Kiourti, M. Christopoulou, and K. Nikita, "Performance of a novel miniature antenna implanted in the human head for wireless biotelemetry," in *Antennas and Propagation (APSURSI), 2011 IEEE International Symposium on*, pp. 392–395, July 2011.

[31] C. A. Balanis, *Antenna Theory : Analysis and Design*. New York: John Wiley & Sons, third ed., 2005.

[32] J. Volakis, *Antenna Engineering Handbook*. McGraw-Hill, fourth ed., 2007.

[33] P. Soontornpipit, C. M. Furse, and C. Y. Chung, "Design of implantable microstrip antenna for communication with medical implants," *Microwave Theory and Techniques, IEEE Transaction*, vol. 52, pp. 1944–1951, 2004.

[34] "Ism bands." Website, Retrieved on 19th October, 2015. https://en.wikipedia.org/wiki/ISM_band.

[35] "About z-wave technology." Website, Retrieved on 19th October, 2015. http://z-wavealliance.org/z-wave-alliance-overview.

[36] "Understanding z-wave networks, nodes and devices." Website, Retrieved on 19th October, 2015. http://www.vesternet.com/resources/technology-indepth/understanding-z-wave-networks.

[37] "What is z-wave." Website, Retrieved on 19th October, 2015. http://www.z-wave.com/what_is_z-wave.

[38] K. Wong and C. I. Lin, "Characteristics of a 2.45 ghz compact shorted patch antenna in close proximity to a lossy medium," *Microw. Opt. Technol. Lett.,*, vol. 45, no. 6, pp. 480–483, 2005.

[39] P. Salonen, Y. Rahmat-Samii, and M. Kivikoski, "Wearable antennas in the vicinity of human body," *IEEE Antenna and Propagation Society Symposium*, vol. 1, pp. 467–470, June 2005.

[40] A. Alomainy, Y. Hao, A. Owadally, C. G. Parini, P. S. Hall, and C. C. Constantinou, "Statistical analysis and performance evaluation for on-body radio propagation with microstrip patch antennas," *IEEE Antenna and Propagation Society Symposium*, vol. 55, pp. 245–248, January 2007.

[41] S. Agneessens, P. V. Torre, E. Tanghe, G. Vermeeren, W. Joseph, and H. Rogier, "On-body wearable repeater as a data link relay for in-body wireless implants," *IEEE Antennas Wirel. Propag. Lett.*, vol. 11, pp. 1714–1717, January 2012.

[42] Y. Cho and H. Yoo, "Miniaturised dual-band implantable antenna for wireless biotelemetry," *Electronic Lett.*, vol. 52, pp. 1005–1007, June 2016.

[43] N. Haga, K. Saito, M. Takahashi, and K. Ito, "Characteristics of cavity slot antenna for body-area networks," *Antennas and Propagation, IEEE Transactions*, vol. 57, pp. 837–843, April 2009.

[44] M. R. Kamruddin, Y. Nechayev, and P. Hall, "Performances of antennas in the on-body environment," *IEEE Antennas and Propagation Society International Symposium*, vol. 3A, pp. 475–478, June 2005.

[45] Z. Wang, L. Zhang, and J. L. Volakis, "Textile antennas for wearable radio frequency applications," *Textiles and Light Industrial Science and Technology*, vol. 2, pp. 105–112, July 2013.

[46] C. Hertleer, H. Rogier, L. Vallozzi, and L. van Langenhove, "A textile antenna for off-body communication integrated into protective clothing for fire-fighters," *IEEE Transactions on Antennas and Propagation*, vol. 57, pp. 919–925, 07 April 2009.

[47] Y. Bayram, a. B. S. S. Y. Zhou, S. Xu, J. Zhu, N. A. Kotov, and J. L. Volakis, "E-textile conductors and polymer composites for conformal lightweight antennas," *IEEE Transactions on Antennas and Propagation*, vol. 58, pp. 2732–2736, August 2010.

[48] K. Koski, A. Vena, L. Sydänheimo, L. Ukkonen, and Y. Rahmat-Samii, "Design and implementation of electro-textile ground planes for wearable uhf rfid patch tag antennas," *IEEE Antennas and Wireless Propagation Letters*, vol. 12, pp. 964–967, December 2013.

[49] S. Zhu and R. Langley, "Design and implementation of electro-textile ground planes for wearable uhf rfid patch tag antennas," *IEEE Transactions on Antennas and Propagation*, vol. 57, pp. 926–935, April 2009.

[50] "First report and order." Website, Retrieved on 14th October, 2015. https://transition.fcc.gov/Bureaus/Engineering_Technology/Orders/2002/fcc02048.pdf.

[51] "System maintenance for uwb (ultra wide band) microwave band radio system." Website, Retrieved on 1st January 2017. http://www.soumu.go.jp/main_sosiki/joho_tsusin/eng/Releases/Telecommunications/100908_g.html.

[52] "Ultra wide band." Website, Retrieved on 1st January 2017. http://www.etsi.org/technologies-clusters/technologies/radio/ultra-wide-bandhighlight=YTozOntpOjA7czozOiJ1d2IiO2k6MTtzOjEwOiJ0ZWNobm9sb2d5IjtpOjI7czoxNDoidXdiIHRlY2hub2x

[53] A. Alomainy, Y. Hao, X. Hu, C. Parini, and P. Hall, "Uwb on-body radio propagation and system modelling for wireless body-centric networks," *Communications, IEE Proceedings*, vol. 153, pp. 107–114, Feb 2006.

[54] T. S. P. See and Z. N. Chen, "Experimental characterization of uwb antennas for on-body communications," *Antennas and Propagation, IEEE Transactions*, vol. 57, pp. 866–874, April 2009.

[55] M. Khan, Q. Abbasi, A. Alomainy, Y. Hao, and C. Parini, "Experimental characterisation of ultra-wideband off-body radio channels considering antenna effects," *Microwaves, Antennas Propagation, IET*, vol. 7, pp. 370–380, April 2013.

[56] L. Vallozzi, D. Pepe, T. Castel, H. Rogier, and D. Zito, "On-body characterization of planar differential antennas for multiple, wide, and narrow bands," *International Journal of Antennas and Propagation*, vol. 2016, 2016.

[57] A. Alomainy, A. Sani, J. Santas, A. Rahman, and Y. Hao, "Transient characteristics of wearable antennas and radio propagation channels for ultra wideband body-centric wireless communications," *IEEE Transactions on Antennas and Propagation*, vol. 57, pp. 875–884, April 2009.

[58] A. Rahman, A. Alomainy, and Y. Hao, "Compact body-worn coplanar waveguide fed antenna for uwb body-centric wireless communication," *Antennas and Propagation, EuCAP 2007. The Second European Conference*, pp. 1–4, November 2007.

[59] N. Haga, K. Saito, M. Takahashi, and K. Ito, "Characteristics of cavity slot antenna for body-area networks," *Antennas and Propagation, IEEE Transactions*, vol. 57, pp. 837–843, April 2009.

[60] M. Klemm, I. Kovacs, G. Pedersen, and G. Toster, "Novel small-size directional antenna for uwb wban/ wpan applications," *IEEE Transaction Antennas and Propagation*, vol. 55, pp. 3884–3896, December 2005.

[61] N. P. Agrawall, G. Kumar, and K. P. Ray, "Wide-band planar monopole antennas," *IEEE Transactions on Antennas and Propagation*, vol. 46, pp. 294–295, February 1998.

[62] M. Ammann and Z. Chen, "Wideband monopole antennas for multi-band wireless systems," *IEEE Antennas and Propagation Magazine*, vol. 45, pp. 146–150, April 2003.

[63] J. Liang, C. C. Chiau, X. Chen, and C. G. Parini, "Study of a printed circular disc monopole antenna for uwb systems," *IEEE Transaction Antennas and Propagation*, vol. 53, pp. 3500–3504, November 2005.

[64] C.-Y. Huang and W.-C. Hsia, "Planar elliptical antenna for ultra-wideband communications," *Electronics Letters,*, vol. 41, no. 6, pp. 296–297, 2005.

[65] K. P. Ray, Y. Ranga, and P. Gabhale, "Printed square monopole antenna with semi-circular base for ultra-wide bandwidth," *Electronics Letters*, vol. 43, no. 5, pp. 263–265, 2007.

[66] J.-P. Zhang, Y.-S. Xu, and W.-D. Wang, "Ultra-wideband microstrip-fed planar elliptical dipole antenna," *Electronics Letters*, vol. 42, no. 3, pp. 144–145, 2006.

[67] K. P. Ray, G. Kumar, and P. V. Anob, "Wideband circular wire mesh and annular ring monopole antennas," *Microwave and Optical Technology Letters*, vol. 48, no. 12, pp. 2459–2461, 2006.

[68] E. Fear, X. Li, S. Hagness, and M. Stuchly, "Confocal microwave imaging for breast cancer detection: Localization of tumors in three dimensions," *IEEE Trans. Biomed. Eng.*, vol. 49, pp. 812–822, August 2002.

[69] E. Fear, P. Meaney, and M. Stuchly, "Microwaves for breast cancer detection?," *IEEE Potentials*, vol. 22, no. 1, pp. 12–18, 2003.

[70] D. Kurrant, E. Fear, and D. Westwick, "Tumor response estimation in radar-based microwave breast cancer detection," *IEEE Trans. Biomed.Eng*, vol. 55, pp. 2801–2811, December 2008.

[71] Y. Chen and P. Kosmas, "Detection and localization of tissue malignancy using contrast-enhanced microwave imaging: Exploring information theoretic criteria," *IEEE Trans. Biomed.Eng*, vol. 59, pp. 766–776, March 2012.

[72] I. C. H. Sharyl, J. Nass, and J. C. Lashof, *Mammography and Beyond: Developing Technologies for the Early Detection of Breast Cancer.* Nat. Academies Press, Washington, DC, U.S.A, 2001.

[73] S. Latif, D. Flores-Tapia, S. Pistorius, and L. Shafai, "A planar ultrawideband elliptical monopole antenna with reflector for breast microwave imaging," *Microwave and Optical Technology Letters*, vol. 56, no. 4, pp. 808–813, 2014.

[74] D. Gibbins, M. Klemm, I. Craddock, J. Leendertz, A. Preece, and R. Benjamin, "A comparison of a wide-slot and a stacked patch antenna for the purpose of breast cancer detection," *IEEE Transaction Antennas and Propagation*, vol. 58, no. 3, pp. 665–674, 2010.

[75] G. Bindu, V. Hamsakkutty, A. Lonappan, J. Jacob, V. Thomas, C. K. Aanandan, and K. T. Mathew, "Wideband bow-tie antenna with coplanar stripline feed," *Microwave and Optical Technology Letters*, vol. 42, pp. 222–224, August 2004.

[76] X. Li, S. C. Hagness, M. K. Choi, and D. W. van der Weide, "Numerical and experimental investigation of an ultrawideband ridged pyramidal horn antenna with curved launching plane for pulse radiation," *IEEE Antennas and Wireless Propagation Letters*, vol. 2, pp. 259–262, 2003.

[77] J. Bourqui, M. Okoniewski, and E. C. Fear, "Balanced antipodal vivaldi antenna with dielectric director for near-field microwave imaging," *IEEE Antennas and Wireless Propagation Letters*, vol. 58, pp. 2318–2326, July 2010.

[78] M. Bassi, M. Caruso, M. S. Khan, A. Bevilacqua, A.-D. Capobianco, and A. Neviani, "An integrated microwave imaging radar with planar antennas for breast cancer detection," *IEEE Transaction on Microwave Theory and Techniques*, vol. 61, pp. 2108–2118, May 2013.

[79] T. Henriksson, M. Klemm, D. Gibbins, J. Leenderts, T. Horseman, A. Preece, R. Benjamin, and I. Craddock, "Clinical trials of a multistatic uwb radar for breast imaging," *Antennas and Propagation Conference (LAPC), 2011 Loughborough*, pp. 1–4, 2011.

[80] X. Li, S. Davis, S. Hagness, D. V. D. Weide, and B. V. Veen, "Mircrowave imaging via space-time beamforming: experimental investigation of tumor detection in multilayer breast phantoms," *IEEE Transactions on Microwave Theory and Techniques*, vol. 52, no. 8, pp. 1856–1865, 2004.

[81] "Ieee standard for definitions of terms for antennas," *IEEE Std 145-2013 (Revision of IEEE Std 145-1993)*, pp. 1–50, 2014.

# Chapter 3

# Q-Slot UWB Monopole Antenna

## 3.1 Printed Monopole Antennas

As has been discussed in the previous chapter, several types of planar monopoles which exhibit ultra-wide impedance bandwidth have been proposed for on-body and microwave imaging applications. Monopole antennas are attractive for body-centric wireless communication because they are easy to construct and implement from simulation to practical experiment. Monopole antennas with different basic shapes such as rectangle, square, circle, ellipse, triangular, rectangular with semicircular bottom and hexagon on ground plane for practical UWB applications have been proposed[1] (see Fig. 3.1). Printed monopole antenna can also be viewed as a special case of microstrip antenna configuration with ground plane assume to be at infinity [2]. Usually the radiator is etched on a substrate, for example, FR4. It can also be assumed that beyond the substrate, there exist a very thick air with ($\varepsilon_r = 1$), that make a microstrip antenna configuration with thick substrate $\varepsilon_r$ closer to unity resulting in high bandwidth.

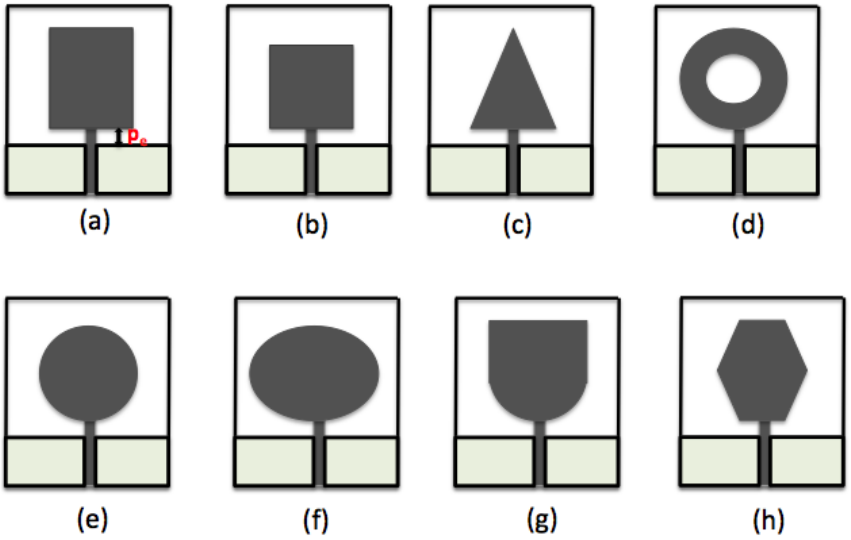


FIGURE 3.1: Examples of different basic shapes of printed monopoles: (a) rectangular, (b) square, (c) triangular, (d) annular ring, (e) circular, (f) elliptical, (g) rectangular with semicircular bottom, and (h) hexagonal.

In [3, 4], extensive study of CPW-fed circular disc, microstripline-fed circular disc and elliptical disc monopoles for UWB application have been demonstrated. The results from the study show that the overlapping of the closely distributed resonance contribute to UWB characteristics of the antenna. In a related study, printed-slot monopoles have been shown as capable of providing ultra-wideband bandwidth [5]. Furthermore, the demands on antenna for such applications should include acceptable input matching and stable radiation over a wide band of operation. In addition to these demands, there is also emphasis on the time-domain characteristics of the antenna, particularly its ability to maintain a radiated pulse.

In this chapter we present the design and analysis of a printed rectangular monopole (PRM) UWB antenna with a Q-slot for on-body and microwave imaging applications. We also discuss the experimental characterisation of the antenna in close proximity to human body and breast phantom. We also look at other performance indicators of the antenna including its radiation patterns and time-domain characteristics with emphasis on fidelity and impulse response.

The proposed antenna was designed to provide optimise wide-band performance and pulse fidelity in the UWB range of 3.1 GHz to 10.6 GHz. The antenna also exhibits high immunity and stable radiation pattern in close proximity to the human body. Following this section will cover the antenna geometry and design process.

## 3.2 Antenna Geometry

The geometry of the proposed PRMA with Q-slot consists of an $L_s \times W_s$ = 36.6 x 39mm$^2$ FR4 substrate with ($\varepsilon_r$ = 3, tan $\delta$ = 0.01 and thickness of 1.6 mm). On top of the substrate is an $L \times W$ = 18.3 x 23.8 mm$^2$ rectangular radiator. A thin Q-slot is etched on the radiator to generate additional resonance in the structure. At the back of the substrate is a partial rectangular ground plane measuring 36.6 x $gr$ mm$^2$ (see Fig. 3.2). A 50 Ω coaxial transmission line is used to feed the antenna.

### 3.2.1 Design Steps and Guidelines

As discussed earlier, printed monopole antenna (PMA) can be thought of as special case of microstrip antenna with the ground plane considered to be located at infinity [2]. The design process starts from modifying printed rectangular monopole antenna (PRMA) with appropriate dimensions for UWB operations. We take into account the attractive features of PRMA such as wide impedance characteristics, acceptable radiation performance and ease of fabrication.

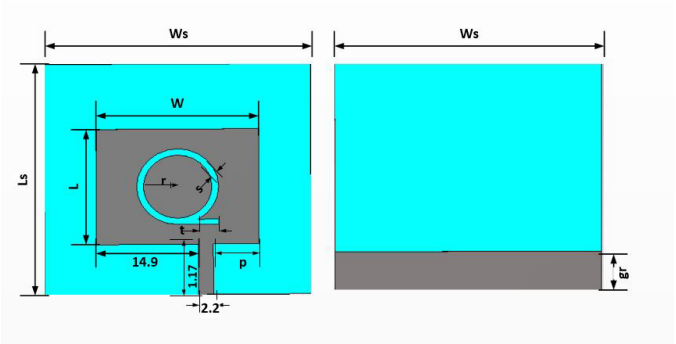


FIGURE 3.2: Geometry of PRMA with Q-slot: left (top view), right (bottom view). All dimensions in mm.

The lower band-edge frequency ($f_o$) at 3.1 GHz was estimated according to (3.1)[2, 6].

$$f_o = \frac{c}{\lambda} = \frac{7.2}{(L + r_e + p_e)} \tag{3.1}$$

where L (cm) is the length of the planar monopole antenna, which is equivalent to cylindrical monopole antenna of the same height L, W (cm) is the width of the planar monopole antenna, $r_e$ (cm) is effective radius of the equivalent cylindrical monopole antenna which is determined by equating area of the planar (LW) and cylindrical monopole antennas with the same radius ($2\pi r_e L$) as in (3.2 -3.3), $p_e$ is the length of feed gap shown in Fig. 3.1.

$$2\pi r_e L = LW \tag{3.2}$$

$$r_e = \frac{W}{2\pi} \tag{3.3}$$

It has been demonstrated that slot antennas can achieve broadband operation and miniaturisation as have been widely reported in the literature [7, 8]. For example, U-slots have been employed to achieve broadband operation in [9–11]. In this study, we have employed a Q-slot to achieve UWB operation and good impedance stability over the spectrum. We will carefully examine the effect of the Q-slot in the next section.

Following this analysis, we modelled the printed rectangular monopole antenna (PRMA) in CST Microwave Studio without Q-slot using the aforementioned dimensions. The next step involves plotting surface current distributions and contours at representative frequencies at 3.5 GHz, 6.5 GHz and 9 GHz close to resonance (See Fig. 3.3). We observed that the surface current density of the radiator was relatively weak at the central part of the structure for all the frequencies considered. Therefore, we carefully etched Q-slot at

the centre of the radiator to enhance impedance matching while generating additional resonance and UWB operation. We optimised the parameters using a Trust Region Framework (TRF) algorithm within CST Microwave Studio to achieve the final design. At this point we compared the $S_{11}$ of the PRMA with and without Q-slot as shown in Fig. 3.4.

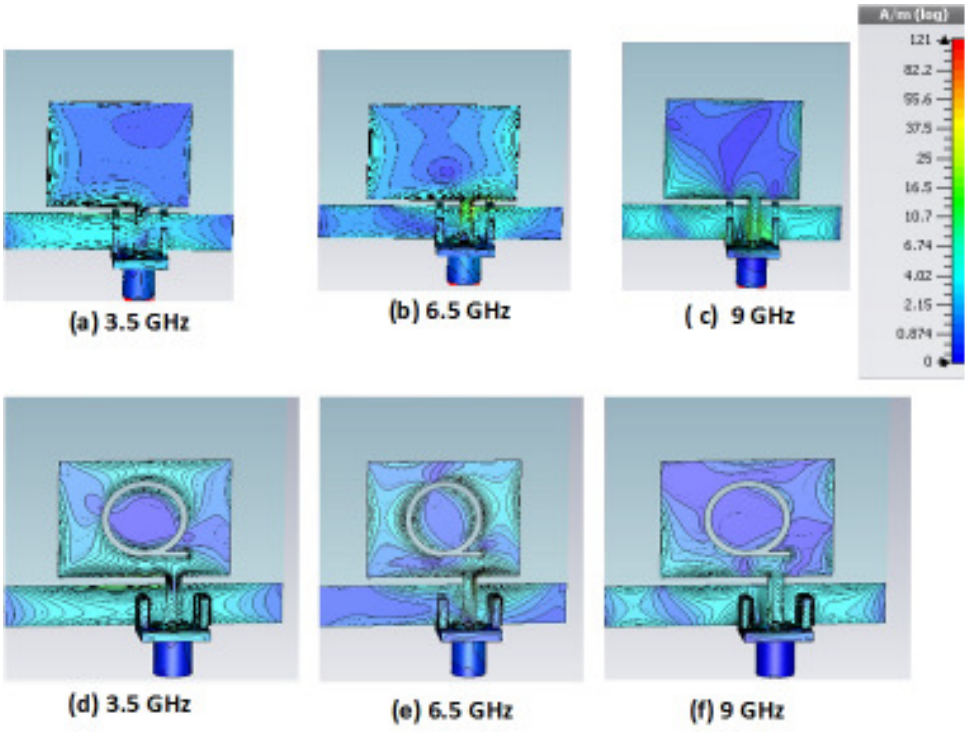


FIGURE 3.3: Surface current densities (a-c) without Q-slot (d-f) with Q-slot.

.

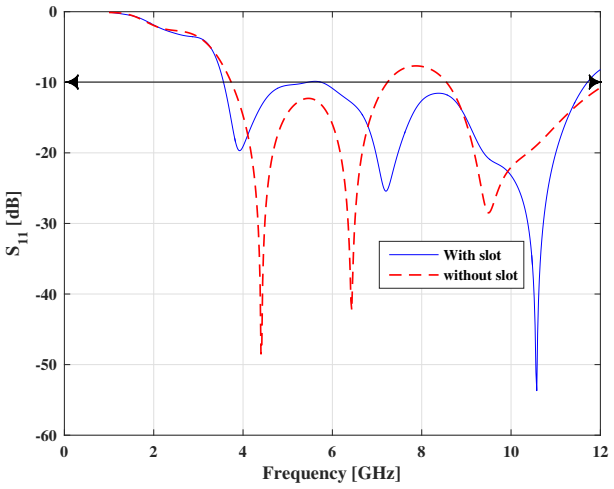


FIGURE 3.4: Simulated return loss for PRMA with and without Q-slot. The introduction of the Q-slot achieves a broader bandwidth and covers the whole UWB operation spectrum

TABLE 3.1: Summary and dimensions of the parameters of PRMA with Q-slot

| Parameter | Description | Optimised value |
|---|---|---|
| L | radiator length | 18.3 mm |
| W | radiator width | 23.8 mm |
| c | speed of light | $3 \times 10^8$ m/s |
| $f_o$ | fundamental frequency | 3.1 GHz |
| $r_e$ | effective radius of equivalent cylindrical monopole antenna | 3.0 mm |
| $p_e$ | feeding gap | 1.2 mm |
| h | substrate height | 1.6 mm |
| s | slot width | 1.0 mm |
| t | q-descender | 6.0 mm |
| p | feeding position | 6.7 mm |
| gr | ground length | 6.3 mm |
| r | outer radius of the Q-slot | 6.0 mm |

### 3.2.2 Parametric Study

For the parametric study, all parameters are fixed to those of Table 3.1 except for the variable. To gain further insight into the performance of the proposed PRMA, we examined the physical meaning and the effect of the introduction of Q-slot in terms of directivity, efficiency, return loss, impedance matching, and gain. We studied the effects of the following parameters with reference to Fig. 3.2: slot width $s$, feeding position $p$, outer radius of the slot $r$, Q-descender $t$ and ground plane length $gr$.

Firstly, our approach in this study is to compare the PRMA with and without Q-slot in terms of directivity, efficiency, return loss, impedance matching, and gain. The simulated 3D directivity of the two structures close to resonances are illustrated in Fig. 3.5. At all the sampled frequencies, there is slight increase in directivity of PRMA with Q-slot as compared to PRMA without slot. This could be attributed to an improved omni-directionality at high frequencies or improved directivity as a result of introduction of Q-slot, a true reflection shown on other indicator metrics tabulated in Table 3.2 for easy comparison.

The next step in our approach in this study is to examine the effect of Q-slot parameters (s,p,r,t,gr) on antenna gain and return loss. For parametric study, with the exception of the variable all other parameters are fixed to the optimal values in Table 3.1. Fig. 3.6 show the effect of changing these parameters on antenna gain. The results show that the gain varies approximately from 2 to 4 dBi at the lower end of the band, and from 6.0

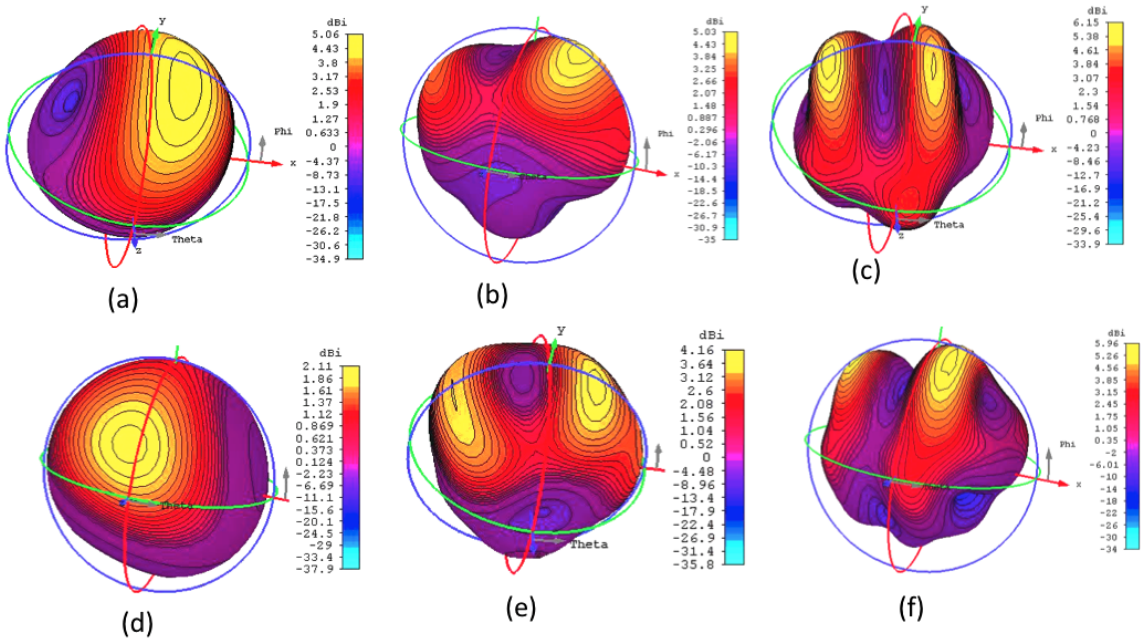


FIGURE 3.5: Simulated 3D directivity at 3.5 GHz, 6.5 GHz and 9.0 GHz: (a-c) PRMA with Q-slot and (d-f) PRMA without Q-slot.

TABLE 3.2: Comparison of characteristics of PRMA with and without Q-slot

| | PRMA | | | | | |
|---|---|---|---|---|---|---|
| Parameter | With Q-slot | | | Without Q-slot | | |
| Frequency[GHz] | 3.5 | 6.5 | 9.0 | 3.5 | 6.5 | 9.0 |
| Directivity[dBi] | 5.06 | 5.03 | 6.15 | 2.11 | 4.16 | 5.96 |
| Radiation eff.[%] | 98.40 | 99.60 | 98.68 | 95.60 | 96.87 | 97.30 |
| Total eff.[%] | 98.30 | 99.45 | 99.56 | 94.8 | 96.10 | 96.70 |
| Realised gain[dB] | 4.33 | 4.90 | 6.0 | -0.03 | 3.90 | 5.61 |

to 7.5 dBi at the upper end, a trend that supports the pattern observed in the antenna directivity. On the other hand, Fig. 3.6 (b) suggests that the gain varies considerably with changes in the ground plane length gr. For instance, for $gr = 40$ mm (corresponding to a full ground plane) the gain is maximised to 6.7 dBi for the lower frequencies, and 7.6 dBi for the higher portion of the spectrum. However, for a full ground plane, the proposed PRMA becomes a typical microstrip patch antenna (MSA) with most of the signals reflected in one direction, therefore, the proposed antenna no longer behaves as a printed monopole with poor return loss and input matching which does not meet -10 dB UWB bandwidth of 3.1 GHz - 10.6 GHz (see Fig. 3.7 (b)). For the feeding position $p$, we identified two optimal positions i.e 6.7 mm and 0 mm (edge of the radiator). We noticed that by optimising the feeding position, $p$, from the centre of the radiator, there

is excitation of additional modes resulting in wider bandwidth [2]. However, at -10 dB bandwidth $p = 6.7$ mm provides a wider band from 3.1 GHz - 11.7 GHz whiles $p = 0$ mm covers 4.3 GHz - 10.4 GHz.

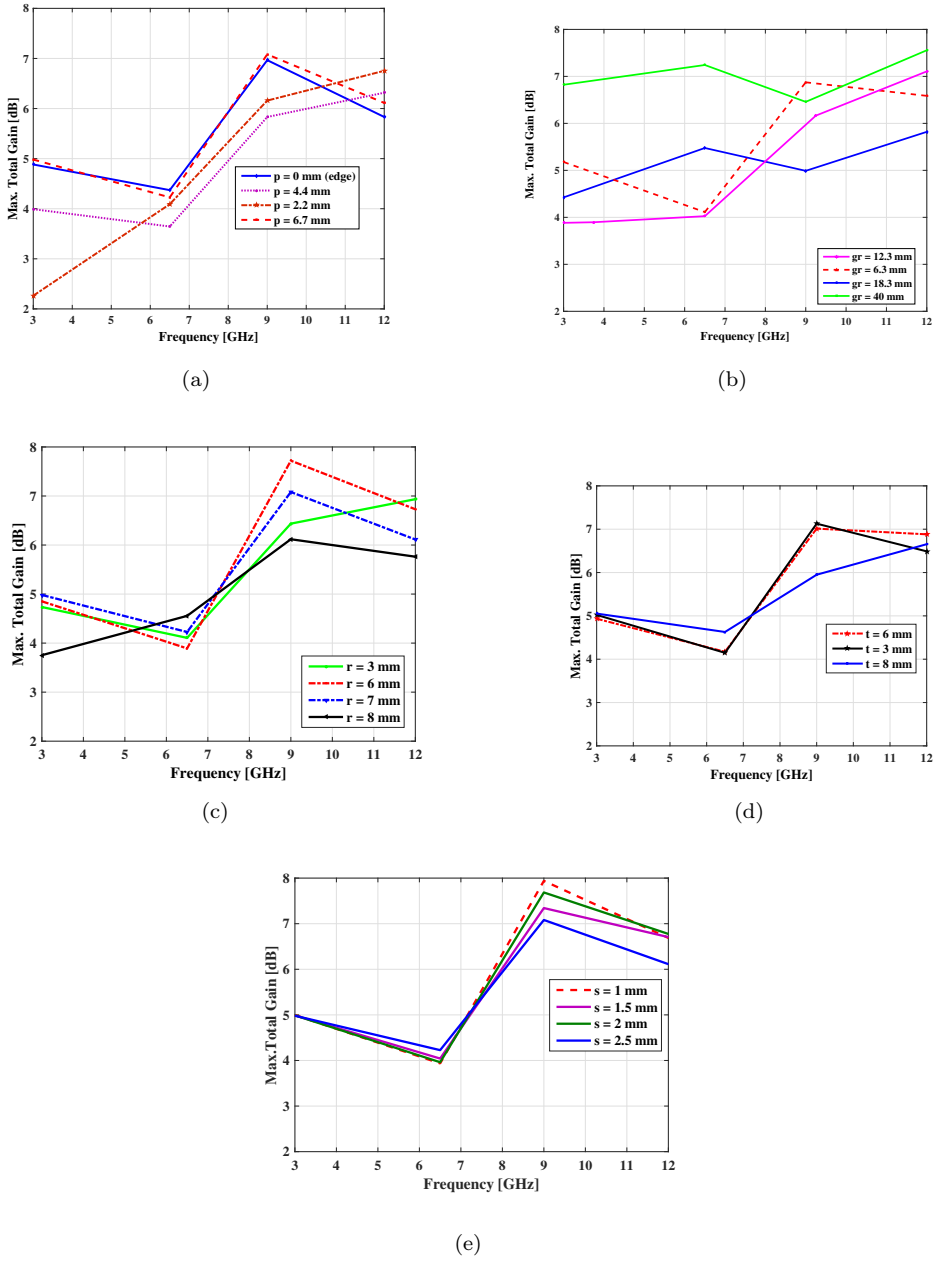


FIGURE 3.6: Effect of design parameters $p$, $g_r$, $r$, $t$ and $s$ on antenna gain with the optimised parameters (**red dotted line**) by changing one parameter at a time. Changing with respect to (a) feeding positions $p$, (b) ground length $g_r$, (c) slot radius $r$, (d) Q-descender $t$, (e) slot width $s$.

We also examined the effect of Q-slot parameters on antenna return loss. With reference to Fig. 3.7, optimising the antenna parameters can result in a return loss below -10dB with good matching characteristics and VSWR $< 2$ from 3.1 GHz to 11.7 GHz. The return loss plots suggest that all parameters have significant effect on the antenna

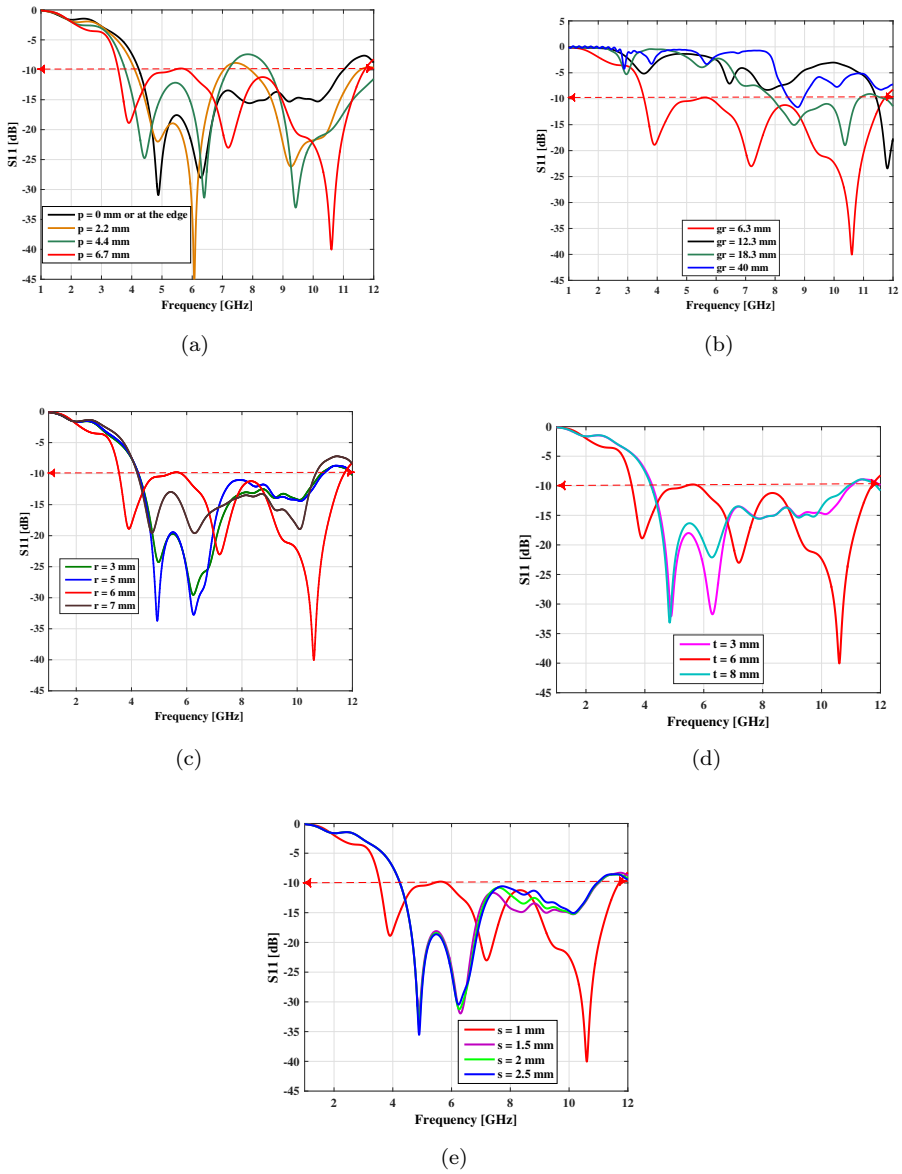


FIGURE 3.7: Effect of design parameters $p$, $g_r$, $r$, $t$ and $s$ on antenna $S_{11}$ with the optimised parameters (**red line**) by changing one parameter at a time. Changing with respect to (a) feeding positions $p$, (b) ground length $g_r$, (c) slot radius $r$, (d) Q-descender $t$, (e) slot width $s$.

resonance behaviour. Feeding positions $p$ at 6.7 mm or at the edge (0 mm) result in a return loss under -10 dB for the UWB spectrum of 3.1-10.6 GHz, while all other positions result in values exceeding -10 dB for a portion of the spectrum. With regards to the ground plane length $gr$, a satisfactory UWB range is only achieved at 6.3 mm. Finally, changes in the Q-slot parameters $r, s$ and $t$ do not affect the -10 dB requirement severely, but they have strong impact on the antenna input impedance and resonant frequencies. After careful analysis of the effect of these parameters on the antenna performance, we finalised the antenna design based on the optimised dimensions shown in Table 3.1.

## 3.3 Simulated and Measured Performance

### 3.3.1 Simulated and Measured Return Loss in Free Space

Fig. 3.8 shows the prototype of PRMA with Q-slot and the measurement setup. The antenna was experimentally characterised by a Keysight M9375A vector network analyser (VNA). The antenna was simulated between 2 GHz-12 GHz, as this was the initial UWB spectrum of interest. However, our measurements showed that the antenna return loss is under -10 dB for frequencies up to 20 GHz.

As shown in Fig. 3.9 (a), there is a very good agreement between the simulated and measured results across the whole UWB spectrum. Fig. 3.9 (b) demonstrates that the measured return loss is below -10 dB for up 20 GHz.

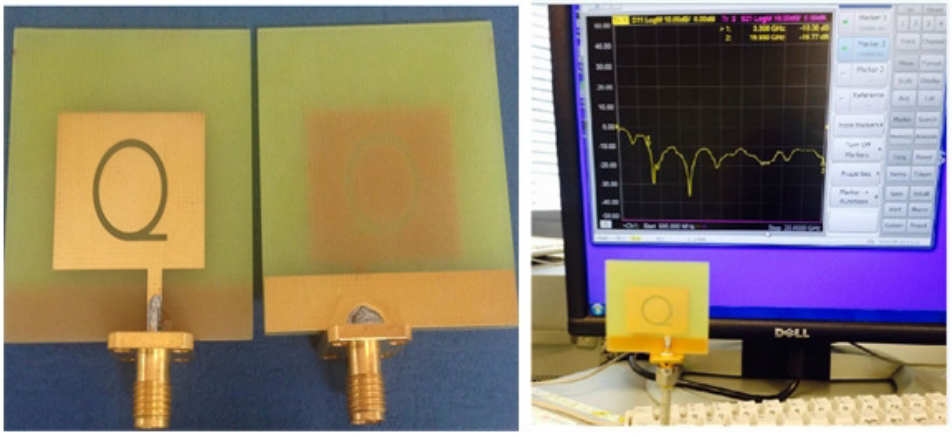


FIGURE 3.8: Fabricated prototype of PRMA with Q-slot and free space measurement setup

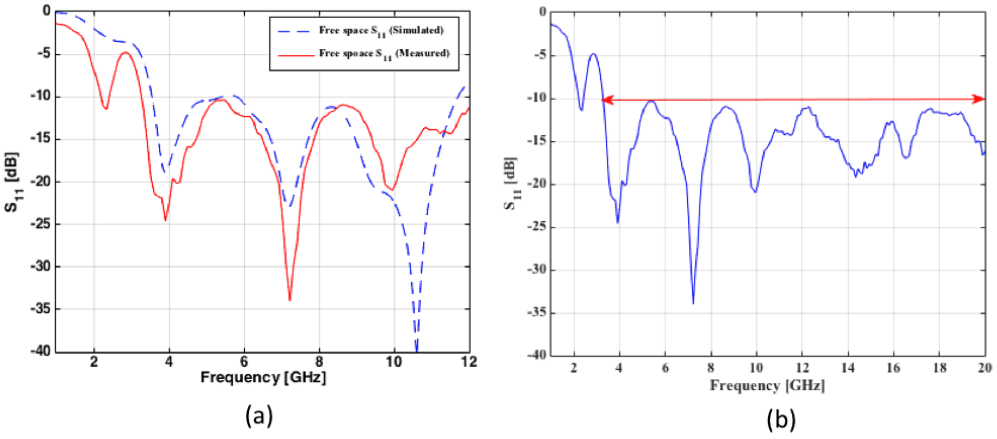


FIGURE 3.9: (a) Free space simulated and measured $S_{11}$ of PRMA with Q-slot up to 12 GHz. (b) Free space measured $S_{11}$ of PRMA with Q-slot up to 20 GHz.

### 3.3.2 Simulated Return Loss on Body

To study the antenna performance for on-body applications, we considered a three-layer phantom composed of wet skin ($\varepsilon_r = 41.982, \sigma = 2.0168$), fat ($\varepsilon_r = 5.2138, \sigma = 0.13497$) and muscle ($\varepsilon_r = 51.936, \sigma = 2.2216$) calculated at the lower-edge of UWB spectrum 3.1 GHz [12]. We take into account that this is only an approximate tissue model, since the tissue properties are not constant across the whole frequency range. The dimensions of the phantom (50 mm x 50 mm x 400 mm) are equivalent to a human arm model considered in [13, 14] as shown in Fig. 3.10 (a). Using this model, we calculated the antenna return loss when placed on or very close to the human body. The separation gap between the antenna and the phantom was varied between 3 mm to 15 mm, and the calculated return loss for the various positions is plotted in Fig. 3.10(b). The results show that the proposed antenna maintains reasonable performance in close proximity to the tissue which suggest that this antenna could be very candidate for on-body applications.

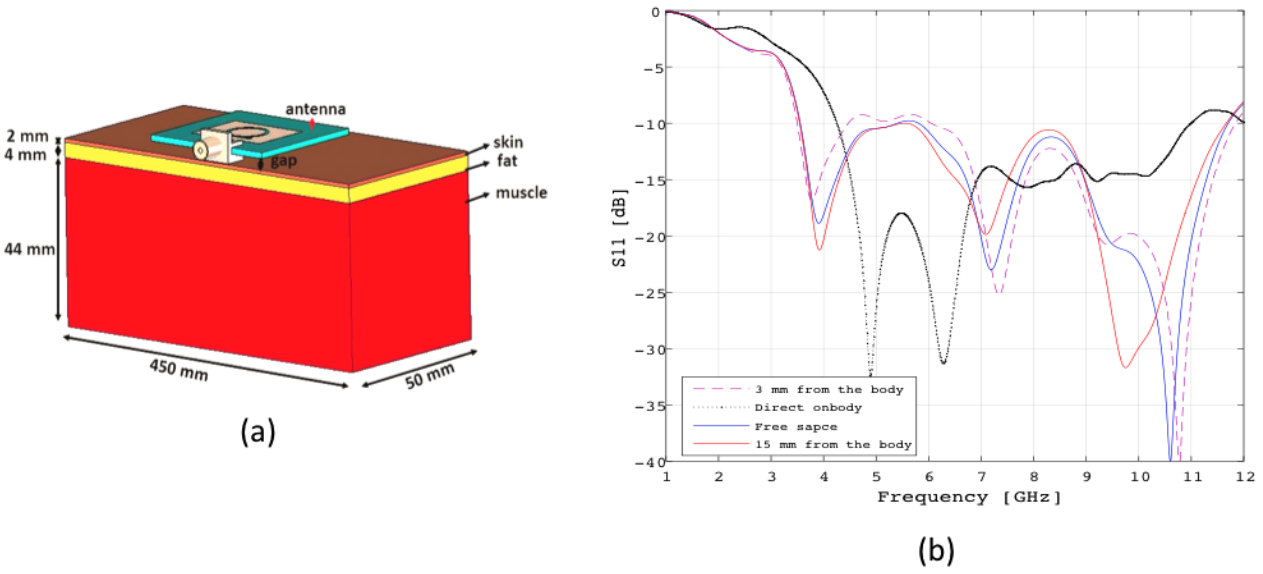


FIGURE 3.10: Simulated on-body performance of the proposed antenna (a) Antenna and three-layer phantom model for on-body simulations (b) Corresponding calculated return loss for various values of the gap between the antenna and the phantom.

### 3.3.3 Measured Results for On-body Performance

For on-body measurements we attached the antenna parallel onto the chest of a male human volunteer ( age = 35 years, weight = 81 kg, height = 172 cm, BMI = 27) in standing position. We took the measurements by varying the distance from the chest from 3 to 15 mm as shown in Fig. 3.11(a). In addition to the chest measurements we carried out direct on-body measurements on different parts of the body such as arm and wrist (Fig. 3.11(b-d)). The results from these measurements are plotted in Fig. 3.12(a), where it is shown that the antenna maintains its UWB operation in the presence of the human body. Moreover, the measured on-body data for different body parts plotted in Fig. 3.12(b) confirms the antenna's UWB operation from 3.1 GHz to 20 GHz.

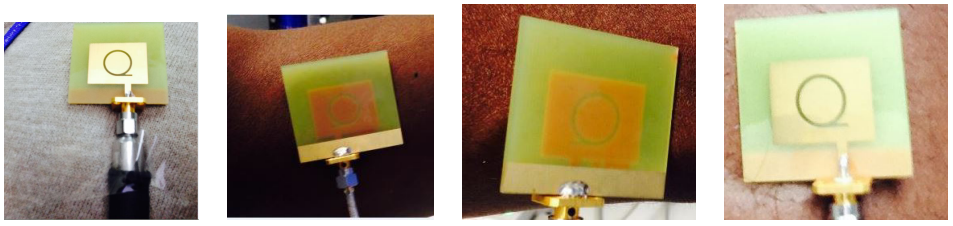

(a) Human chest with clothes on (b) Human arm (c) Human wrist (d) Human chest without clothes

FIGURE 3.11: Photographs of the measurements when the antenna was placed on different parts of the body

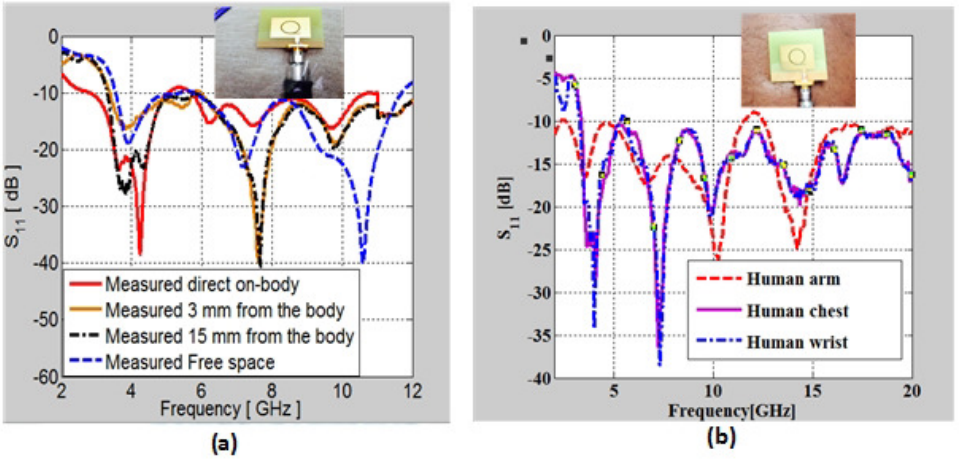


FIGURE 3.12: (a) Measured $S_{11}$ when the antenna was placed on human subject with varied gap (b) Direct on-body measured $S_{11}$ (up to 20 GHz) on different parts of the body.

### 3.3.4 Radiation patterns

The antenna radiation pattern in the azimuth plane and elevation plane were evaluated both in free space and on-body at representative frequencies 3.1 GHz, 6.5 GHz and 9 GHz. Fig. 3.13 shows the on-body simulated and measured azimuthal and elevation plane radiation pattern at the aforementioned frequency points. At lower frequencies, the radiation pattern in azimuth plane plane is more directive while at higher frequencies (e.g. 9 GHz), the pattern is quasi-omnidirectional. Both the simulated and on-body measurement agree at the selected frequencies. In the elevation plane plane, the radiation pattern at the selected frequencies are more or less omnidirectional. There is also a good agreement between the measured and the simulated results.

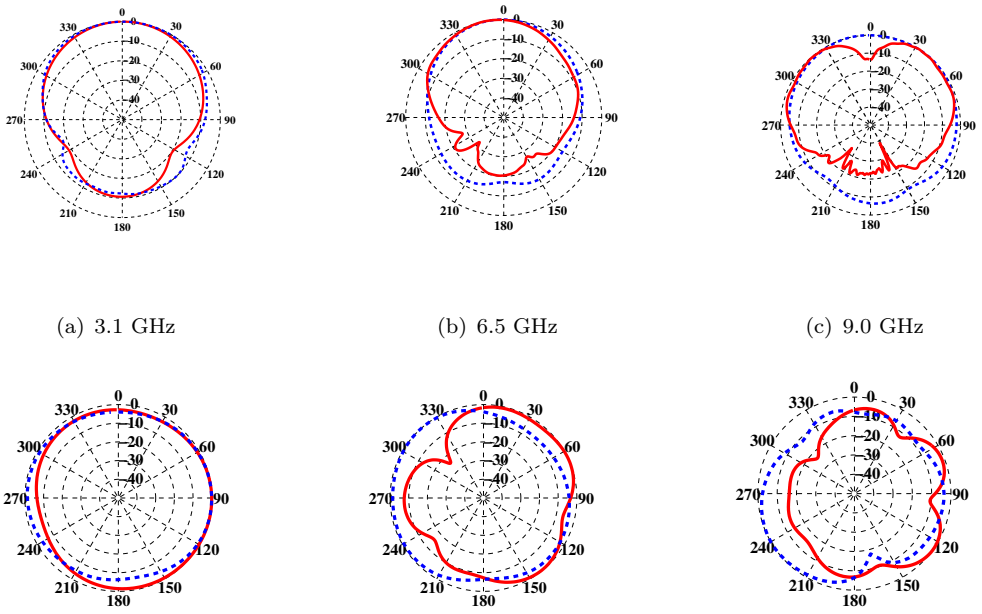

(a) 3.1 GHz (b) 6.5 GHz (c) 9.0 GHz

(d) 3.1 GHz (e) 6.5 GHz (f) 9.0 GHz

FIGURE 3.13: Measured and Simulated radiation patterns (**blue dotted line free space simulated** ), (**red solid line on-body measurement**) at 3.1 GHz, 6.5 GHz and 9 GHz. (a-c) azimuth plane, (d-f) elevation plane. The antenna was placed on-body and 3 mm away from the human chest

### 3.3.5 Operation in the Presence of a Breast Phantom

We also performed measurements to evaluate the antenna performance on a breast tissue mimicking phantom, shown in Fig. 3.14. The breast phantom was prepared from the materials listed on Table 3.3 showing the percentages by weight of all the components [15]. The hemispherical breast phantom had a diameter of 14 cm and a depth of 10 cm (see Fig. 3.14). The measured permittivity and conductivity of the breast phantom across the UWB spectrum is shown in Fig. 3.14. The return loss of the antenna on the breast phantom is shown in Fig. 3.15, which shows that the antenna once again maintains its UWB operation across the range from 2-10 GHz.

TABLE 3.3: Composition of tissue-mimicking materials. Abbreviations: v: volume, w: weight, A: p-toluic acid, B: n-propanol, C: gelatin, D: formaldehyde, E: oil, F: surfactant, G: water

| v% oil | w%A | w%B | w % C | w% D | w% E | w % F | w % G |
|---|---|---|---|---|---|---|---|
| 50 | 0.045 | 1.81 | 7.69 | 0.18 | 44.42 | 2.89 | 42.96 |

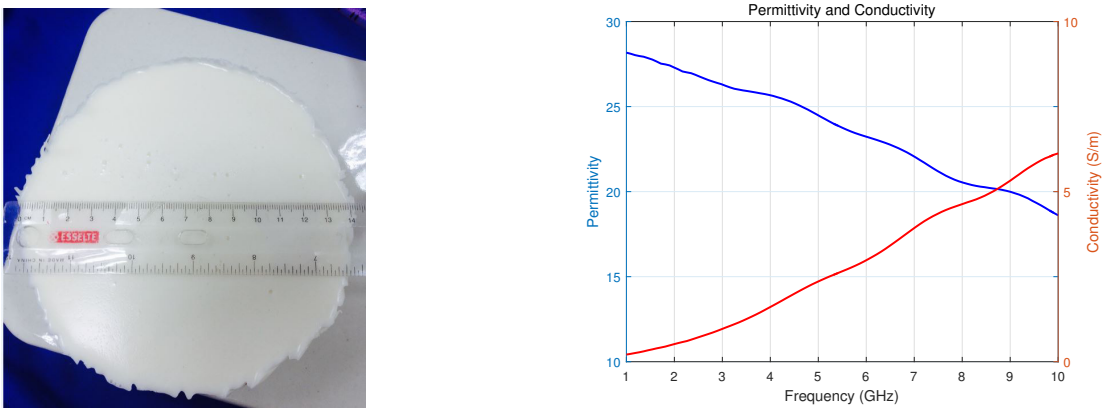


FIGURE 3.14: Photo of the homogeneous breast phantom and the corresponding dielectric propoerties

In addition to breast phantom measurements, we also performed measurements using matching liquid made up of 90% glycerine and 10% water. We measured the properties of the liquid in the UWB spectrum with measurement set-up shown in Fig. 3.16(a) and Fig 3.16(b) shows the measured liquid properties . For the measurements, the antennas were initially placed outside the tank containing the matching liquid as shown

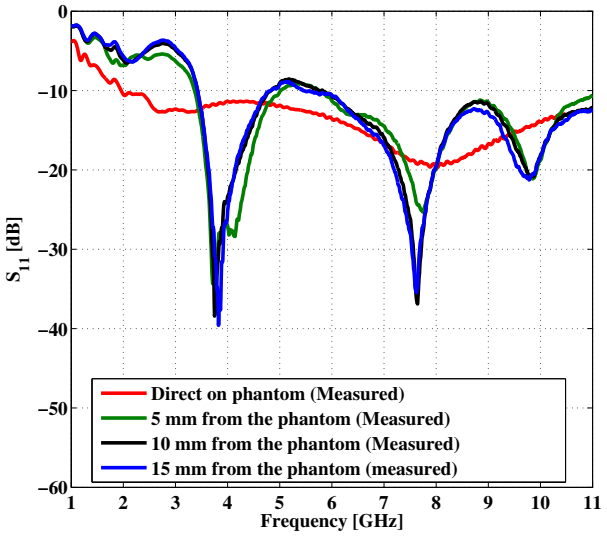


FIGURE 3.15: Measured return loss of the antenna in the presence of the breast mimicking phantom

in Fig.3.17[1] with the distance between the antennas in the measurement set up was 15 cm. We observed the response and the results show that the antenna performance is consistent with simulated results.

We also fully immersed the antenna in the matching liquid and once again the antenna shows consistent results. Fig. 3.18(a) shows the measured reflection coefficient of the antenna in presence of matching liquids. Fig. 3.18(b) shows the transmission from antenna 1 to antenna 2 when the antennas were mounted on the liquid tank. When the antennas were fully immersed in the matching liquid, the transmission was weaker than in free space, this is due to the lossy nature of the liquid. We summarise the performance of the printed Q-slot antenna in Table 3.4.

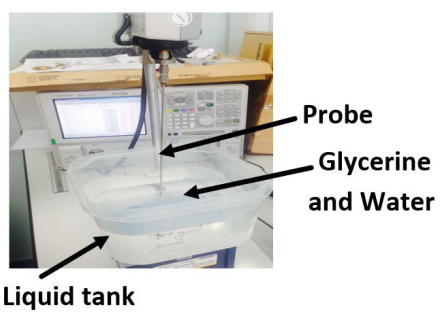


(a) Measurement set up

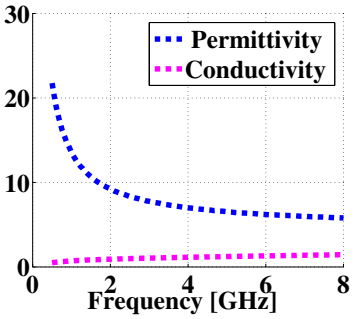


(b) Properties of the liquid

FIGURE 3.16: Photo of the liquid phantom measurement set-up and plot of its dielectric properties. The liquid is made up of 90% glycerol and 10% water.

[1] Kind Courtesy of MediWise UK Ltd

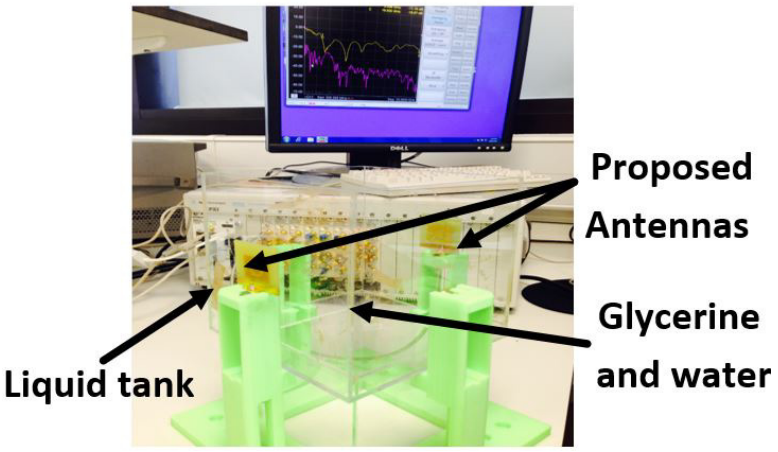


FIGURE 3.17: Measurement set-up for the antenna with the matching liquid. The antennas were placed outside the tank at 15 cm distance between them.

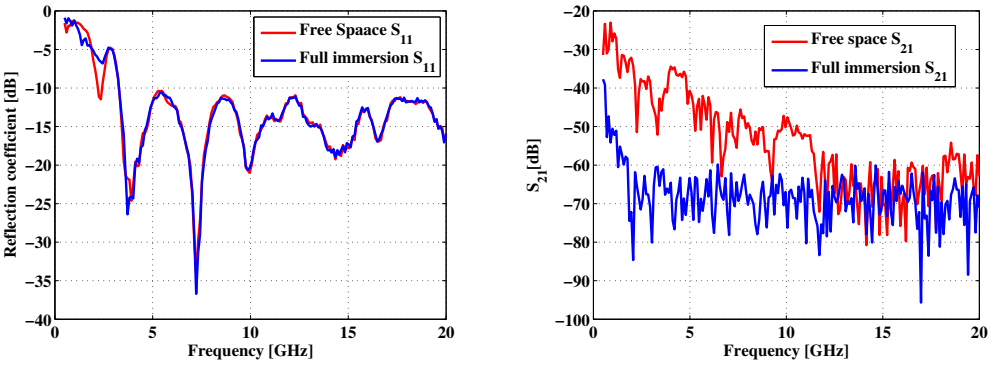


(a) Measured reflection coefficient

(b) Measured $S_{21}$

FIGURE 3.18: (a) Measured return loss of the antenna in the presence of the liquid phantom (b) Measured transmission coefficient of the antenna in the presence of the liquid phantom.

TABLE 3.4: Performance of Q-slot monopole in free space and on the body

| Paramter | Free Space | On-body (Phantom) |
|---|---|---|
| Resonance Frequency (GHz) | Simulated 3.8<br>Measured 3.8 | Simulated 4.45<br>Measured 4.20 |
| Bandwidth (-10 dB) GHz | Simulated 7.7<br>Measured (from 3.1-20) 17.9 | Simulated 6.5<br>Measured 17.5 |
| Gain (dBi) | Simulated 3.8 @ 3.1 GHz<br>4.2 @ 6.5 GHz<br>6.4 @ 9.0 GHz<br>Measured 3.5 @ 3.1 GHz | Simulated -8.2 @ 3.1 GHz<br>-6.4 @ 6.5 GHz<br>-2.5 @ 9.0 GHz<br>Measured -9.3 @ 3.1 GHz |
| Total efficiency (%) | 98 at 9.0 GHz | 52 at 9.0 GHz |

## 3.4 Time-Domain Characteristics

The performance of UWB antennas rely on the quality and the shape of the received signals relative to a source signal. By post processing the scattered signals and compare it against a source signal, the system could be used to characterise an object. Therefore, it is important to quantify the level of distortion of the radiated signals in the time-domain. In this section, we quantify the time-domain performance of the proposed UWB antenna by analysing its impulse response and pulse fidelity.

### 3.4.1 Review of Gaussian Pulse Signals

Gaussian pulse is one of the commonest signals used to excite UWB antennas due to their unique properties in terms of time domain and frequency spectrum performance.

A Gaussian pulse signal is mathematically described as (3.4):

$$V(t) = e^{-}\left(\frac{t-d}{b}\right)^2 \tag{3.4}$$

where $b$ is the pulse width, $d$ is the pulse shift and $t$ is time duration.

Fig. 3.19 shows the time-domain representation of a Gaussian pulse with $b = 100$ ps. The corresponding power spectral density is also shown in Fig. 3.20, which shows that basic Gaussian pulse will not fit the power spectral density mask set by the FCC for UWB antennas.

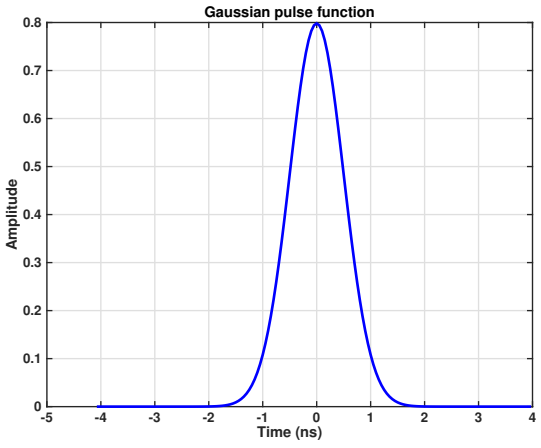


(a) Gaussian pulse

FIGURE 3.19: Time-domain representation of a Gaussian pulse

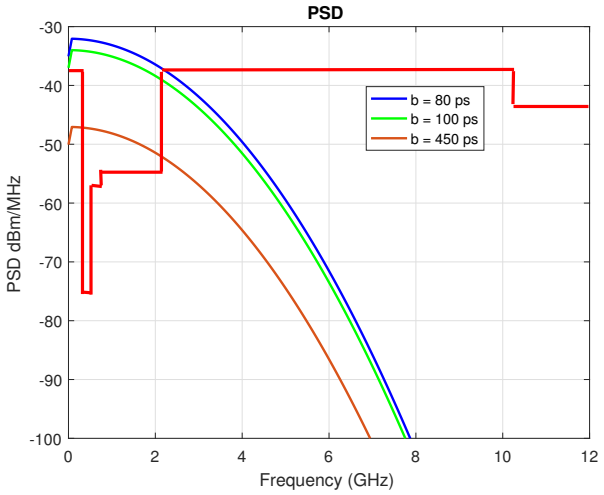


FIGURE 3.20: Frequency-domain representation of a Gaussian pulse with different pulse widths

To reduce high values in the power spectrum, Gaussian pulse derivatives are commonly used. Here we investigate Gaussian pulse derivatives with different pulse widths in compliance with FCC regulations. Equations (3.5-3.6) represent Gaussian first and second derivatives. We plotted the pulse with different widths as shown in Fig. 3.21 with the corresponding power spectral density shown in Fig. 3.22, which shows that the first and second derivatives of Gaussian pulses do not satisfy the FCC mask. The power spectral density of the pulses do not cover the entire FCC mask more especially from 0.96 GHz to 1.61 GHz. Other studies [16, 17], have shown that higher order Gaussian derivatives satisfy FCC regulations, however, more noise and distortion are introduced with more filters. For this reason, we will not investigate high order Gaussian derivatives but will adopt sine-modulated means to meet FCC requirements.

$$V(t) = \left[ -\frac{2(t-d)}{b^2} \right] e^{-\left(\frac{t-d}{b}\right)^2} \tag{3.5}$$

$$V(t) = \left[ -\frac{2}{b^2} + \frac{4(t-d)^2}{b^4} \right] e^{-\left(\frac{t-d}{b}\right)^2} \tag{3.6}$$

In order to comply with FCC emission limit on UWB antennas, the baseband Gaussian pulse is modulated with sinusoidal carrier as (6.4)

$$V_{mod}(t) = \left[ sin(2\pi f_c t) \right] e^{-\left(\frac{t-d}{b}\right)^2} \tag{3.7}$$

where $b$ is the pulse width, $t$ is the time length, $d$ is the time delay and $f_c$ is the modulated frequency.

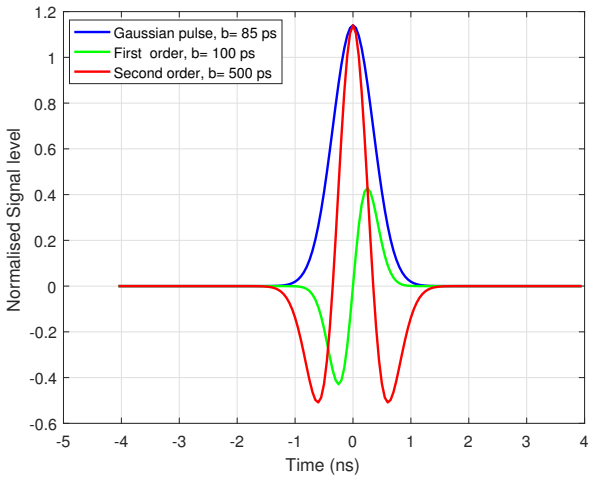


FIGURE 3.21: Gaussian pulse derivatives with different pulse width

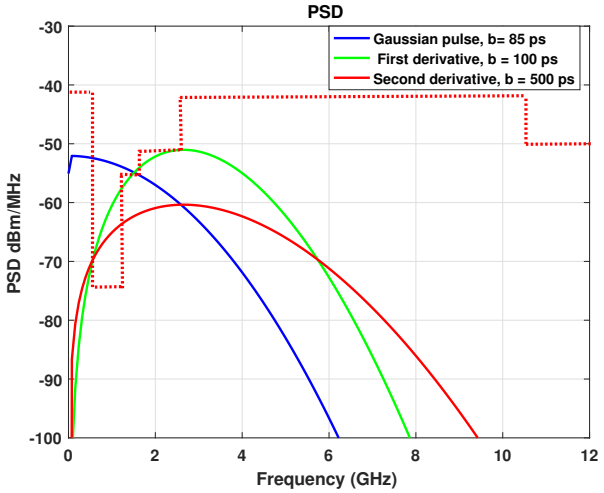


FIGURE 3.22: Frequency domain representation of Gaussian pulse derivatives

We modulated the input signal at the following frequencies 4.5 GHz and 6.5 GHz with $b = 220$ ps and $d = 180$ ps. Fig. 3.23 shows the modulated Gaussian pulse and its corresponding power spectral density (PSD) with the FCC emission mask is shown in Fig. 3.24. The PSD of the modulated signal matches well with the FCC regulation. With this method the baseband Gaussian pulse fits the operating centre frequency with the option of adjusting the signal bandwidth.

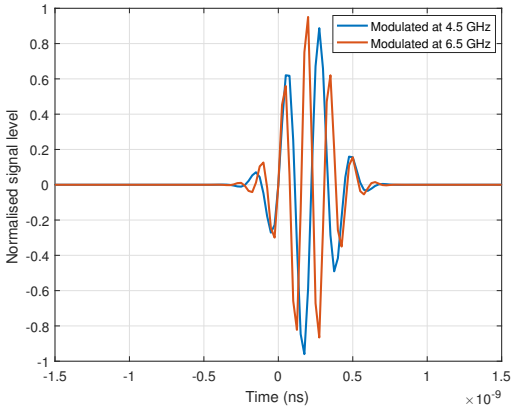


FIGURE 3.23: Sine-modulated Gaussian pulse at 4.5 GHz and 6.5 GHz

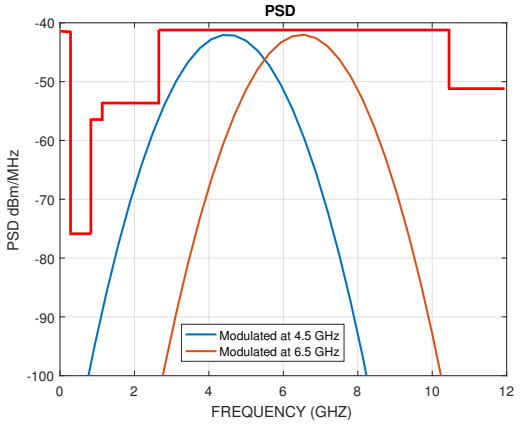


FIGURE 3.24: Power spectral density of the modulated Gaussian pulse at 4.5 GHz and 6.5 GHz

### 3.4.2 Antenna Pulse Fidelity

In UWB system the pulse emitted by the transmitting antenna is exposed to distortion that affect the quality of the signal receive by the receiving antenna. In analysing the spatial capacity of UWB systems, a measure frequently used to analyse the degree of similarity between the original pulse and the received pulse in the time domain is the fidelity. For a UWB antenna, fidelity is a figure of merit use to access the quality of the design and its ability to maintain pulse shape. From a systems point of view, UWB antenna systems should transmit and receive high-quality signals for high signal-to-noise ratio (SNR) at a receiver. In practice, signal fidelity is calculated for a given direction in space in order to fully characterise the spatial radiation properties of an antenna.

According to [18], an antenna fidelity is defined as the cross-correlation of input signal and the received signal that have been normalised by their energy. Thus, the fidelity corresponds to the peak cross-correlation of the excitation signal and the output signal. This allows us to compare the shape of the pulses independently of their amplitude. It

also enables us to address the characteristics of transmit and receive antennas, as well as antenna system response.

The fidelity $F$ is expressed mathematically as:

$$F = \ max_{\ \tau}\left[\frac{\int_{-\infty}^{+\infty} x(t)\cdot y(t-\tau)\cdot dt}{\sqrt{\int_{-\infty}^{+\infty}|x(t)|^2\cdot dt\int_{-\infty}^{+\infty}|y(t)|^2\cdot dt}}\right] \tag{3.8}$$

For the antenna fidelity calculation, we used CST field probes that were placed at the far-field of the transmitting antenna to receive the radiated signals. Fig. **??** shows the input and received signals of the proposed antenna. The signals were cross-correlated using CST Microwave Studio and the result is shown in Fig. **??**. We investigated the antenna fidelity in three different directions i.e $(\theta = 0°, \phi = 0°)$, $(\theta = 0°, \phi = 90°)$, and $(\theta = 90°, \phi = 90°)$. The peak value or maximum correlation represents the fidelity of the antenna. As has been shown in Fig. 3.25, the antenna fidelity ranges from 0.6588 to 0.9531, thus 65.88% to 95.31% which is within the acceptable range of 90% and above for UWB antennas [19].

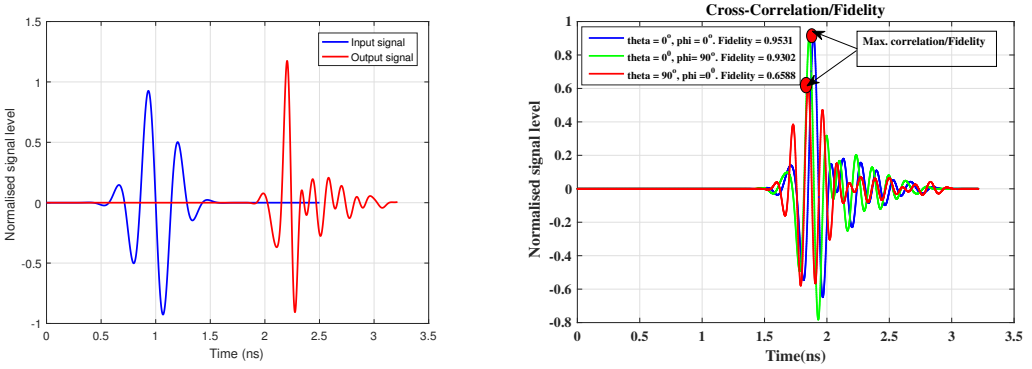


(a) Input and output signal

(b) Cross-correlation of input and output signals

FIGURE 3.25: (a) Input and output signal. (b) The signals were cross-correlated to show the peak value representing the antenna fidelity in three different directions.

### 3.4.3 Antenna Impulse response

In radio channel propagations, the system can be represented in three stages or blocks as shown in Fig. 3.26 [20], the transmitting antenna $(Tx)$ , the radio channel $(CH)$, and the receiving antenna $(Rx)$. The impulse response of an antenna can be derived from the transfer function $H_{(f)}$ by using an Inverse Fast Fourier Transform (IFFT) [21]. The results can easily be deduced from the measurements.

The transfer function for $Tx$ and the channel $CH$ relate the input voltage to the electric far-field in the desired direction as expressed in equation (3.9):

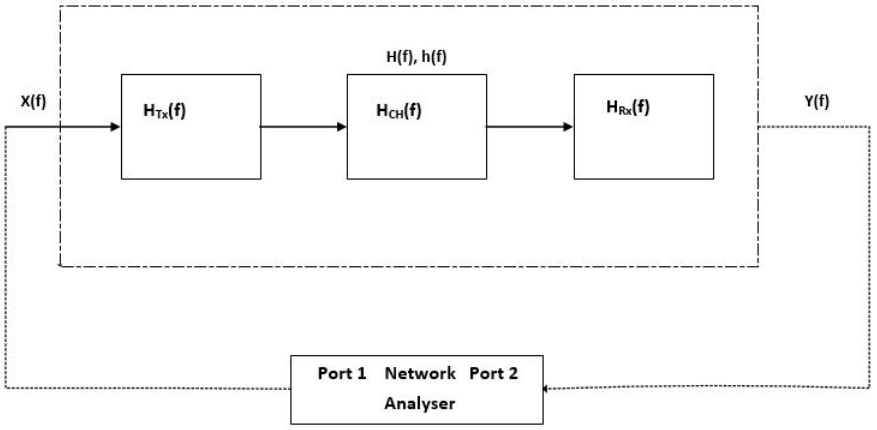


FIGURE 3.26: A simple block diagram of UWB communication link [20]

$$\hat{H}_{Tx|Ch} = \hat{H}_{Tx}(f)\hat{H}_{CH}(f) = \frac{\hat{E}(f)}{V_{Tx}(f)} \tag{3.9}$$

where $\hat{E}(f)$ and $V_{Tx}$ are the Fourier transform of the electric field and input voltage respectively.

In a similar fashion, a vector transfer function for $Rx$ is defined as equation (3.10)

$$\hat{H}_{Rx}(f) = \frac{V_{out}(f)}{\hat{E}(f)} \tag{3.10}$$

The relationship between the input voltage to $Tx$ and the received voltage at the receiver $Rx$ can be calculated as equation (3.11).

$$H(f) = H_{Tx}(f)H_{CH}(f)H_{RX}(f) = \frac{Y(f)}{X(f)} = S_{21} \tag{3.11}$$

Using Inverse Fast Fourier Transform (IFFT), the impulse response $h[n]$ is calculated from the real part of equation (3.11) as;

$$h[n] = Re\{IFFT[H(f)]\} \tag{3.12}$$

### 3.4.4 Simulated Impulse Response of the PRMA with Q-slot

In order to characterise the transient performance of the antenna, spatially metrics such as impulse response can be used as optimisation goal to quantify the time-domain response. The free space channel between two identical antennas were set face-to-face with a separation distance of 50 cm, which is about five times the wavelength at the lowest frequency ( 3 GHz), the most appropriate setting for WBAN applications [22].

Two Q-slot antennas were put face-to-face to do the impulse response analysis as shown in Fig. 3.27. The antennas were simulated in CST Microwave Studio. Different separation distances $d$ between the antennas were taken into consideration. We evaluated the amplitude and phase of the transmission coefficients $S_{21}$ as shown in Fig. 3.28. As has been shown, both the amplitude and phase have smooth and linear features implying that transmitted signal has less distortion across the operating spectrum.

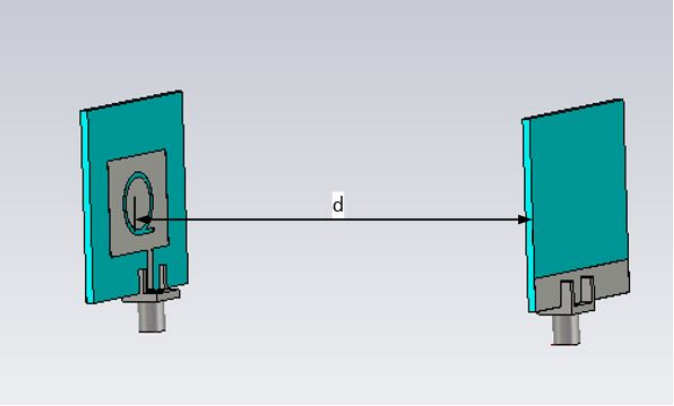


FIGURE 3.27: Two PRMA with Q-slot in face-to-face alignment for impulse response simulation

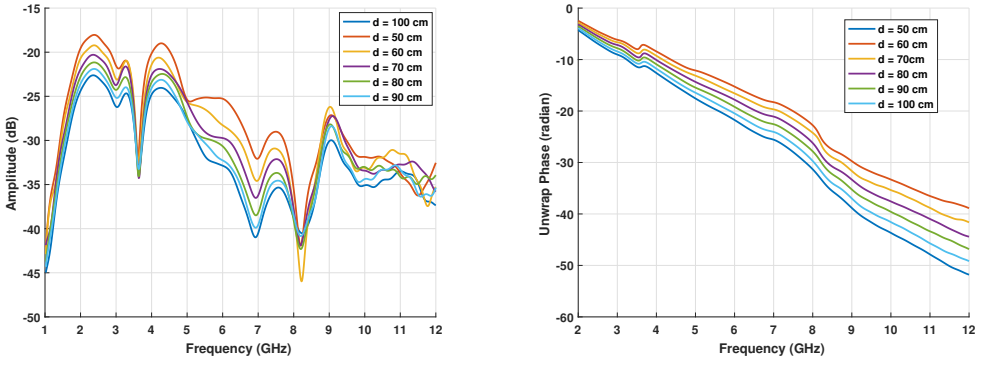


(a) Amplitude of the transmission coefficient ($S_{21}$ ) of the PRMA with Q-slot in face-to-face orientation

(b) The unwrap phase of $S_{21}$

FIGURE 3.28: The impulse response of the antenna showing (a) $S_{21}$, and (b) unwrap phase

### 3.4.5 Measured Impulse Response of PRMA with Q-Sslot

There are two different techniques that can be used to measure the impulse response, direct time measurement using fast sampling and oscilloscope, and frequency domain measurement using network analyser. For this measurement, we used the latter approach, frequency domain and network analyser.

In the measurement, we attached two PRMA with Q-slot to port 1 and port 2 of Keysight M9375A Vector Network Analyser (VNA) with a separation distance of at least 50 cm between the antennas. The network analyser was swept in the desired frequency range of 3-12 GHz with sampling rate at 1700 and sweep time of 800 ms. We store the magnitude of the transmitter $Tx$ and the receiver $Rx$. We measured the response of two antennas by aligning them face-to-face at a separation distance of 50 cm to confirm the simulated results. Also to access and evaluate the impulse response and fidelity in different directions, we performed other measurements by aligning the antennas in different orientations keeping the same distance of 50 cm between them (See Fig. 3.29). The antenna performance was evaluated by comparing the simulated and measured transmission coefficient ($S_{21}$) when the antennas were oriented face-to-face with 50 cm distance between them, the result has been shown in Fig. 3.30. As has been shown there is a good agreement between the $S_{21}$ with an isolation of at least -20dB.

We post processed the fidelity from the measured results using MatLab software package. The fidelity of the system impulse response were calculated in different orientations according to the measurements. In side-by-side orientation the fidelity was 95.1%, and when the antennas were face-to-face it was 97.6%. In all cases, the results show that the antenna exhibits high fidelity in different orientations.

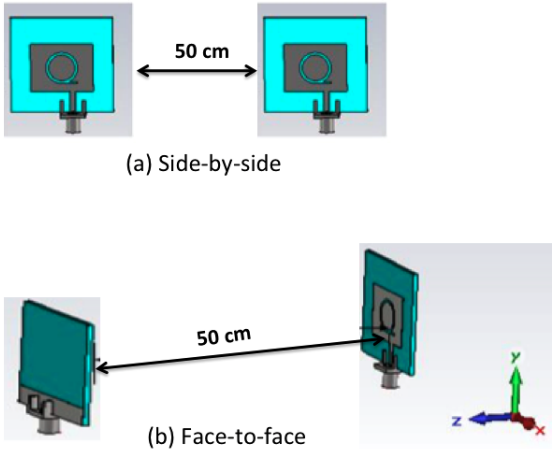


FIGURE 3.29: Transfer function set up with two identical antennas with a separation distance of 50 cm between them and different orientations

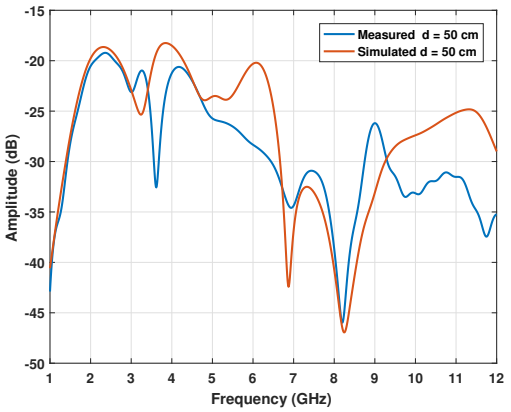


FIGURE 3.30: Simulated and measured transmission coefficient of two PRMA with Q-slot in face-to-face orientation with a separation distance of 50 cm between them

## 3.5 Summary

In this chapter, we looked at the on-body performance of PRMA with Q-slot by using real human as a test subject. Experimental investigation was made by taking on-body measurements on the chest of the human subject. We also measured the performance of the antenna on different parts of the body. The results demonstrate the resilient of the antenna in presence of human body. The Q-slot on the radiator generated overlapping and closely spaced resonances that account for UWB characteristics and resilience to body detuning. We also tested the antenna in the presence of breast phantom and matching liquid. The results once again demonstrate the resilient of the antenna in these environments, which suggest that the PRMA with Q-slot could be a good candidate for microwave imaging applications.

We evaluated the time-domain characteristics of the proposed antenna. The PRMA with Q-slot was designed to radiate less distortion signals by optimising the slot parameters together with the ground plane to provide smooth signal transition and impedance matching network across the spectrum. It has been shown that by using modulated Gaussian signal, the Q-slot antenna satisfies the entire spectrum of UWB as defined by FCC. Furthermore, the chapter also demonstrated that a system composed of two identical PRMA with Q-slot can achieve a fidelity factor of 95% on average.

# References


[1] F. Gustrau and D. Manteuffel, *EM Modelling of Antennas and RF Components for Wireless Communication Systems - A Practical Guide. Series: Signals and Communication Technology.* Springer, 2006.

[2] K. P. Ray, P. V. Anob, R. Kapur, and G. Kumar, "Broadband planar rectangular monopole antennas," *Microwave and Optical Technology Letters*, vol. 28, no. 1, pp. 55–59, 2001.

[3] J. Liang, C. C. Chiau, X. Chen, and C. G. Parini, "Study of a printed circular disc monopole antenna for uwb systems," *IEEE Transaction Antennas and Propagation*, vol. 53, pp. 3500–3504, November 2005.

[4] P. Li, J. Liang, and X. Chen, "Study of printed elliptical/circular slot antennas for ultra wideband applications," *IEEE Transaction Antennas and Propagation*, vol. 54, pp. 1670 – 1675, June 2006.

[5] P. Li, J. Liang, and X. Chen, "Ultra-wideband elliptical slot antenna fed by tapered micro-strip line with u-shaped tuning stub," *Microwave and Optical Technology Letters*, vol. 47, pp. 140–143, October 2005.

[6] N. P. Agrawall, G. Kumar, and K. P. Ray, "Wide-band planar monopole antennas," *IEEE Transactions on Antennas and Propagation*, vol. 46, pp. 294–295, February 1998.

[7] R. Bhalla and L. Shafai, "Broadband patch antenna with a circular arc shaped slot," in *Antennas and Propagation Society International Symposium, 2002. IEEE*, vol. 1, pp. 394–397 vol.1, 2002.

[8] B.Yeboah-Akowuah, E. Kallos, G. Palikaras, C. Yifan, and P. Kosmas, "A novel compact planar inverted-F antenna for biomedical applications in the mics band," in *Antennas and Propagation (EuCAP), 2014 8th European Conference*, pp. 822–824, April 2014.

[9] K. F. Lee, S. Yang, A. A. Kishk, and K. M. Luk, "The versatile u-slot patch antenna," *Antennas and Propagation Magazine, IEEE*, vol. 52, pp. 71–88, Feb 2010.

[10] S. Weigand, G. Huff, K. Pan, and J. Bernhard, "Analysis and design of broad-band single-layer rectangular u-slot microstrip patch antennas," *Antennas and Propagation, IEEE Transactions*, vol. 51, pp. 457–468, March 2003.

[11] A. Deshmukh and K. Ray, "Analysis of broadband variations of u-slot cut rectangular microstrip antennas," *Antennas and Propagation Magazine, IEEE*, vol. 57, pp. 181–193, April 2015.

[12] "Calculation of the dielectric properties of body tissues," institute for applied physics, italian national research council." website. http://niremf.ifac.cnr.it/tissprop.

[13] C. H. Lin, K. Saito, M. Takahashi, and K. Ito, "A compact planar inverted-f antenna for 2.45 ghz on-body communications," *Antennas and Propagation, IEEE Transactions on*, vol. 60, pp. 4422–4426, Sept 2012.

[14] B.Yeboah-Akowuah, P. Kosmas, and C. Yifan, "A low profile microstrip patch antenna for body-centric communications at 2.45 GHz band," in *Antennas and Propagation (EuCAP), 2015 9th European Conference*, pp. 1–3, April 2015.

[15] M. Lazebnik, E. L. Madsen, G. Frank, and S. C. Hagness, "Tissue mimicking phantom and materials for narrowband and ultrawideband microwave applications," *Phys.Med.Biol*, vol. 50, August 2005.

[16] M. Mirshafiei, M. Abtahi, and L. A. Rusch, "Ultra-wideband pulse shaping: bypassing the inherent limitations of the gaussian monocycle," *IET Communications*, vol. 6, pp. 1068–1074, June 2012.

[17] D. D. Wentzloff and A. P. Chandrakasan, "Gaussian pulse generators for subbanded ultra-wideband transmitters," *IEEE Transactions on Microwave Theory and Techniques*, vol. 54, pp. 1647–1655, June 2006.

[18] D. Lamensdorf and L. Susman, "Baseband-pulse-antenna techniques," *IEEE Antennas and Propagation Magazine*, vol. 36, pp. 20–30, Feb 1994.

[19] H. Fallahi and Z. Atlasbaf, "Study of a class of uwb cpw-fed monopole antenna with fractal elements," *IEEE Antennas and Wireless Propagation Letters*, vol. 12, pp. 1484–1487, 2013.

[20] A. H. Mohammadian, A. Rajkotia, and S. S. Soliman, "Characterization of uwb transmit-receive antenna system," in *Ultra Wideband Systems and Technologies, 2003 IEEE Conference on*, pp. 157–161, Nov 2003.

[21] T. Yang, S.-Y. Suh, R. Nealy, W. Davis, and W. L. Stutzman, "Compact antennas for uwb applications," *2003 IEEE Ultra Wideband Systems and Technologies*, pp. 205–208, November 2003.

[22] J. McLean, H. Foltz, and R. Sutton, "Pattern descriptors for uwb antennas," *IEEE Transaction Antennas and Propagation*, vol. 53, pp. 553–559, January 2005.

# Chapter 4

# Spline Curve UWB Monopoles for Microwave Imaging

As has been discussed in chapter **2**, section 2.4.1, different kinds of antennas such as monopoles, bow-tie, slot, patch antennas and vivaldi antennas have been proposed for microwave imaging [1–4]. Although some of these antennas have excellent performance they are seldom used in portable devices because of bulky size and unconformity. Planar monopoles are becoming alternative choice for many applications, and as many electronic devices and components become smaller, a large emphasis in the last few years has been placed toward electrically small antennas, including printed board designs such as UWB monopoles.

One of the main objectives of this study is the design of wideband, low profile and small antennas for microwave imaging applications. Our design approach was to select a printed monopole antenna that can meet most of our physical requirements and then design in the environment to meet our UWB features for microwave imaging applications. In order to meet the specification that the antenna be small, the proposed structure should be efficiently utilise the available space taking into account the fundamental limits on electrically small antenna.

In this chapter, we present two compact UWB monopoles using spline curves. By using spline curves a number of control points can be assigned to manipulate the shape of parametric curves, and as has been pointed out " the bandwidth of an antenna enclosed in a sphere of radius $r$ can be improved only if the antenna utilises efficiently, with its geometrical configuration, the available volume within the sphere " [5]. Furthermore, our choice of spline curve printed monopole is motivated by earlier study [6] that shows efficient surface area utilisation with good impedance match and wider bandwidth.

## 4.1 UWB Antenna Miniaturisation

To miniaturise any antenna, one has to consider the physical limitations imposed on electrically small antenna, thus an antenna whose electrical size or volume is defined by

$kr$ [5, 7], where $k$ is the free space wave number and equal to $\frac{2\pi}{\lambda}$ and $r$ is the radius of an imaginary sphere surrounding the maximum dimension of the antenna.

The fundamental limits of electrically small antennas were first studied by Chu [8] and followed by Harrington [9]. Chu used spherical wave function to describe the field distribution which propagates in the outward radial direction. The study by Chu [8], also confirmed that the source or current distribution of the antenna system inside the sphere is not uniquely determined by the field distribution outside the sphere. When the sphere which encloses the antenna element becomes very small, the quality factor Q becomes large.

From [10, 11], it has been shown that when $kr < 1$, the quality factor Q of small antenna can be expressed as [10]:

$$Q = \frac{1 + 2(kr)^2}{(kr)^3[1 + (kr)^2]}.e_{rad} \tag{4.1}$$

where $e_{rad}$ is the radiation efficiency of the antenna. Fractional bandwidth (FBW) is related to the Q of the system by:

$$FWB = \frac{\Delta f}{f_o} = \frac{1}{Q} \tag{4.2}$$

where $\Delta f$ = bandwidth and $f_o$= centre frequency.

It follows that by increasing the Q as in (4.1) has a direct consequence on the FBW of electrically small antenna as in (4.2). The opposite is also true, so to optimise the FBW of small antenna the size of the antenna and the quality factor must be taken into account.

UWB monopoles are known to operate in resonating mode at lower frequencies and travelling wave mode at higher frequencies. The smooth transition from resonating mode to travelling mode is achieved through overlapping of resonating harmonics and optimising feeding position and ground plane [12]. The two antennas designed in this chapter have been assessed for possible microwave imaging application. These antennas are very good candidates for such applications due to their UWB characteristics and very small size.

## 4.2 Coplanar Waveguide (CPW) UWB Antenna

Most UWB antennas that have been reported in the literature used canonical geometries [13, 14]. However, these antennas have limitations in utilising the available surface area. For small antennas, the physical limitations imposed on them [8] make it imperative to efficiently maximise the available surface area. Spline-based geometries have been implemented into planar antennas to provide UWB operations [6]. In this study, our approach is to use spline curves to design planar monopoles for UWB operations.

The proposed CPW UWB antenna was designed to operate in the lower frequency range of UWB spectrum. The geometry of the proposed CPW UWB antenna is shown in Fig.4.1. The geometry consists of 25 x 16 $mm^2$ FR4 substrate with $\varepsilon_r = 4.6$ and thickness 1.57 mm. On top of the substrate is the spear-shaped radiator modelled from spline curves where the optimised curve profiles $Z_A = 7.348$ mm and $Z_B = 9.284$ mm were designed according to the exponential taper equation (4.3) [15]:

$$z = Ae^{aL} \tag{4.3}$$

where $A = 0.5$, the scaling factor, $-4.5 \leq a \leq 2.5$, the exponential rate and $L = \pm 2$, the shifting value. It follows that the exponential rate:

$$a = \frac{1}{L} In(\frac{z}{A}) \tag{4.4}$$

The shape of the radiator is designed to maximise the surface area bearing in mind the limitations imposed on small antennas. The design also controls the surface wave currents that normally affect the antenna performance as the surface wave on the radiator decay exponentially and travel within the substrate at a relatively short distance and begin to radiate because of the discontinuity between the two media. On the same side of the radiator is coplanar waveguide (CPW) where all the conductors lie on the same plane . The optimised dimensions were obtained after several iterations as have been shown in Fig. 4.1.

### 4.2.1 Parametric Studies of Coplanar UWB Antennna

The simulation results show that the antenna performance is dependent on two parameters. We studied the combinations of the structure parameters which include; ground plane length *gl* and the *bend* at the corners of the ground plane (Refer to Fig. 4.1).

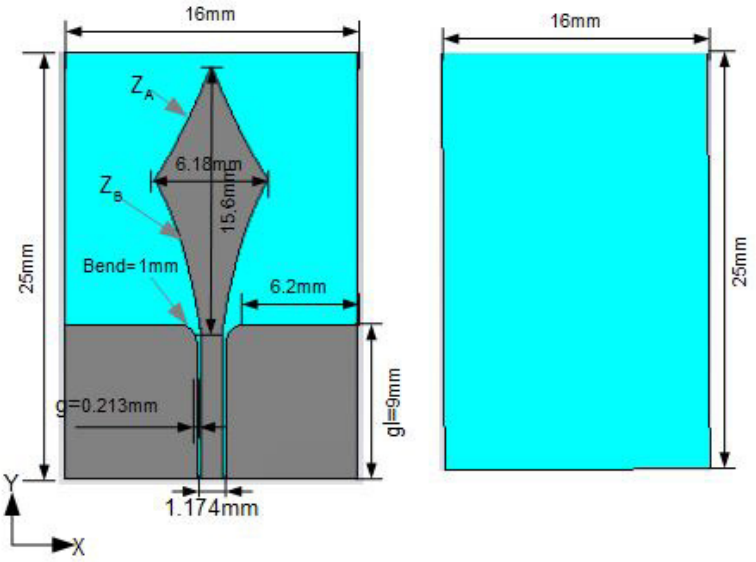


FIGURE 4.1: Geometry of the optimal Coplanar UWB antenna: left (top view), right (bottom view)

(i) Effect of ground length $gl$

Fig. 4.2 depicts the simulated return loss curves for different values of $gl$ with optimal values of other parameters fixed at $g$= 0.2 mm, $bend$ = 1 mm.

It can be seen in Fig. 4.2 that the resonant frequencies shift slightly upwards with the increase of the ground length $gl$. The return loss also increases with similar pattern, however, the antenna is better matched at $gl$ = 9 mm. The antenna is very sensitive with respects to the changing of $gl$, for example at $gl$ = 10 mm, the return loss was just below -10dB but the matching was different from the optimal value $gl$ = 9 mm.

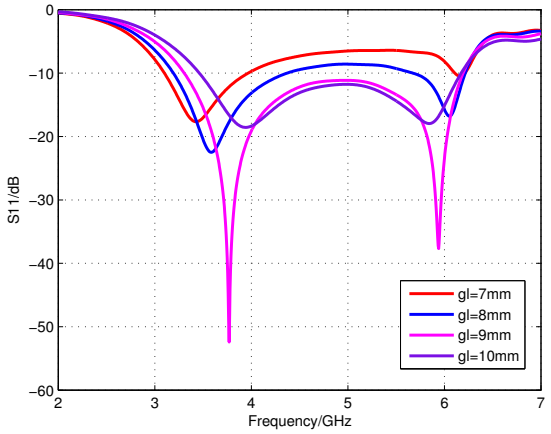


FIGURE 4.2: Simulated return loss curves of the effect of design parameter $gl$ on CPW UWB antenna with optimal values; $g$ = 0.2 mm, $bend$ = 1 mm

(ii) Effect of cpw *bend*

The corners of the cpw ground plane close to the central conductor were bent to enhance the input impedance and matching. The effect of the *bend* on the antenna with other optimal parameters fixed at $g = 0.2$ mm, $gl = 9$ mm is shown in Fig.4.3.

It can be seen from Fig. 4.3 that between the values *bend* = 1 mm - 2.67 mm better matching and input impedance results were achieved. The return loss began to deteriorate when the curve was bent at 3.5 mm. The *bend* has little effect on the resonant frequency, but it affects the impedance matching when it increases especially from 3.5 mm onwards.

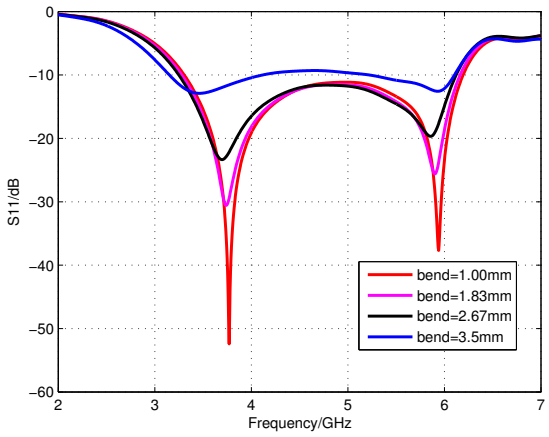


FIGURE 4.3: Simulated return loss curves of the effect of design parameter *bend* on CPW UWB antenna with optimal values, $g = 0.213$ mm, $gl = 9$ mm

### 4.2.2 Results of CPW UWB antenna

Fig. 4.4 shows the prototype of the proposed CPW UWB antenna. We evaluated the performance of the antenna in free space with optimal parameters shown in Fig. 4.5. The results in Fig. 4.5 show that the antenna operate in the lower UWB spectrum from 3.30GHz- 6.20GHz at -10dB with deep resonance at 3.77GHz and 5.94GHz. There is good agreement between the simulated and measured results.

The antenna also provides excellent impedance, radiation patterns and gain within the spectrum. The radiation patterns in azimuthal plane and elevation plane were evaluated in free space at the following frequencies 3.5 GHz, 4.5 GHz and 6GHz. Fig. 4.6(a) shows that in the azimuthal plane, the lower frequencies exhibit omnidirectional pattern, however, at higher frequencies (e.g 6 GHz) the pattern is directive. In the elevation plane, Fig. 4.6(b), the lower frequencies show dipole-like pattern (doughnut shape) with the nulls at 90° and 270°, the higher frequencies show quasi-omnidirectional pattern.

FIGURE 4.4: Prototype of CPW UWB Antenna (left) top view, and (right) bottom view.

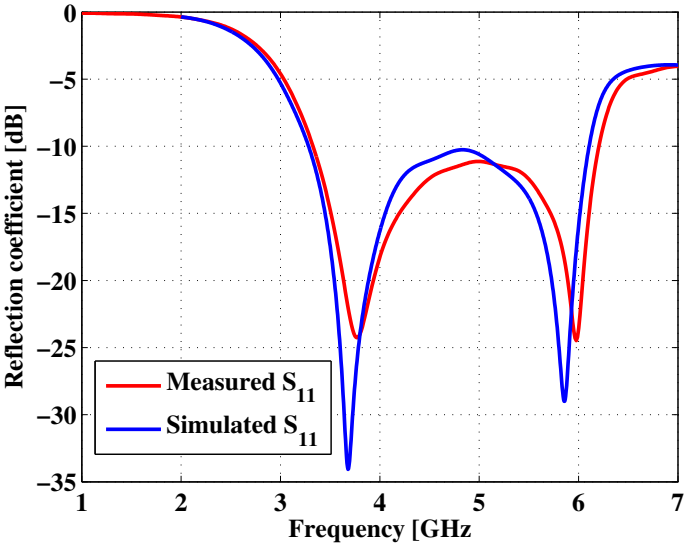


FIGURE 4.5: Simulated and Measured $S_{11}$ of CPW UWB antenna .

The realised gain is between 1.85dB to 4.8dB from 3.3-6.2 GHz and the efficiency ranges from 63% to 98% within the interested range as shown in (See Fig.4.7 (a) and (b)) respectively. The VSWR $< 2$ within the operational bandwidth.

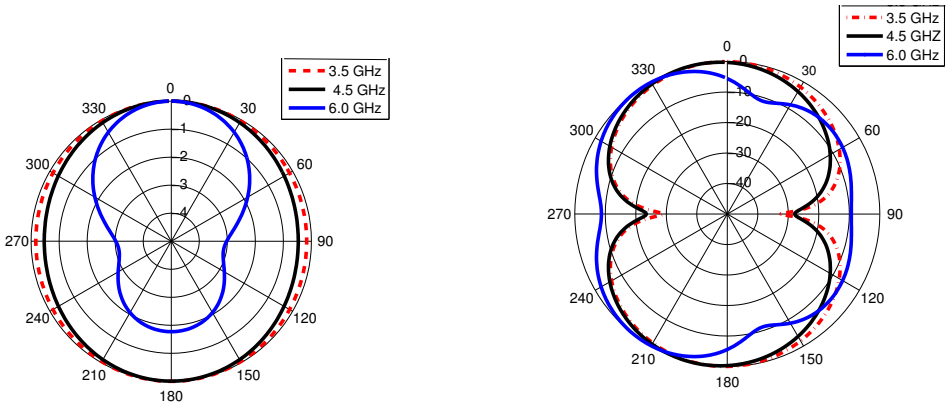


(a) (b)

FIGURE 4.6: Free space radiation pattern of CPW UWB antenna at 3.5 GHz, 4.5 GHz and 6 GHz (a) azimuthal plane, (b) elevation plane.

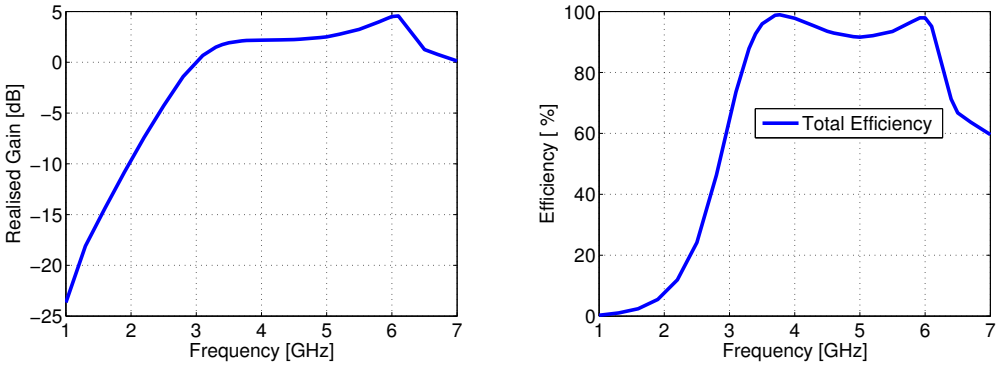


(a) Realised gain of CPW UWB antenna

(b) Efficiency of CPW UWB antenna

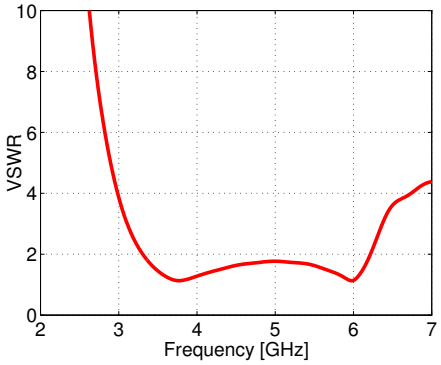


(c) Voltage standing wave ratio of CPW UWB antenna

FIGURE 4.7: Simulated Parameters (a) Realised gain (b) Efficiency ( c) VSWR of CPW UWB antenna

### 4.2.3 CPW UWB Antenna Performance in Coupling Medium

As the proposed antenna is intended for microwave imaging, we studied the response of the CPW UWB antenna in coupling medium usually used to reduce the adverse effects of signal reflections at the antenna-air-breast interface. Previous studies reported in the literature show that without coupling medium most of the signal source would be reflected at the air-skin interface [16, 17]. In this study, a coupling medium which is a mixture of 90% glycerin and 10% water was chosen. An array of four antenna elements were fully immersed in a cylindrical tank (measuring 8 cm in radius and 15 cm in height) containing the coupling liquid as shown in Fig. 4.8. The distance between the antenna elements were set at 14 cm which is similar to the spacing expected in a clinical system.

First we evaluate the signal strength between the antennas in the coupling medium with the results shown in Fig. 4.9. The results show that there is minimal coupling of -30 dB between the antennas. We also had to evaluate the signals transmitted from transmitter (Tx) to the receivers (Rx) by varying the relative positions between the antennas with respect to the height of the container. We record the signals strengths at each of the locations of the receivers between the frequency spectrum 1.5 GHz to 4.0 GHz. We processed the results as a function of signal strengths to the relative positions of the receivers as shown in Fig. 4.10.

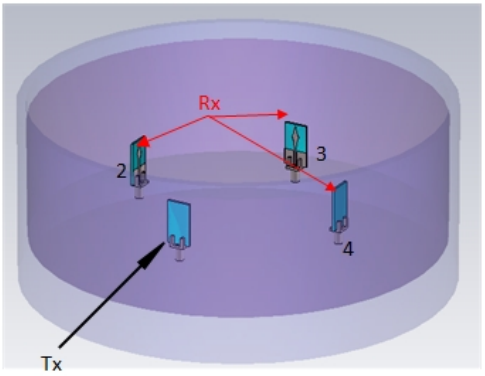


FIGURE 4.8: Simulation setup for CPW UWB antenna fully immersed in a coupling liquid made up of 90% glycerin and 10% water. The distance between the antenna elements was set at 14 cm.

The signals received by all the receivers (Rx 2, Rx 3, Rx 4) at the following frequencies 3.5 GHz to 4.0 GHz were very low, however, it is also important to emphasise that the low signal levels are mainly due to the choice of a very lossy coupling medium (glycerin/water), which is motivated by the need to minimise multi-path signals in microwave tomography. For radar-based systems, low-loss liquids are used and therefore the proposed antennas would produce much higher signal levels. At this stage no imaging algorithm has been used to processed the outcome, as the focus of this study is to propose

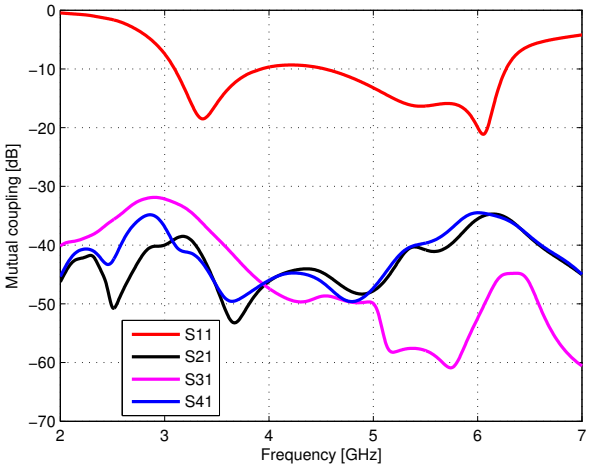


FIGURE 4.9: Mutual coupling of CPW UWB array

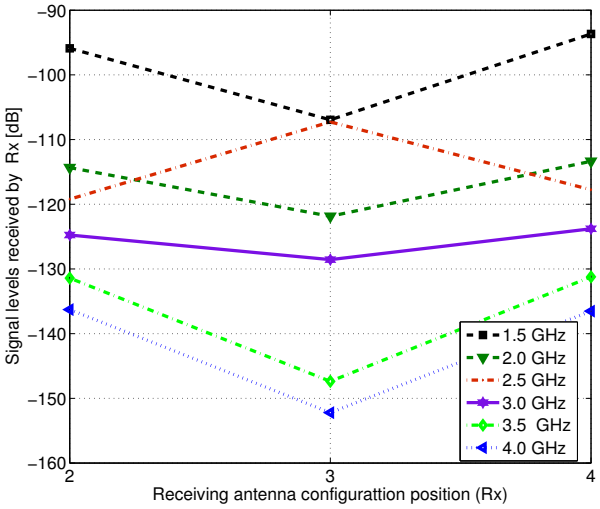


FIGURE 4.10: Signal strengths from Tx to Rx. The positions of the antennas were adjusted relative to the height of the container

small and conformal antenna for microwave imaging. However, the results presented in this study could serve as a basis for using this antenna for future microwave imaging with appropriate imaging algorithms.

### 4.2.4 Measurement Set-up for CPW UWB Antenna Imaging Array

It is necessary to perform some measurements to verify the experimental model. To do so we performed a simple test using four CPW UWB antenna array. The set-up is a plexiglass of approximately (14 cm x 14 cm x 15 cm) with properties closed to those used in the simulation. The plexiglass contains the matching liquid made up of 90%

glycerol and 10% water (See Fig. 4.11)[1]. Although we acknowledge the fact that it is practically impossible to eliminate interference from the environment, we covered the set-up with absorbers to minimise the effect. We mounted the antennas on the glass with configuration such that the positions of each antenna is 90° to the adjacent antenna while those opposite were 180°.. The transmitter transmits the signals while the rest of the antennas remain in the receiving mode. We look at the scattered signals detected by the receiving antennas in the array as a results of introduction of the cylindrical scatterers (3 mm in radius and height 3cm).

In this study we looked at the sensitivity towards the locations of randomly placed tumors (in this case the scatterers). We tested the CPW antenna array with scatterers at different locations with the antennas being kept at high or low locations in line with base of the immersion. The frequency of operation is determined to be 3-4 GHz in this study. The dynamic range in this case was assumed to be -70dB and set to the average received signal at 3 GHz.

The measured scattering parameters have been shown in Fig. 4.12. As has been observed the average scattered signal from the transmitter to all the receiving antennas is around -40 dB across the frequency range 2 GHz - 4 GHz, which shows the sensitivity of the imaging system to the small objects (scatterers). It shows that the set-up can detect the presence of the 6mm scatterer.

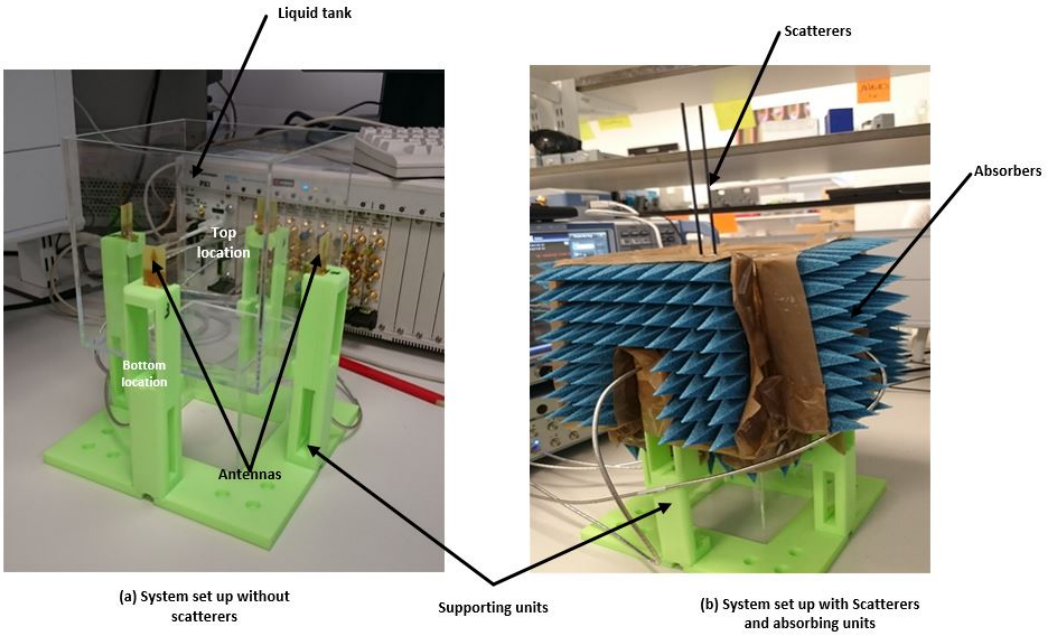


FIGURE 4.11: CPW UWB imaging measurement set-up. (a) Set-up without scatterers and absorbing units, (b) Set-up with scatterers and absorbing units. The distance between the antenna elements was 14 cm. The antennas were placed at different positions labelled as top and bottom in the figure.

[1]Kind Courtesy of MediWise UK Ltd

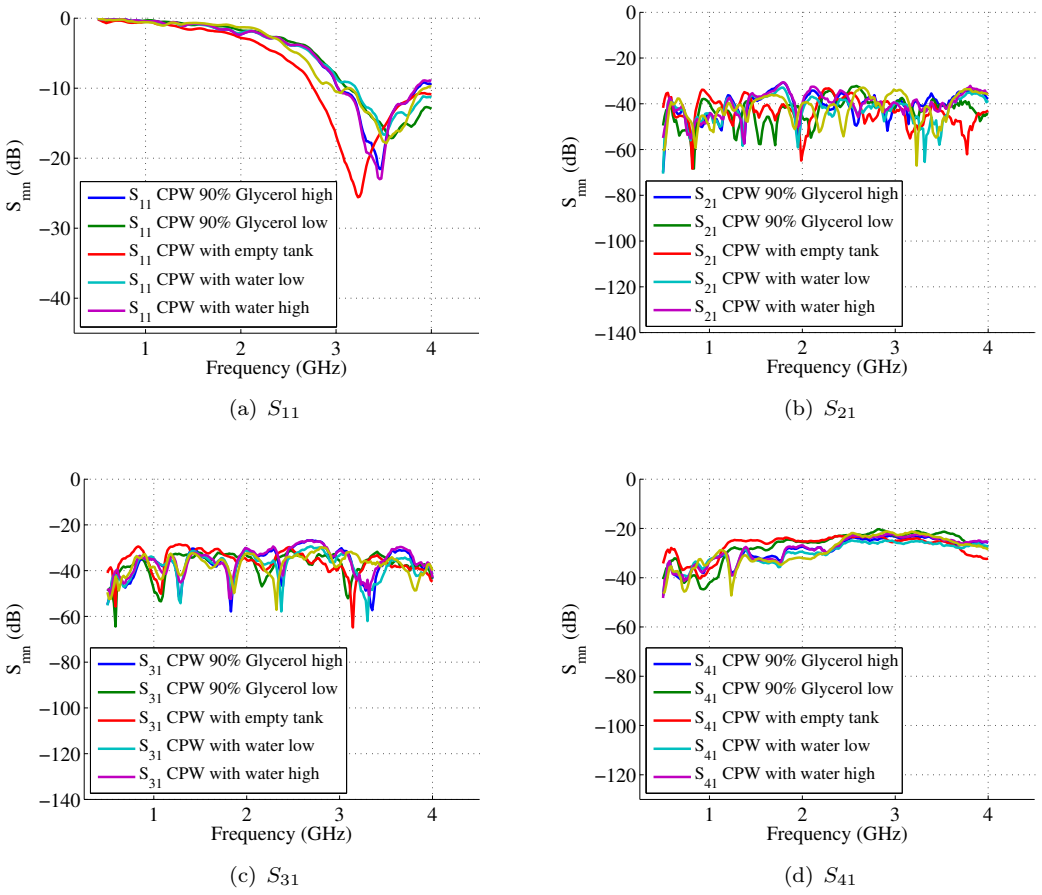


(a) $S_{11}$ (b) $S_{21}$

(c) $S_{31}$ (d) $S_{41}$

FIGURE 4.12: Measured scattering parameters of CPW UWB Antenna array. The concentration of the matching liquid used, 90% glycerine and 10% water.

## 4.3 Planar UWB Antenna for Microwave Imaging

### 4.3.1 Antenna Geometry

In addition to the CPW UWB antenna we propose another printed UWB monopole antenna with a different ground plane. The distinction between the two antennas is the spectra of operation and positions of the ground planes. By adding more resonances to the new design we enhanced the bandwidth, thereby, covering the whole spectrum as defined by FCC (3.1-10.6 GHz) while the CPW UWB only covers the lower band (3.1-6 GHz), hence we adopt the new design procedure.

The geometry of the proposed Planar UWB antenna consists of a 16 x 25 mm$^2$ FR4 substrate with $\varepsilon_r = 4.6$ and thickness 1.57 mm. On top of the substrate is a spear-shaped radiator with the profile curves $A$ and $B$ modelled using the exponential equation (4.5):

$$y = e^x + t \tag{4.5}$$

where $-4 \leq x \leq 2.4$ and $t = \pm 2$ which is a constant to shift the curve from the vertical axis. At the back of the substrate is a semi-circular cut (radius c, refer to Fig. 4.13) ground plane with a small triangular notch in parallel with the feed line to improve the impedance matching. In [18],[19] Guo *et al.* have used similar ground plane for UWB antennas. This type of ground plane as demonstrated in the literature shows that wideband operation could be achieved. Furthermore, the structure of the ground plane reduces unwanted surface current waves that have the potential of propagating along the transmission and receiving lines. A 50 Ω coaxial transmission line was used to feed the antenna.

#### 4.3.1.1 Design Steps and Guidelines

The first process was to design the ground plane from a rectangular shape, then introduced the semi-circular slot with its radius $c$ already defined in Table 4.1. The open ends of the rectangular shape is cut off to the appropriate dimension. The substrate with dimensions L x W was constructed on top of the ground plane. The radiator was designed according to the exponential equation (4.5).

The curve $A$ (See Fig. 4.13) was constructed first using the analytical curve facility within CST Microwave Studio [20]. Curve $A$ was transformed using the Transform menu and Mirror submenu within CST to get curve $B$. Both curves were finally mirrored to get the other half of the radiator to form a closed structure . The antenna geometry and the parameters were optimised to improve its performance. The optimal dimensions of the antenna are shown in Table 4.1.

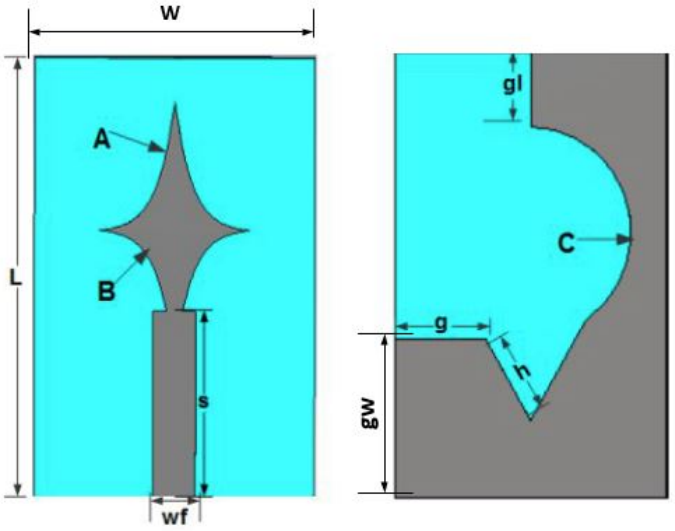


FIGURE 4.13: Geometry of Planar UWB antenna: left (top view), right (bottom view)

TABLE 4.1: Optimal dimensions of Planar UWB antenna

| Parameter | L | W | A | B | C | s | wf | g | gw | gl | h |
|---|---|---|---|---|---|---|---|---|---|---|---|
| Unit (mm) | 25 | 16 | 9.3 | 6.5 | 5.9 | 10.6 | 2.4 | 5.4 | 8.0 | 4.2 | 5.9 |

### 4.3.2 Results of Planar UWB Antenna

The prototype of the proposed Planar UWB antenna is shown in Fig. 4.14. The antenna was characterised by a Keysight M9375A vector network analyser (VNA). Fig. 4.15 shows the results for simulated and measured return loss. The results show that the proposed structure covers the entire spectrum allocated by FCC for UWB application. The -10 dB bandwidth shows that the antenna operates from 2.7-10.7 GHz representing a fractional bandwidth (FWB) of 119%, which is enough to satisfies the FCC requirements. It also establishes the fact that high FWB leads to high processing gain, good multi-path resolution and low signal fading.

We also examined the radiation patterns at the following frequency points; 3.1 GHZ, 6.5 GHz and 10 GHz. Fig. 4.16 shows that the proposed Planar UWB antenna maintains a very good radiation patterns at the selected frequencies. In the azimuth plane, the antenna shows a stable radiation pattern by maintaining the main beams in the broadside direction. In the elevation, it can be seen that the proposed antenna displays stable omnidirectional radiation patterns at all the sampled frequencies.

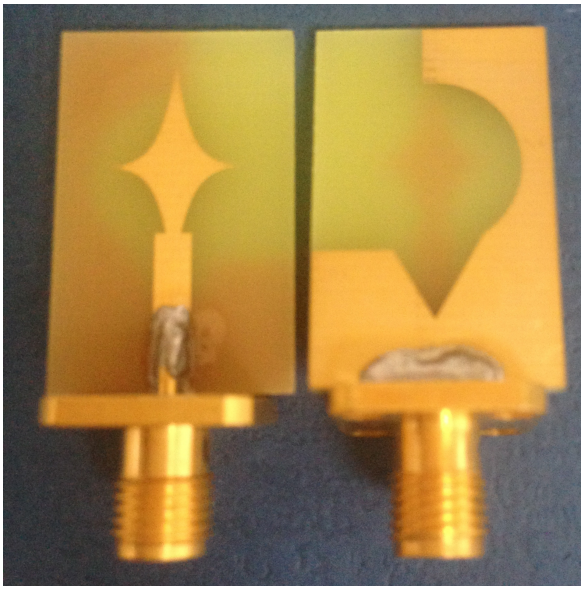

FIGURE 4.14: Prototype of the proposed Planar UWB Antenna

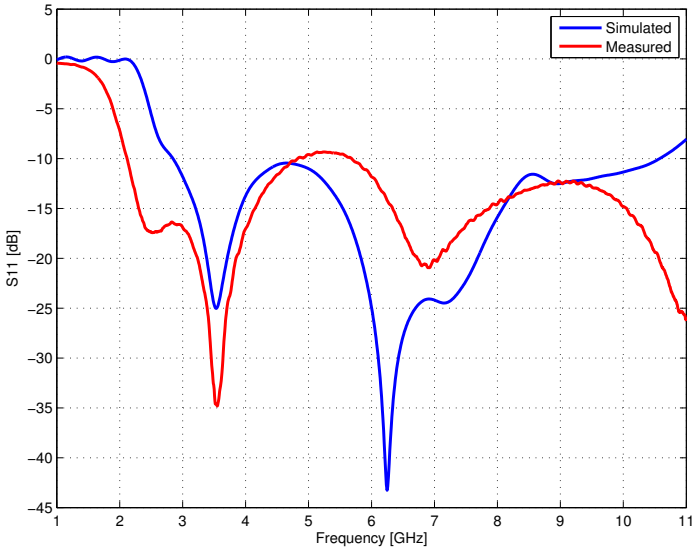


FIGURE 4.15: Simulated and measured return loss curves of Planar UWB antenna

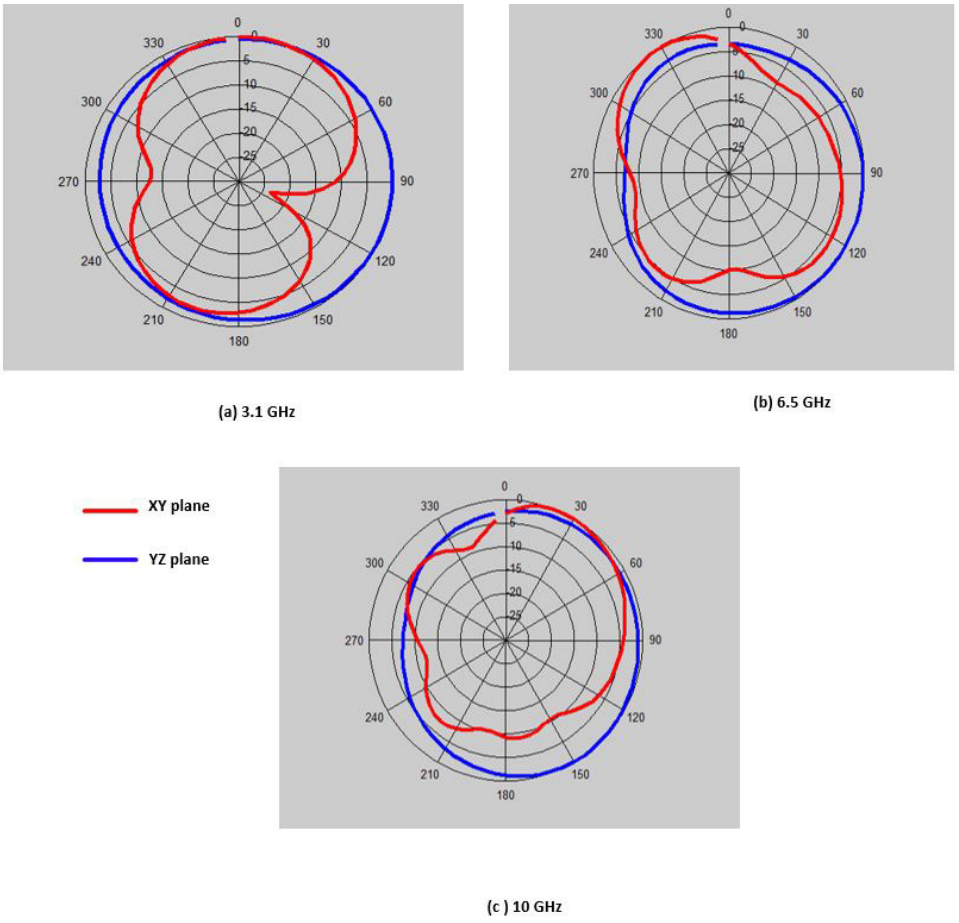


FIGURE 4.16: Radiation patterns of the proposed Planar UWB antenna at 3.1, 6.5 and 10 GHz.

The gain values range approximately from 2.1 dBi to 5.3 dBi in the spectrum 2.7 GHz-8.1 GHz, however, from 8.3 GHz to 11.4 GHz the gain values decrease slightly (Fig. 4.17).

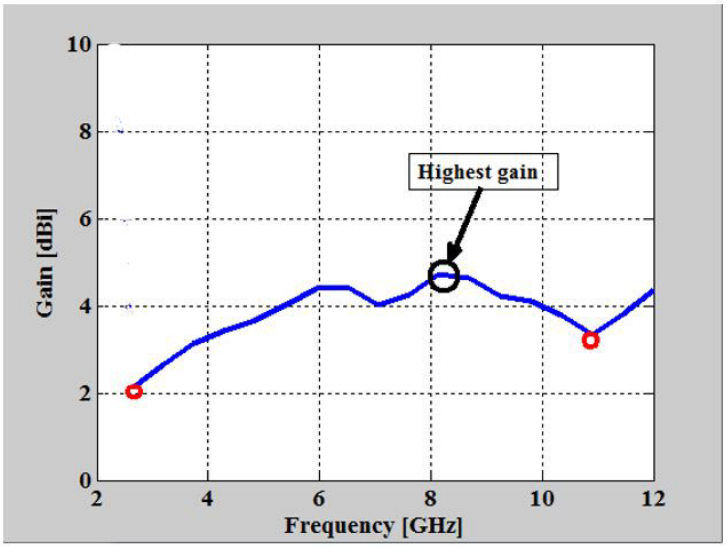


FIGURE 4.17: Simulated total gain of the proposed Planar UWB antenna.

### 4.3.3 Simulation Studies to Assess Feasibility of Imaging with the Planar UWB Antenna

In this study an array of four planar UWB antennas in a circular loop was considered. The aim is to observe and study the effects of inclusion of immersion medium and biological phantom. The focus of our study will still remain on the backscattered and received signal strength of the receivers, which will ultimately define and shape up the images with appropriate imaging algorithm.

In Fig. 4.18, the transmitter (Tx) was excited and all the remaining three antennas ($R_2, R_3, R_4$) were in receiving mode. The received power at each receiver is a function of its distance from the transmitter, hence the antenna furthest away from the transmitter should receive the minimum power. The study is carried out in two different cases. In case 1, the antennas were placed inside a plastic cover and were fully immersed in the matching liquid. For convenience and better visibility the immersion medium has not been shown for the case where antenna elements were fully immersed in the medium (Fig. 4.18(a)). In case 2, the antennas were placed outside the plastic cover operating in the free space as shown in Fig. 4.18(b).

The plastic cover is made up of 3D printing material and its permittivity and conductivity given as 3 and 0.0015 S/m respectively. The skin layer selected from the CST material library models the first layer of the biological phantom under study. The remaining

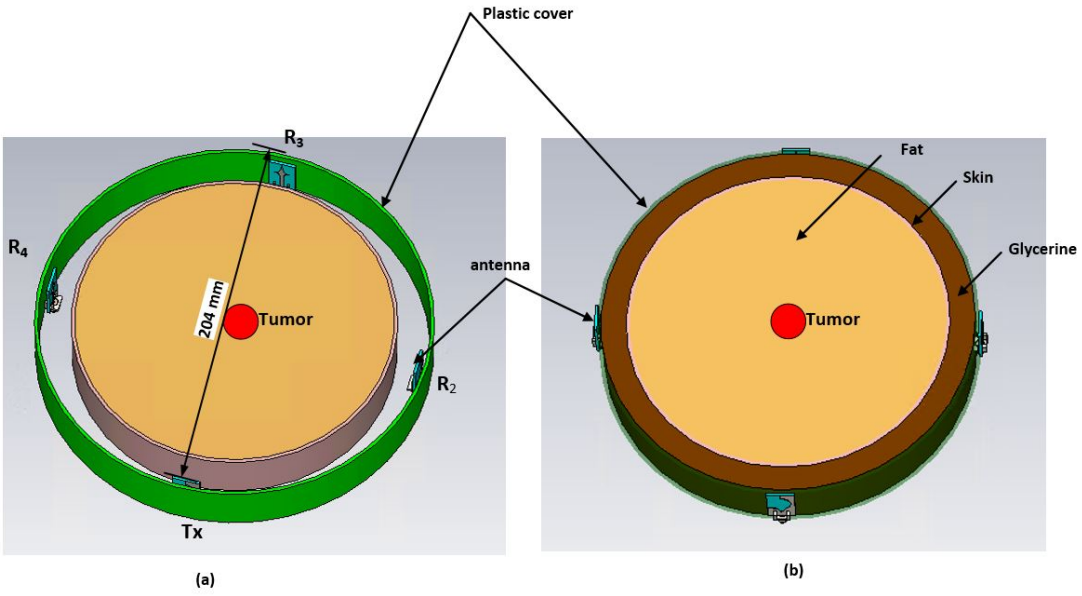


FIGURE 4.18: Imaging array using Planar UWB antenna (a) antennas fully immersed in the liquid medium (b) antennas mounted on the plastic cover.

volume of the phantom is assumed to be homogeneous fat, again, selected from the CST material library. The immersion medium is a mixture of 90% glycerine and 10% water.

The diameter of the array is 204 mm in both cases. In the scenario where antennas were fully immersed in a medium, the external diameter of the plastic cover is 220 mm with thickness 2 mm, the immersion medium is placed in the entire volume inside the cover and then the biological phantom is inserted inside the coupling medium. The skin is considered to be 2mm thick with an external diameter of 186 mm and the homogeneous fat occupies the remaining volume of diameter 184 mm. The target tissue or tumor is a cylindrical shape with radius 3 mm and height 7.7 mm which was modelled using a Debye model with $\varepsilon_\infty = 3.99$, $\varepsilon_s = 54$, relaxation time 7e$-^{12}$, and placed at the centre of the fatty tissue i.e 104 mm from the transmitter Tx. The height of the array is 32.5 mm where the port is 7.5 mm high from the bottom of the immersion.

In the second scenario, depicted in Fig. 4.18(b), the antenna elements were placed outside the immersion. They are stuck on the exterior of the plastic cover, rest of the geometry is the same as scenario one. The immersion liquid is not in contact with the antennas and is serving as a coupling medium only. All antenna elements have been assigned their own respective ports and only antenna Tx with port number 1 is excited, the remaining elements only receive the scattered signals.

#### 4.3.3.1 Case 1: Planar UWB Antenna Array Coupling Medium

We will look at the frequency and time-domain properties of the antenna in coupling medium.

(I) Frequency-Domain Response Using Fig. 4.18(a) set-up

Fig. 4.19 shows the transmission coefficients ($S_{21}$) between the transmitter and the receivers. First, it is observed that the free space transmission has higher transmission amplitude. The models with phantom, however, exhibit relatively weak transmissions because of the presence of biological tissues. Nevertheless, at certain frequencies, for example (3.4 GHz, 4.5 GHz) the receivers picked up good signals around -60 dB which is good enough for modern microwave circuitry systems. Similar signal behaviour has been observed by the transmission from $R_2$ and $R_4$, which is not a surprise since both receivers were at the same distance of 40 mm from the transmitter.

(II) Reflected Signals of Planar UWB Antenna with Fig. 4.18(a) set-up

The transmitter Tx was excited by Gaussian pulse shown in Fig. 4.20 . We examine the reflected signals in free space without the phantom and compare the results with the cases where we have phantoms. We studied the signal behaviour by placing virtual probe at the point of interest.

As has been shown in Fig 4.21 the reflected signals in free space and the model with phantoms show clear differences in terms of signal amplitudes. The models with phantoms have lower amplitude as a result of the biological tissues. In the case of phantom without tumor and phantom with tumor, looking at the time between 2 nanoseconds and 3 nanoseconds (Refer to Fig 4.21(b) and (c)), the signal amplitudes circled in black differ as the result of the tumor. The early-time content of the signals is influenced by the presence of the tumor. Since the phantom model without tumor has higher amplitude than the one with tumor response, the early-time signal could be processed earlier without corrupting the tumor signals. The difference in signal amplitudes could be processed with appropriate image algorithms.

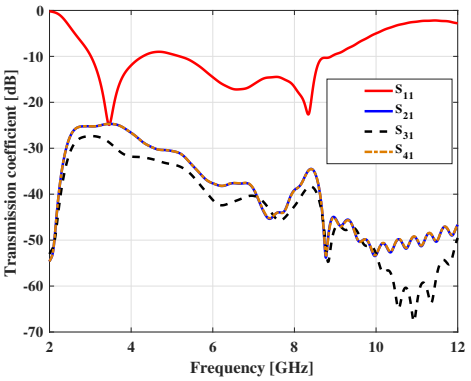


(a) $S_{21}$ in free space

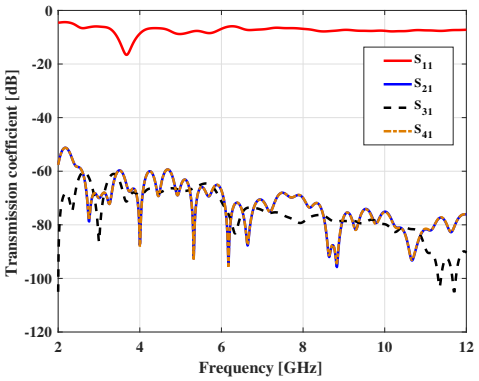


(b) $S_{21}$ of phantom without tumor

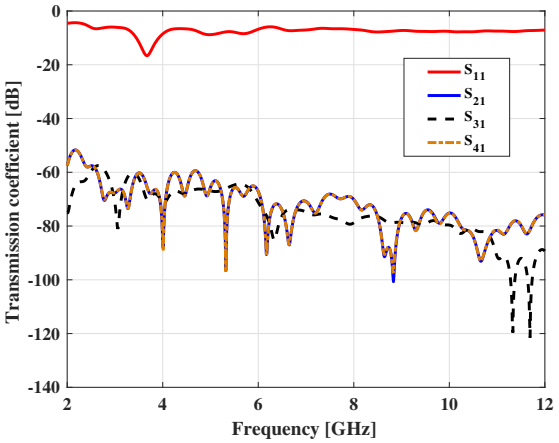


(c) $S_{21}$ of phantom with tumor

FIGURE 4.19: Comparison of transmission coefficients ($S_{21}$) of an array of Planar UWB antenna. The figure depicts the transmission when the antennas were immersed in a liquid medium

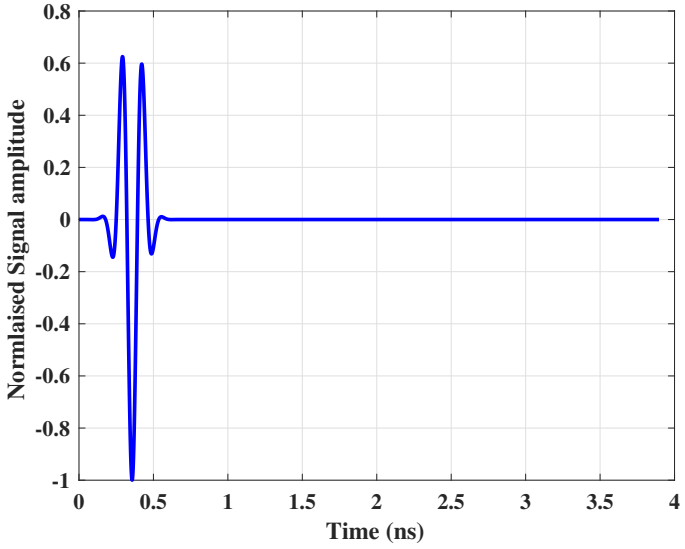


FIGURE 4.20: Gaussian pulse used to excite Planar UWB antenna

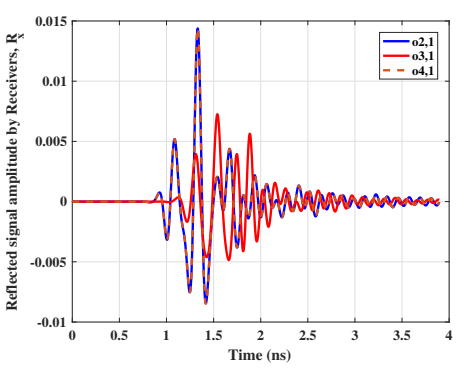


(a) Reflected signals in free space

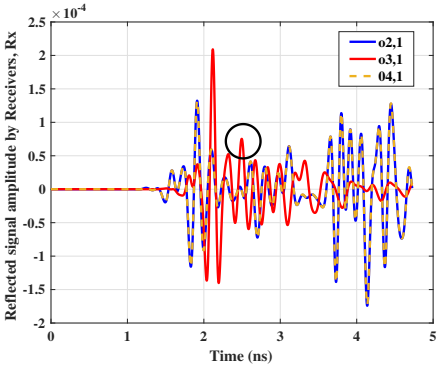


(b) Reflected signals with phantom without tumor

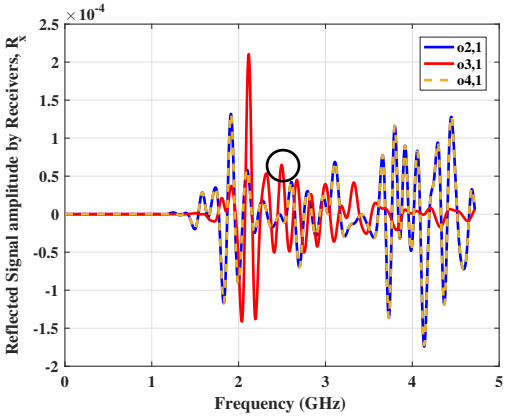


(c) Reflected signals with phantom and tumor

FIGURE 4.21: Comparison of reflected time-domain signals of Planar UWB antenna. The results show the case where the antennas were immersed in a liquid medium

(III) Transmitted Signals of Planar UWB antenna with Fig 4.18(a) set-up

We also examine the signals received at some strategic locations. We placed probes at 40 mm, 102 mm and 204 from the transmitter Tx to measure the field strengths. Most importantly, we observe changes in signal amplitudes at 102 mm, the location where the tumor was placed. The recorded signal strengths at these locations have been shown in Fig. 4.22. It can be seen from the figure that, the free space signals reached the maximum amplitude within few nanoseconds. However, the models with phantoms reached maximum amplitudes with some delays.

We examined carefully the signals recorded at 102 mm from the transmitter. At this particular point where the tumor was placed, it became apparent that the phantom without tumor has unchanged signal amplitude between 1.5 nanoseconds to 2 nanoseconds (See Fig. 4.22(b)). On the other hand, within the same time frame, the model with tumor shows change in signal amplitude. The reflection from the tumor influenced the changes in signal amplitude.

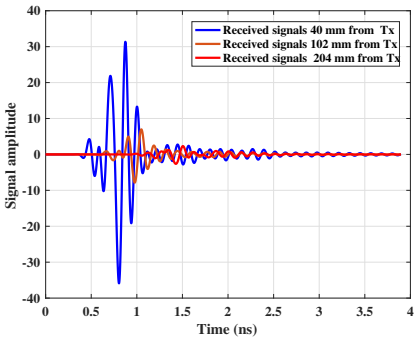


(a) Received signals in free space

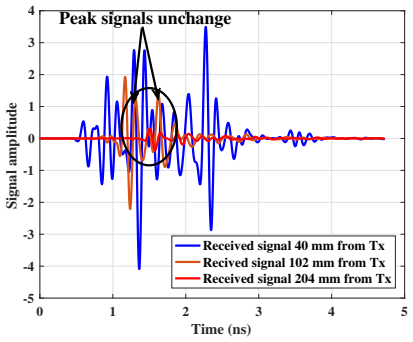


(b) Received signals with phantom without tumor

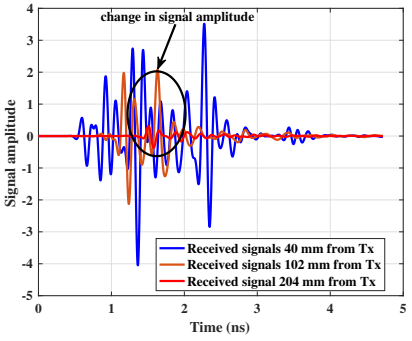


(c) Received signals with phantom and tumor

FIGURE 4.22: Comparison of received time-domain signals where the antennas were immersed in a liquid medium. Probe was used to record the signals at 40 mm, 102 mm and 204 mm from Tx

#### 4.3.3.2 Case 2: Planar UWB Antenna Array Mounted on the Plastic Cover

We investigate the case where the antennas were mounted outside a plastic cover as shown in Fig. 4.18(b)).

(A) Frequency-Domain Response of Planar UWB antenna Using Fig. 4.18(b) set-up

Fig. 4.23 shows the transmission coefficient from the transmitter Tx to the receivers Rx. It can be seen that the signal transmission is very weak from Tx to Rx due to the fact that most of the signals were scattered by the plastic material and the biological tissues. $R_3$ which is 204 mm from the Tx exhibits very weak signal across the whole spectrum. If we compare the two cases i.e antenna in coupling medium and outside coupling medium, the results suggest that the proposed Planar UWB antenna could be preferably used for microwave imaging applications by immersing the antenna elements in a coupling medium.

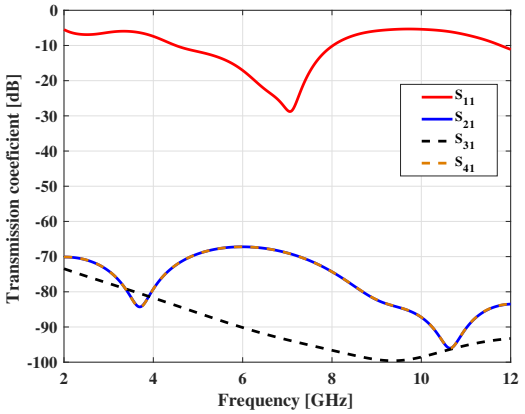


FIGURE 4.23: Transmission coefficient when an array of four Planar UWB antenna were mounted outside plastic cover as shown in Fig. 4.18(b)

(B) Scattered Signals of Planar UWB antenna with Fig 4.18(b) set-up

When an array of four Planar UWB were mounted outside plastic cover (Refer to Fig. 4.18(b)), we studied the scattering effect at the walls of the imaging tank. Fig.4.24 shows the scattering signals which shows that most of the signals could not go through the plastic cover and the phantom. Other studies [21, 22] have suggested that antennas for microwave imaging should be immersed in a coupling medium, which has been the case in our first scenario, to minimise the mismatch between the coupling medium and free space.

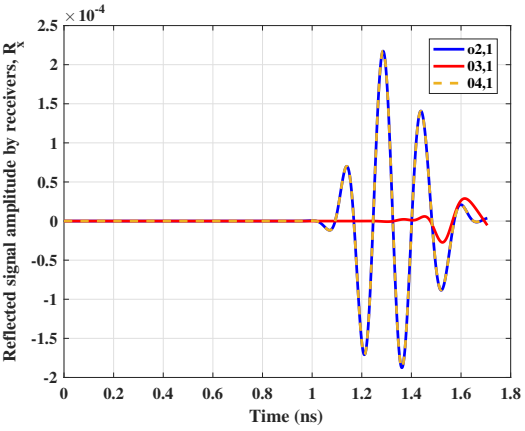


FIGURE 4.24: Scattered signal when an array of four Planar UWB antenna were mounted outside plastic cover as shown in Fig. 4.18(b)

(C) Transmitted Signals of Planar UWB antenna with Fig 4.18(b) set-up

Fig. 4.25 shows the received signals when an array of four Planar UWB antennas were mounted outside the plastic cover as shown in Fig. 4.18(b). We used virtual probe to measure the signal strengths at a distance 204 mm from the transmitter (Tx). The signal amplitude is almost flat suggesting that the plastic cover and

the biological tissues between $T_x$ and $R_3$ scatter most of the signals. Although we detected some signals at 40 mm and 102 mm from the Tx, the the signal strengths were weak as compared to what were detected at the same locations when the antennas were immersed in coupling medium. This indicates that for imaging applications the proposed antenna could be best used by deploying them in immersion medium.

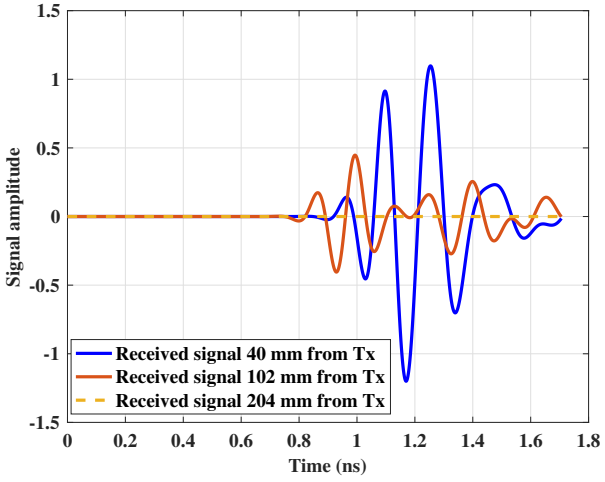


FIGURE 4.25: Received signal strengths when an array of four Planar UWB antenna were mounted outside plastic cover as shown in Fig. 4.18(b)

### 4.3.4 Measurement Set-up of Planar UWB Antenna Imaging array

To study the behaviour of the proposed antenna for microwave imaging application, we examine the signal properties through the coupling medium (90% glycerine and 10% water). In all cases, $S_{21}$ transmission parameter was first measured with no scattering objects present between the antennas. We measured $S_{21}$ again with cylindrical scatterers (3 mm in radius and height 3 cm) placed between the antennas. We compare the results in the coupling medium to the free space measurements. The reflection and transmission coefficients of the antennas were obtained by placing the antennas in the tank containing the coupling liquid (i.e 90% glycerine and 10%) and measuring S-parameters with vector network analyser.

In the measurements we used the same set up in Fig. 4.11. We carried out the measurement by placing the antennas in three different positions around the plexiglass containing the coupling medium with the scattering objects . We measured the s-parameters in free space array. We positioned the antennas on the top part of the tank making sure that the antennas were at same level as the coupling medium. We measured the reflected and transmission coefficients at this position. We also placed the antennas close to the

bottom of the tank and measured the S-parameters. We chose these kind of measurements to observe the consistency in signal behaviour of the antenna. Fig. 4.26 shows the measured reflection and transmission characteristics of the antenna.

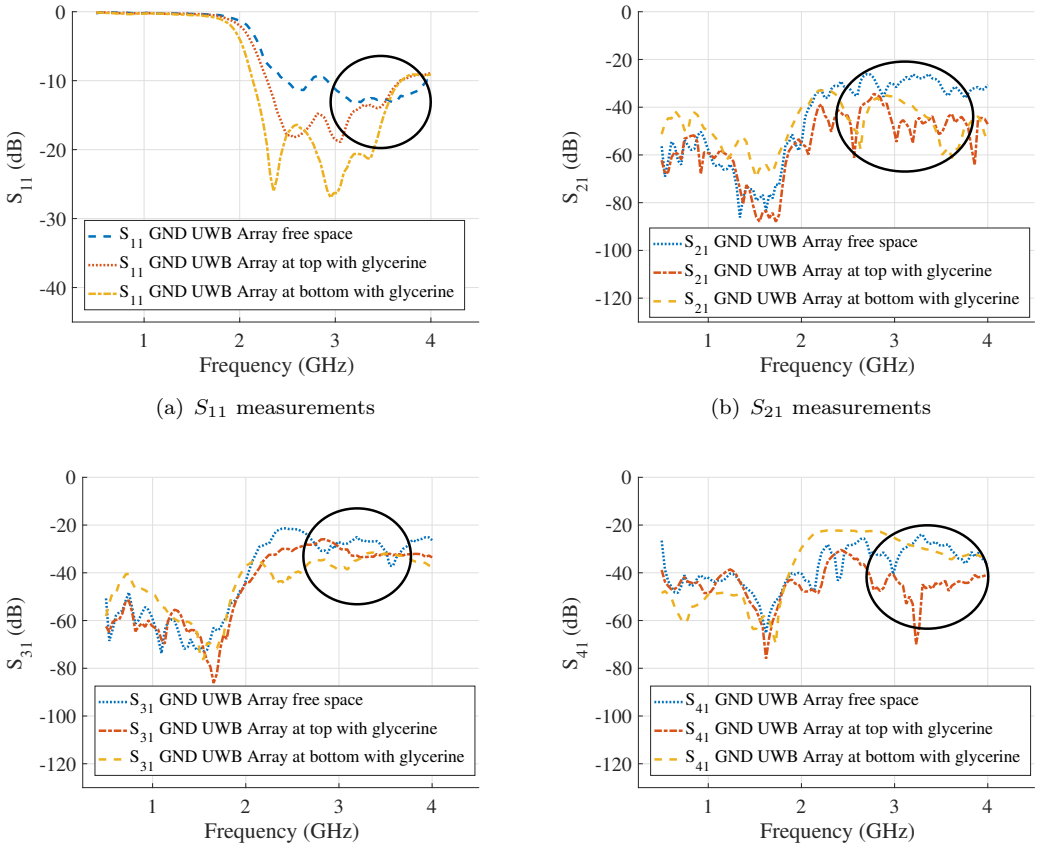


(a) $S_{11}$ measurements

(b) $S_{21}$ measurements

(c) $S_{31}$measurements

(d) $S_{41}$ measurements

FIGURE 4.26: Measured S-parameters of the proposed Planar UWB antenna. Four antennas in an array were placed on a tank containing coupling medium (i.e 90% glycerine and 10%)

TABLE 4.2: S-parameters of Planar UWB antenna at 3.0 GHz, 3.5 GHz and 4.0 GHz. The antennas were placed at different positions on the tank containing the coupling liquid

| Frequency (GHz) | $S_{11}$(dB) | | | $S_{21}$(dB) | | | $S_{31}$(dB) | | | $S_{41}$(dB) | | |
|---|---|---|---|---|---|---|---|---|---|---|---|---|
| | Free | Top | Bottom | F ree | T op | Bottom | F ree | Top | Bottom | Free | T op | Bottom |
| 3.0 | -12.5 | 18.7 | 26.3 | -37.5 | -39.6 | -56.7 | -29.5 | -29.9 | -38.2 | -22.1 | -40.0 | -40.0 |
| 3.5 | -15.7 | 14.8 | 22.7 | 28.5 | -45.5 | -45.7 | -25.6 | -27.8 | -27.8 | -24.5 | -27.3 | -43.1 |
| 4.0 | -11.2 | 10.1 | 10.0 | -38.2 | -46.2 | -47.5 | -24.7 | -36.1 | -38.1 | -35.4 | -40.9 | -35.9 |

Detailed analysis of the antenna in free space shows that the antenna radiates very well from 3 GHz onwards. We analyse the scattering signals between 3 GHZ- 4GHz shown in black circle in Fig. 4.26. The results show that there is signal attenuation through target tissue ( in this case scatterers). In comparison to results of the CPW antenna,

the signal levels between 3 GHZ- 4GHz are still within practical detectable range if we assume a system with a dynamic range of -70dB. Moreover, as has been summarised in Table 4.2, the scattered field values show the sensitivity of the imaging system in the presence of scattering objects measuring about 3 mm in radius.

## 4.4 Summary

This chapter presents two novel printed monopoles designed for microwave imaging. The printed monopoles in this study are compact with physical size of 16 mm x 25 mm and $0.24\lambda$ in electrical size and comparable to similar designs reported in the open literature [23–25]. The proposed UWB monopoles are small enough to fit within the relatively small array area,thereby enhancing microwave image resolution and quality. The study also shows the possibility of using spline curve printed monopoles to model small antennas for microwave imaging application. The two printed monopoles provided different performances in terms of frequency of operation. The CPW monopole antenna where both radiator and ground elements are printed on the same side only covers the lower UWB band (3.1-6 GHz). Using the same dimensions but different ground plane printed on opposite side of the radiator, the planar monopole antenna added more resonances to the design, thereby, enhancing the bandwidth to cover the whole UWB spectrum from 2.7-10.7 GHz.

The chapter also demonstrated the time-domain performance of the antennas in free space and with phantoms. In this study, the simulated and measured results demonstrate that the performance of the proposed antennas for microwave imaging applications could be enhanced by immersing the antenna elements in coupling medium. We have also demonstrated that the antennas could detect small object with 3 mm in radius. At this stage image reconstruction has not been attempted as the focus of this study is to design small UWB antennas for microwave imaging. However, the results and the designs presented may be used as a step for future time-domain 3D experimental investigations and imaging algorithms.

# References


[1] M. Klemm, I. J. Craddock, J. A. Leendertz, A. Preece, and R. Benjamin, "Radar-based breast cancer detection using a hemispherical antenna array-experimental results," *IEEE Transaction on Antennas and Propagation*, vol. 57, pp. 1692–1704, June 2009.

[2] R. Nilavalan, I. J. Craddock, A. Preece, J. A. Leendertz, and R. Benjamin, "Wide-band microstrip patch antenna design for breast tumor detection," *IET Microwave, Antenna and Propagation*, vol. 1, pp. 277–281, April 2007.

[3] S. Choi, J. Park, S. Kim, and J. Y. Park, "A new ultra-wideband antenna for uwb applications," *Microwave and Optical Technology Letters*, vol. 40, pp. 399–401, March 2004.

[4] X. Chen, J. Liang, S. Wang, Z. Wang, and C. Parini, "Small ultra wideband antenna for medical imaging," *Loughborough Antennas and Propagation Conference*, March 2008.

[5] C. A. Balanis, *Antenna Theory : Analysis and Design.* New York: John Wiley & Sons, third ed., 2005.

[6] M. John and M. J. Ammann, "Spline-based geometry for printed monopole antennas," *Electronic Letters*, vol. 43, no. 6, pp. 317–319, 2007.

[7] J. Volakis, *Antenna Engineering Handbook.* McGraw-Hill, fourth ed., 2007.

[8] L. J. Chu, "Physical limitations of omni-directional antennas," *J. Appl. Phys*, vol. 19, pp. 1163–1175, December 1948.

[9] R. F. Harrington, "Effect of antenna size on gain, bandwidth, and efficiency," *J. Res. Nat. Bur. Stand.-D, Radio Propagat*, vol. 1-12, pp. Vol. 64D,, January-February 2003.

[10] R. Hansen, "Fundamental limitations in antennas," *Proc. IEEE*, vol. 69, pp. 170–182, February 1981.

[11] J. S. McLean, "A re-examination of the fundamental limits on the radiation q of electrically small andennas," *IEEE Transaction Antennas and Propagation*, vol. 54, pp. 672–676, May 1996.

[12] X. Chen, J. Liang, L. Guo, C. Chiau, and C. Parini, "Planar uwb monopoles and their operations," *The first European Conference on Antenna and Propagation (EuCAP 2006), Nice, France*, November 2006.

[13] K. Bahadori and Y. Rahmat-Samii, "A miniaturized elliptic-card uwb antenna with wlan band rejection forwireless communications," *IEEE Transactions on Antennas and propagation*, vol. 55, no. 11, pp. 3326–3332, 2007.

[14] Z. N. Chen, M. J. Ammann, M. Y. W. Chia, and T. S. P. See, "Circular annular planar monopoles with em coupling," *IEE Proceedings . Microwave Antennas and Propagation*, vol. 150, pp. 269–273, August 2003.

[15] D. Pozar, *Microwave Engineering*. New York: John Wiley & Sons, fourth ed., 2012.

[16] P. Meaney, M. Manning, D. Li, S. Poplack, and K. Paulsen, "A clinical prototype for active microwave imaging of the breast," *IEEE Transactions on Microwave Theory and Techniques*, vol. 48, pp. 1841–1853, November 2000.

[17] E. Fear, S. Hagness, P. Meaney, M. Okoniewski, and M. Stuchly, "Enhancing breast tumor detection with near-field imaging," *IEEE Microwave Magazine*, pp. 48–56, March 2002.

[18] B. Yeboah-Akowuah, "Study of ultra-wideband antenna," *Masters Thesis, Submitted to Queen Mary, University of London*, August 2009.

[19] L. Guo, S. Wang, X. Chen, and C. Parini, "A small printed quasi-self-complementary antenna for ultrawideband systems," *Antennas and Wireless Propagation Letters, IEEE*, vol. 8, pp. 554–557, 2009.

[20] *CST Microwave Studio, Computer Simulation Technology*, 2014.

[21] P. M. Meaney, F. Shubitidze, M. W. Fanning, M. Kmiec, N. R. Epstein, and K. D. Paulsen, "Surface wave multipath signals in near-field microwave imaging," *International Journal of Biomedical Imaging*, vol. 2012, p. 11, January 2012.

[22] A. H. Golnabi, P. M. Meaney, and K. D. Paulsen, "Tomography microwave imaging with incorporated prior spatial information," *IEEE Transactions on Microwave Theory and Techniques*, vol. 61, pp. 2129–2136, May 2013.

[23] M. Bassi, M. Caruso, M. S. Khan, A. Bevilacqua, A.-D. Capobianco, and A. Neviani, "An integrated microwave imaging radar with planar antennas for breast cancer detection," *IEEE Transaction on Microwave Theory and Techniques*, vol. 61, pp. 2108–2118, May 2013.

[24] J. Bourqui, M. Okoniewski, and E. C. Fear, "Balanced antipodal vivaldi antenna with dielectric director for near-field microwave imaging," *IEEE Antennas and Wireless Propagation Letters*, vol. 58, pp. 2318–2326, July 2010.

[25] M. Ahadi, M. B. M. Isa, M. I. B. Saripan, and W. Z. W. Hasan, "Square monopole antenna for microwave imaging, design and characterisation," *IET Microwaves, Antennas and Propagation*, vol. 9, no. 1, pp. 49–57, 2015.

# Chapter 5

# Planar Wearable Antenna at 2.45 GHz ISM Band

As has been discussed in chapeter 2, section 2.3, many antennas have been proposed for body-worn devices utilising the Industrial, Scientific, and Medical (ISM) band at 2.45 GHz. In previous chapters, we reported about broadband antennas for high data rate and wider bandwidth communications. For most applications that require long range communications and resistant to interference, UWB antennas tend to be the dominant choice. However, for short range communication systems and frequency specific applications the narrow band antennas offer alternative options.

There are a number of antennas such as monopoles designed for specific applications and frequency band. Many of such structures are resonant antennas that generally have dimensions close to half or quarter of a wavelength. These antennas are often simple structures with relatively narrow bandwidth. The emergence of Bluetooth enable wearable devices have led to the development of antennas for such communication systems. Many systems such as IEEE 802.11 wireless LAN and personal area network employ Bluetooth devices for communication.

In this study we propose a new printed monopole antenna with a circular slot (PMA-CS). The antenna is designed to operate at 2.45 GHz for Bluetooth enable wearable applications. We control the resonant frequency of the antenna with the circular slot. The design simplicity and good performance in close proximity to the human body suggest that this antenna is a good candidate for body-centric applications.

## 5.1 Antenna Geometry, Design Process, and Optimisation

The proposed structure is a printed monopole antenna with a circular slot (PMA- CS) derived from a rectangular radiator with a semicircular bottom [1–3]. Antennas of this nature are generally designed for broadband applications, however, with a circular slot the antenna can resonate at a single-frequency band.

The design process follows the construction of a rectangular radiator with a semicircular bottom without any slot as shown in Fig. 5.1. The surface current and other design metrics such as return loss, efficiency and gain were analysed against the objectives of this research work. The surface current contours as shown in Fig. 5.2 indicate that most of the currents were concentrated at the edges and also the area around the ground plane and the stripline. It follows that etching a circular slot at the centre of the radiator will improve the antenna performance by shifting the resonant frequency to a lower range.

The $S_{11}$ analysis (See Fig. 5.3) shows that the structure without any slot provides poor return loss and input matching. This could be attributed to fact that the surface-wave current becomes more severe and pronounced on the radiator giving rise to poor efficiency resulting in poor radiation. To overcome the antenna poor return loss, input impedance and radiation pattern, a slot was etched on the radiator for the following reasons: (i) to make the radiator act approximately as a resonant cavity (short circuit (PEC) walls on top and bottom, open-circuit (PMC) walls on the sides (ii) a strong field is set up inside the cavity, and a strong current on the (bottom) surface of the radiator that give rise to good radiation.

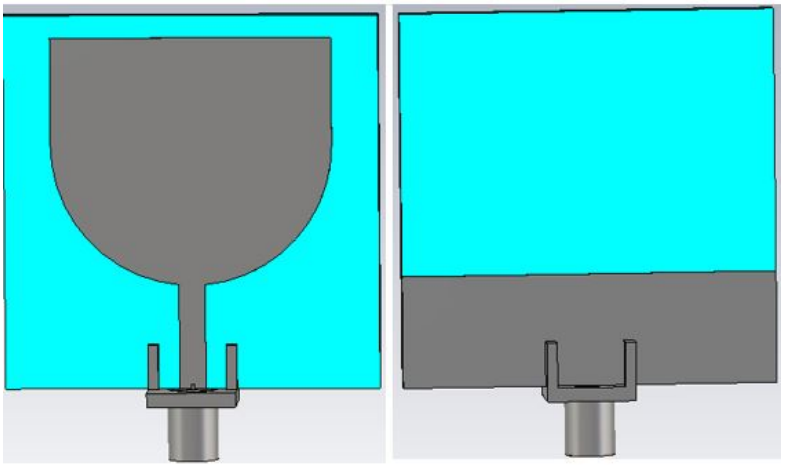

FIGURE 5.1: Geometry of PMA without circular slot. Top view (left), Bottom view (right).

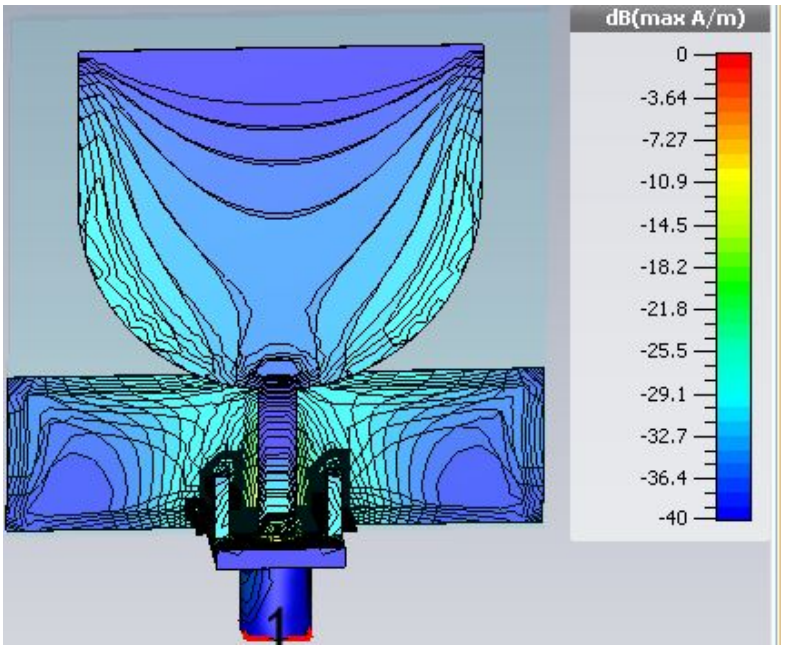


FIGURE 5.2: Surface current contours of Fig. 5.1

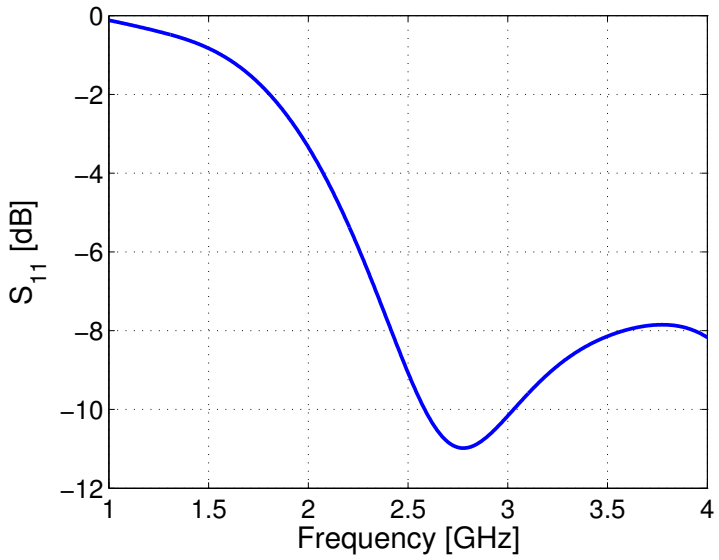


FIGURE 5.3: Return loss curve for the radiator without the circular slot (Fig. 5.1)

Taking the above into consideration, a new design is proposed, as shown in Fig. 5.4, which is a printed monopole antenna with a circular slot (PMA-SC) on FR4 substrate with $\varepsilon_r = 4.6$ and thickness 1.6mm. The total size of the substrate is 40 x 40 $mm^2$. At the back of the substrate is a partial rectangular ground plane measuring 40 x11.9 $mm^2$. The circular slot with optimised radius $r$ =11.8 $mm$ controls the resonant frequency of the antenna. In [1–3], antennas using a semicircular radiator were proposed for ultra-wideband applications. However, those antennas were designed for higher and frequency-independent applications. The novelty of this design lies on the use of the circular slot

on the radiator, which provides an easy mechanism to control the antenna resonant frequency by changing the radius of the circular slot $r$. The use of this slot also reduces the antenna size by lengthening the current path, and results in a frequency shifting from the UWB range to a lower frequency, which is chosen as 2.45 GHz for on-body applications. Furthermore, the advantage of the present design is that it is relatively simple, easy to prototype and manufacture. A 50 Ω coaxial transmission line was used to feed the antenna.

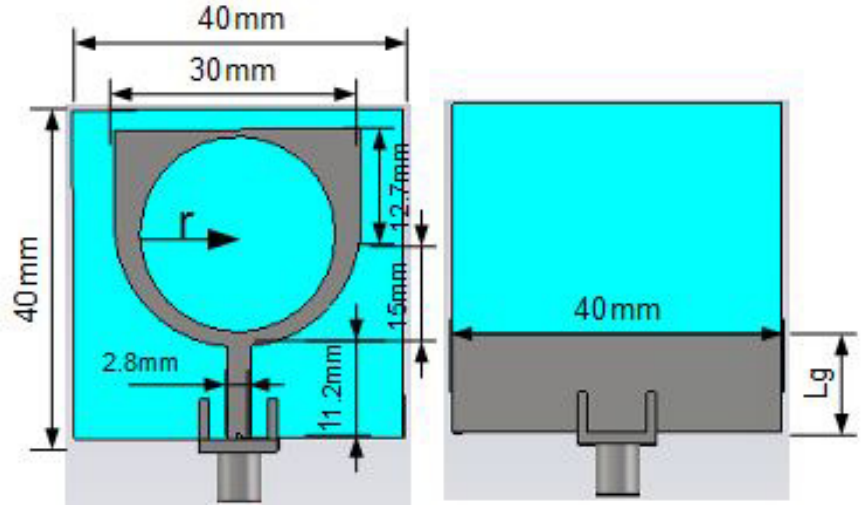


FIGURE 5.4: Geometry of PMA-CS. Top view (left), Bottom view (right)

The surface current and H-field distribution of the proposed antenna (PMA-CS) are shown in Fig.5.5.

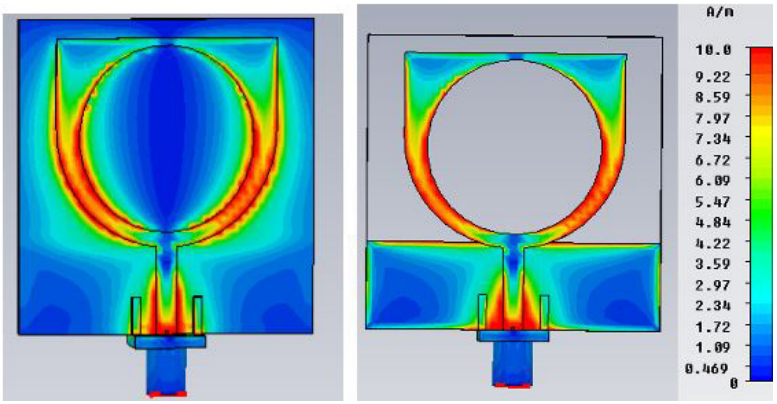


FIGURE 5.5: H-field distribution( left) Surface current (right) of PMA-SC

### 5.1.1 Parametric Studies (PMA-CS)

Two parameters that affect the performance of the proposed antenna are the circular slot radius $r$ and the ground plane length $Lg$. The antenna was simulated for different

dimensions for these two parameters.

(i) Effect of the circular slot radius $r$

The radius of the circular slot that controls the resonant frequency was simulated at different dimensions to observe its effect on the antenna, with the ground plane fixed at its optimal value 40 x 8.068 $mm^2$. Fig. 5.6 shows the $S_{11}$ response for different slot radius $r$. It is clear from the result that $r$ has effect on the resonant frequency and the input impedance, for example when $r$= 9.93 mm the resonant frequency was 2.58 GHz which is higher than ISM band 2.45 GHz and also with a very poor return loss.

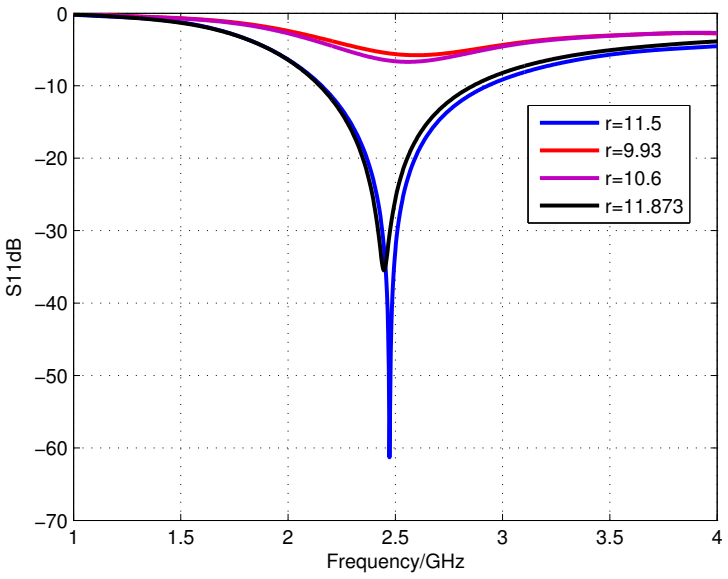


FIGURE 5.6: Simulated return loss curves for different dimensions of the circular slot radius $r$ with the optimal designs.

(ii) Effect of the ground plane length $Lg$

The other parameter that affects the proposed antenna is the ground plane length $Lg$. With the optimised circular slot radius $r$ fixed at 11.5 mm and the ground plane width at 40 mm, the dimensions of $Lg$ were varied to observe its effect on the antenna performance. Fig. 5.7 shows the variations of $Lg$. The optimised value was found to be 8.068 mm. The results shows that the ground plane length $Lg$ affects the input impedance and the matching of the antenna.

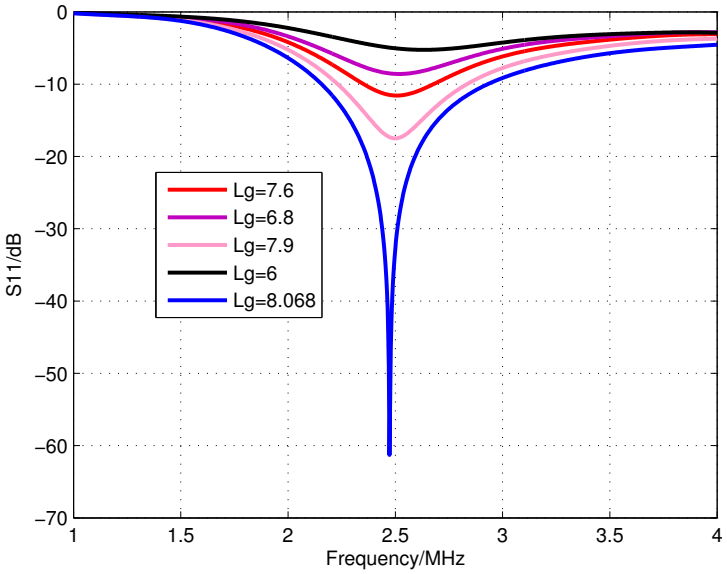


FIGURE 5.7: Simulated return loss curves for different dimensions of the ground plane length $Lg$ with the optimal designs.

The new design shows a better performance in terms of return loss and input matching as a result of the introduction of the circular slot. Fig. 5.8 compares the simulated $S_{11}$ of the two antenna i.e the optimised structure with circular slot and without slot.

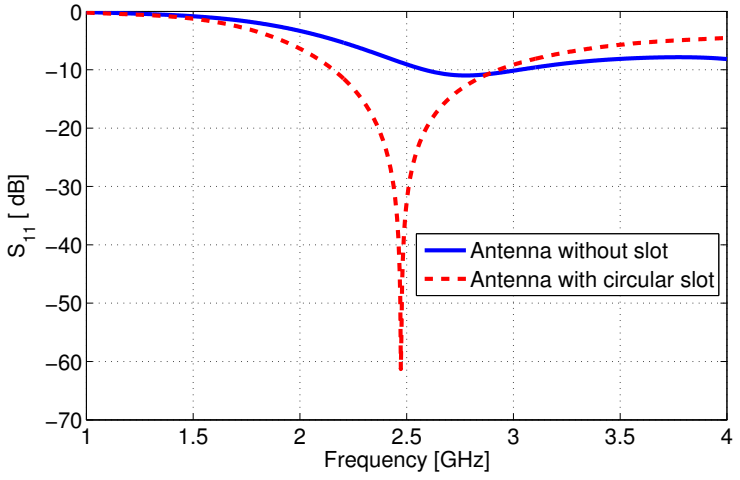


FIGURE 5.8: $S_{11}$ comparisons showing the optimised structure with circular slot and without slot.

### 5.1.2 Simulation Studies to Evaluate Performance

The proposed antenna was simulated in free space and in the vicinity of two different phanoms, a simplified three-layer phantom composed of skin ($\varepsilon_r = 45.85, \sigma = 1.59$), fat

($\varepsilon_r = 5.28, \sigma = 0.1$) and muscle ($\varepsilon_r = 52.73, \sigma = 1.74$) [4] with dimensions (50 mm x 50 mm x 400 mm) equivalent to human arm taken from [5] as shown in Fig. 5.9, and 2/3 muscle equivalent-phantom ($\varepsilon_r = 35.15, \sigma = 1.16$) with dimensions 180 mm x 60 mm x 60 mm taken from [6].

We observed the effect of human body in close proximity of the antenna. The separation gap between the antenna and the phantom was varied between 3 mm to 15 mm to observe the antenna response and performance. Fig. 5.10 shows the simulated free space and on-body return loss curves. There is about 3.5% detuning between the free space simulation and on-body simulation when the gap is 15 mm.

Fig. 5.10 shows that the response of the antenna in free space and on-body are similar, suggesting that the antenna does not detune significantly and could be a good candidate for body-centric applications. As the antenna moves away from the body, its performance converges to the free space performance.

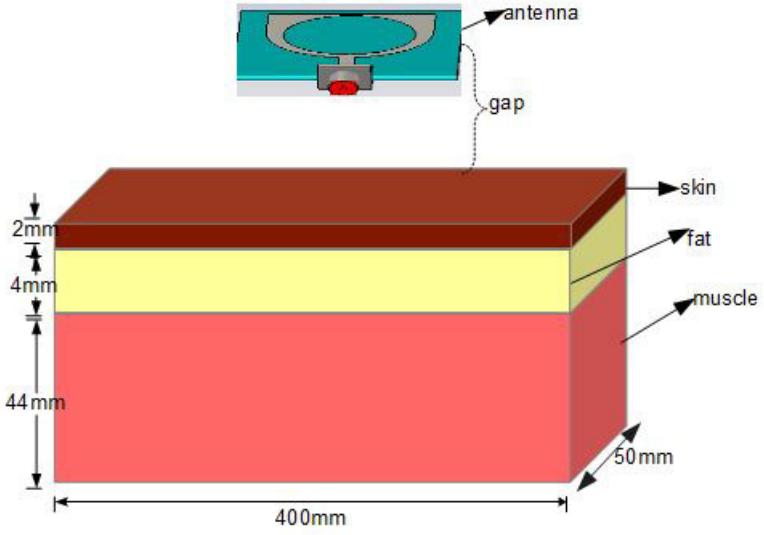


FIGURE 5.9: Three-layer phantom model for CS MSA simulation .

Fig. 5.11 shows the free space and on-body radiation pattern of the antenna. The work also shows that the antenna exhibits quasi-omnidirectional radiation patterns in both free-space and on-body in the elevation plane and more directive in the azimuthal plane. It also appears that in the azimuth plane nearly the entire lobe of radiation, which propagates in the direction of the models is absorbed due to the lossy characteristic of the tissues that compose the models. The free space radiation pattern stays relatively constant from the body, but the on-body pattern has high backlobes due to losses in the tissue. Moreover, the total efficiency of the proposed antenna in free space is almost 100% although this is not entirely accurate for practical reasons and 46% on-body efficiency. A realised gain of 2.79 dBi has been observed (See Fig. 5.16) .

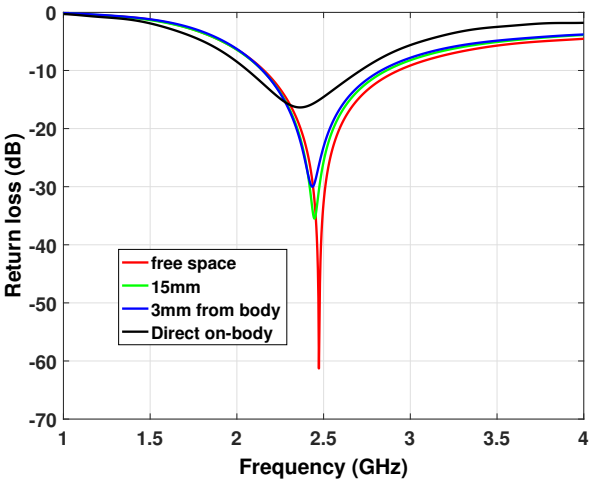


FIGURE 5.10: Simulated return loss curves for free space and on-body with optimised parameters $r = 11.5$ mm, $L_g = 11.932$ mm..

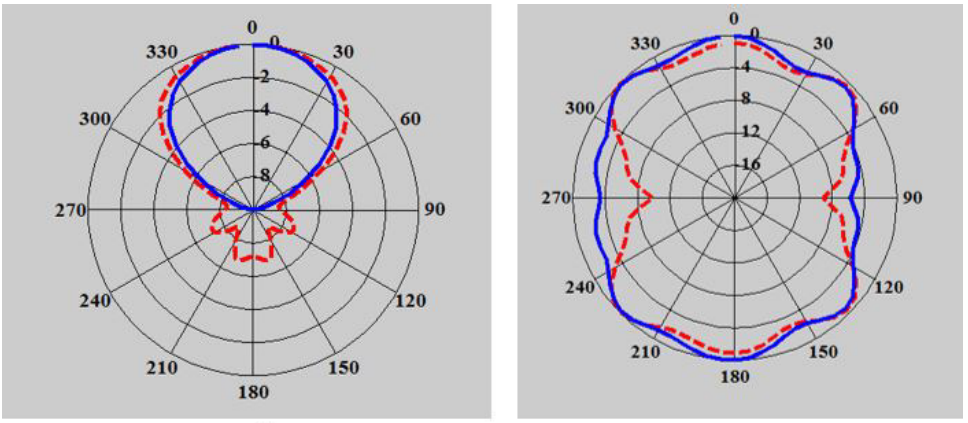


FIGURE 5.11: Simulated radiation pattern of the (PMA-CS) antenna in free space and on-body using the three-layer model of Fig. 5.9 (a) azimuth plane (b) elevation plane, (red dotted line on the body), (blue solid line in free space).

Fig. 5.12 shows the specific absorption rate (SAR) distribution in the ISM band calculated with the antenna placed 3 $mm$ away of the three-layer tissue model used in Fig. 5.9. The antenna was fed with a 1 $W$ peak input reference power. In accordance to the IEEE C95.1-2005 standard, the SAR average value over 10 $g$ of human tissue mass should not exceed 2 $W/Kg$ [8]. The predictions from this figure suggest that the maximum SAR for this antenna is well below regulation requirements.

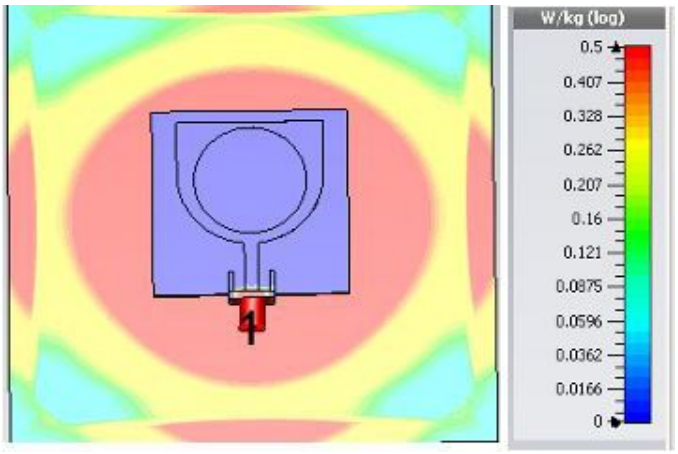


FIGURE 5.12: SAR distributions for PMA-CS when placed 5 mm away from the three-layer tissue model of (Fig. 5.9)

## 5.2 Measured Performance of PMA-CS

The prototype of PMA-CS is shown in Fig. 5.13. The antenna was measured with a M9375A vector network analyser (VNA) at Keysight laboratories in Shenzhen, China. The antenna was measured first in free space and the results were compared to the simulations presented in [7]. Fig. 5.14 shows that the measured free-space return loss agrees very well with free-space simulated results.

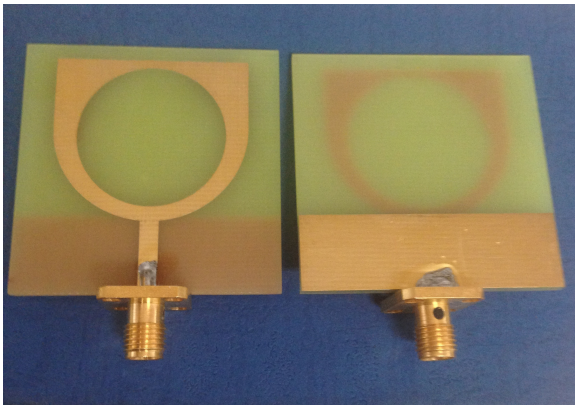

(a)

FIGURE 5.13: Photograph of the fabricated prototype.

The on-body measurements were carried out in anechoic chamber at The Chinese University of Hong Kong (CUHK), where the antenna under test was placed along the arm of real human subject ( age = 28 years, weight = 80 kg, height = 174 cm, BMI = 26). We carried out the measurements by varying the gap from 5 mm to 15 mm between the antenna and the human arm. The measured reflection coefficient is shown in Fig. 5.15. There is reasonable agreement between the simulated and measured results at all the separation gaps between the antenna and the arm.

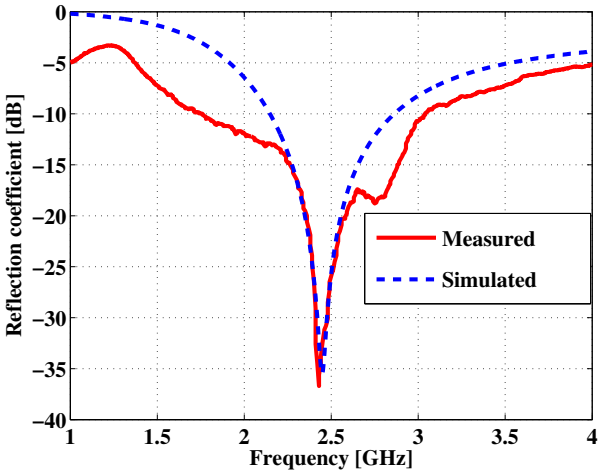


FIGURE 5.14: Simulated and measured reflection coefficient of PMA-CS antenna in free space

The gain pattern was deduced by measuring transmission coefficient of about 2 cm between the single output of a standard-gain horn antenna and the differential terminals of the antenna under test still attached to the arm of the volunteer for different azimuth plane orientation. The measured values were then calibrated taking into account the path loss and mismatch at both ends.

In comparison with the measured -10dB bandwidth in [9], our antenna operates from 2.12-2.68 GHz with a bandwidth of 560 MHz as opposed to 120 MHz. The antenna robustness in close proximity to human body, simplicity, and possible easy circuit integration along with good radiation pattern and bandwidth suggest that it is a good candidate for body-centric application (off-body).

We summarised the free space and on-body performance in Table 5.1.

TABLE 5.1: Performance of the PMA-CS in free space and on the body

| Parameter | Free Space | On-body |
|---|---|---|
| Resonance Frequency (GHz) | Simulated 2.45<br>Measured 2.45 | Simulated 2.45<br>Measured 2.48 |
| Bandwidth (-10 dB) GHz | Simulated 0.65<br>Measured 0.57 | Simulated 0.64<br>Measured 0.56 |
| Gain (dBi) | Simulated 2.79<br>Measured 2.82 | Simulated -6.2<br>Measured -5.1 |
| Total efficiency (%) | 98 | 46.5 |

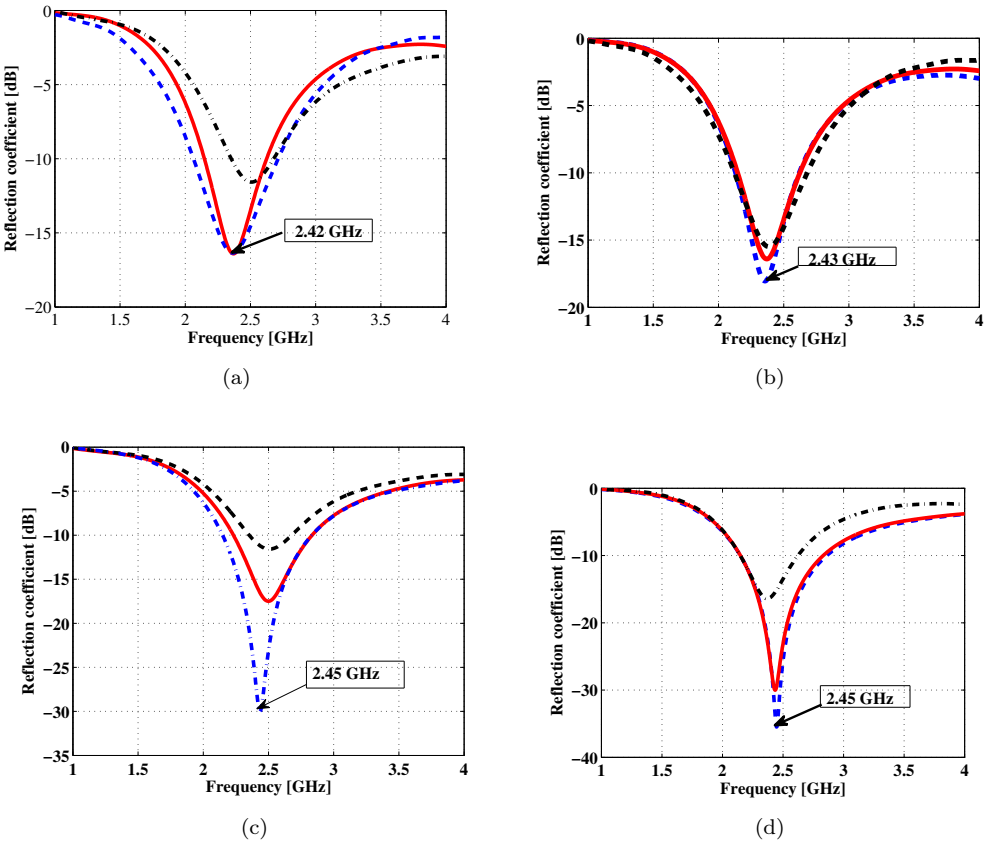


FIGURE 5.15: Simulated and Measured reflection coefficient of the antenna using Fig. 5.9 and 2/3 muscle at various distances from (a) direct on body (b) 5 mm away (c) 10 mm away and (d) 15 mm away, (blue dotted line simulated on arm), (black dotted line ) simulated on 2/3 muscle, and (red dotted line) measured

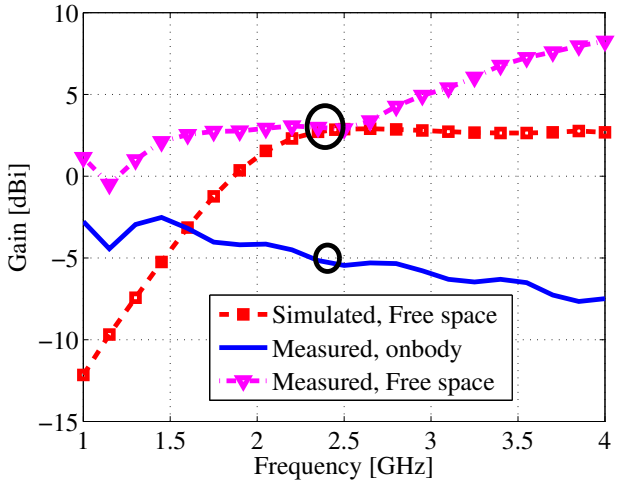


FIGURE 5.16: Realised gain of the proposed antenna showing the following; simulated free space, measured free space, and measured on-body.

## 5.3 Summary

The chapter presents a novel antenna for wearable communications. We control the resonant frequency of the antenna and the input impedance with the radius of the circular slot on the radiator. We took measurements for a range of positions between the antenna and real human subject. The presented simulations and measurements showed that the antenna does not de-tune when in close proximity to the human body. The design simplicity and good performance in close proximity to the human body suggest that this antenna is a good candidate for body-centric applications.

# References


[1] S. Nair, V. Shameena, R. Dinesh, and P. Mohanan, "Compact semicircular directive dipole antenna for uwb applications," *Electronics Letters*, vol. 47, pp. 1260–1262, November 2011.

[2] N. D. Trang, D. H. Lee, and H. C. Park, "Compact printed ultra-wideband antenna with three subband notches," *Communications and Electronics (ICCE), 2010 Third International Conference*, pp. 348–351, Aug 2010.

[3] K. P. Ray, Y. Ranga, and P. Gabhale, "Printed square monopole antenna with semi-circular base for ultra-wide bandwidth," *Electronics Letters*, vol. 43, pp. 13–14, March 2007.

[4] "Calculation of the dielectric properties of body tissues," institute for applied physics, italian national research council." website. http://niremf.ifac.cnr.it/tissprop.

[5] C. H. Lin, K. Saito, M. Takahashi, and K. Ito, "A compact planar inverted-f antenna for 2.45 ghz on-body communications," *Antennas and Propagation, IEEE Transactions*, vol. 60, pp. 4422–4426, Sept 2012.

[6] K. Ito, W. Xia, M. Takahashi, and K. Saito, "An implanted cavity slot antenna for medical communication systems," in *Antennas and Propagation, 2009. EuCAP 2009. 3rd European Conference on*, pp. 718–721, March 2009.

[7] B. Yeboah-Akowuah, P. Kosmas, and Y. Chen, "A low profile microstrip patch antenna for body-centric communications at 2.45ghz band," in *2015 9th European Conference on Antennas and Propagation (EuCAP)*, pp. 1–3, May 2015.

[8] "Ieee standard for safety levels with respect to human exposure to radio frequency electromagnetic fields, 3 khz to 300 ghz amendment 1: Specific absorption rate (sar) limits for the pinna) (amendment 1 to ieee std c95.1-1991 (1999 ed.) c95.1b) superseded by c95.1/d2.4," *IEEE Std PC95.1/D2.3*, 2006.

[9] C. H. Lin, K. Saito, M. Takahashi, and K. Ito, "A compact planar inverted-f antenna for 2.45 ghz on-body communications," *IEEE Transactions on Antennas and Propagation*, vol. 60, pp. 4422–4426, Sept 2012.

# Chapter 6

# Implantable Antennas

Wireless communication systems and implantable antennas are needed for communication with implantable medical devices (IMDs) such as cardiac pacemakers and defibrillators. Designing antennas for embedded applications is extremely challenging because of reduced antenna efficiency, impact of the environment on the antenna, the need to reduce antenna size, and the very strong effect of multi-path losses. Ultra-small devices small enough to be injected in human body and the desire to communicate with them will inevitably lead to the need for miniaturised antennas embedded in lossy environments.

In chapter 2, section 2.2, we reviewed the state-of-the-art of implantable antennas. We reviewed some of the implantable antennas proposed for many applications such as glucose monitoring devices, wireless endoscope capsule and cardiac pacemaker. In this chapter we propose two implantable antennas with two different structural configurations employing numerical techniques to meet the objectives and the requirements of this study. The antennas are very compact with much improved bandwidths at the operating frequencies.

## 6.1 Design techniques

The section discusses the theoretical background of the techniques employed to achieve efficient antenna designs in line with the project objectives. The requirements and constraints related to the design of implantable antennas include: miniaturisation, biocompatibility, patient safety, low power consumption, efficiency and far-field gain. In order to address some of the aforementioned challenges and issues, some advanced designed techniques such as (1) the use of high permittivity substrates (2) stacking of patches (3) meandering patch surface and (4) shorting pins were employed.

The fundamental theory of electromagnetism dictates that electromagnetic waves travel as the speed of light. In electromagnetism, one of the fundamental parameters that affects the propagation of electric field in a medium is permittivity $\varepsilon$, which describes the materials ability to support an electric field. In free space the speed of light is given as (6.1)

$$c = \lambda f \Rightarrow \lambda = \frac{c}{f} \tag{6.1}$$

where $\lambda$ is wavelength and $f$ is the frequency. The relative permittivity $\varepsilon_r$ with respect to free space permittivity $\varepsilon_o$ is expressed as (6.2)

$$\varepsilon_r = \frac{\varepsilon}{\varepsilon_o} \tag{6.2}$$

The speed of propagation $c$ in a medium is also given as (6.3)

$$c = \frac{1}{\sqrt{\varepsilon_r \mu_r}} = \frac{c_o}{\sqrt{\varepsilon_r \mu_r}} \tag{6.3}$$

where $c_o$ is the speed of light in free space, $\mu_r$ is relative permeability.

It follows that

$$\lambda = \frac{c}{f} = \frac{c_o}{f\sqrt{\varepsilon_r}} = \frac{\lambda_o}{\sqrt{\varepsilon_r}} \tag{6.4}$$

where $\lambda_o$ is the wavelength in free space.

Equation (6.4) indicates that by using a high permittivity substrate (dielectric material) the propagation speed in the medium as well as the wavelength can be reduced. In antenna design we take advantage of the fact that using high-permittivity dielectric substrate can reduce the dimensions of the antennas. In particular, the use of high permittivity substrates can shorten the effective wavelength and thus reduce the antenna resonant frequency. In the literature [1–4], high permittivity substrates such as Roger 3210 with $\varepsilon_r = 10.2$ and ceramic alumina, $\varepsilon_r = 9.4$ have been used to reduce the size of antennas.

Another popular technique used to miniaturise antennas for body-centric applications is lengthening the current flow on the patch surfaces with an enhanced inductive effect (L). The meandering can be achieved by inserting several narrow slits at the patch non-radiating edges resulting in a cross-coupling effect between adjacent arms of the meander, thereby creating localised electric field storage, and hence an enhanced capacitive effect (C). The effect lowers the antenna fundamental resonant frequency and thus reduces the antenna size at a fixed operating frequency [1, 5–8].

Multi-layered stacked patches have been employed to design dual-band antennas for various applications. For example, dual-band microstrip patch antennas have been reported in the literature [9, 10]. Patch-stacking reduces the size of the antenna by increasing the length of the current path. When two patches are vertically stacked, the distance

between the patches can be controlled so that they are coupled together to act as a single wideband antenna [11].

Recently, many stacked patches designed for single frequency operation have been reported [3, 12–15]. In addition to this technique .i.e. vertically stacking the patch, inserting a shorting pin between the ground plane and the patch reduces the physical size of the antenna at the operating frequency. A popular antenna using this type of arrangement is the planar inverted-F antenna (PIFA) where the shoring pin or shorting post affects the fundamental frequency of the antenna [16].

## 6.2 Proposed Antenna Designs and Optimisation

In this study, we look at two designs for implants in the MICS (402-405 MHz) band employing the aforementioned techniques. We have chosen these two designs to demonstrate the underlying principle (mirror image arrangement) that has been explained in section (6.3). We have also managed to miniaturise the size and the volume of the antennas with this mirror image arrangement.

### 6.2.1 Compact Circular PIFA (CC-PIFA)

The proposed antenna is a multi-layered structure consisting of a (a) ground plane and two circular patches (radiators), with (b) lower patch and (c) upper patch as shown in Fig. 6.1. The upper patch is the mirror image of the lower patch etched on the second layer substrate. The ground plane has a radius of 5 mm and both patches have a 4.5 mm radius. Sandwiched between the patches is a circular Rogers 3210 substrate ($\varepsilon_r = 10.2$, $tan\delta = 0.003$) with thickness 0.635 mm and radius 4.5 mm. Such high permittivity dielectric substrates have been used to achieve miniaturisation and reduce the antenna resonant frequencies [3], [13]. On top of the upper patch is a superstrate with same properties as those of the substrates, and its purpose is to cover the antenna and preserve its biocompatibility and robustness.

In order to lengthen the effective current path on the patch surface as well as enhance the bandwidth at the operating frequency, three carefully placed hooked-shaped slots are cut on the patch. In [13], an antenna of a similar structure was proposed for MICS operation where similar slots were used to lengthen the current path and achieve miniaturisation. The difference between our CC-PIFA and [13] is the number of slots and orientation of the lower and upper patch. Our design encompasses mirror image arrangement to enhance bandwidth at the operating frequency. With the mirror image approach, the two

radiators have closely related resonant frequencies. The radiators coupled together resulting in overlapping of these resonance, hence an improved bandwidth at the operating frequency.

The distance from one slot to another is 1.2 mm and the optimised width $w$ of the slot was found to be 0.35 mm. The inner probe of the feed introduces inductance so a small optimised gap $g = 0.3$ mm was cut to provide a capacitive effect to balance the inductive effect and also to improve the impedance matching of the antenna. To further reduce the size of the antenna, a shorting pin $S$ with radius of 0.3 mm and centre (x = 1.5 mm, y= 2.5 mm), referenced to the origin of the ground plane, connects the ground plane and the lower patch. Both patches are excited by 50 Ω coaxial cable F of length L = 8 mm as shown in Fig. 6.1(d) with inner conductor radius 0.2 mm and centre (x= 0.9 mm, y= -3.7 mm) referenced to the origin of the ground plane.

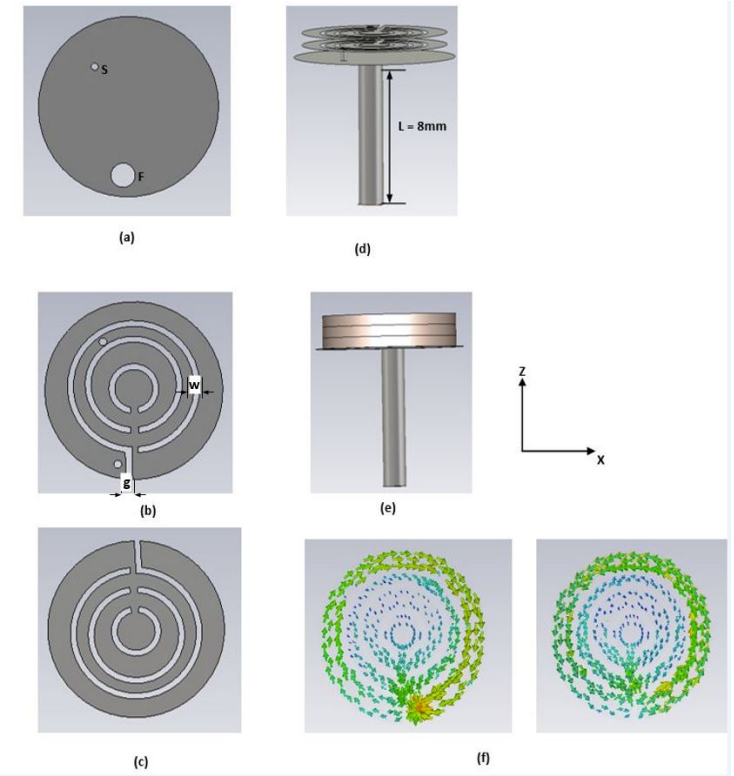


FIGURE 6.1: Geometry of Compact Circular PIFA: (left) including the: (a) ground, (b) lower patch,(c) upper patch, (d) view of the vertically stacked patches, (e) vertically stacked antenna with substrates, (f) and resulting surface current distribution (right)

#### 6.2.1.1 Simulation Studies for CC-PIFA

The antenna was modelled and simulated using CST's Microwave Studio. As the antenna is intended for embedded application inside the human body, the design and simulations

TABLE 6.1: Tissues Electric Properties and mass densities at 402 MHz

| Tissue | ($\varepsilon_r$) | Conductivity ($\sigma$,s/m) | Mass Density(Kg/m$^3$) |
|---|---|---|---|
| Skin | 46.7 | 0.69 | 1010 |
| Fat | 11.6 | 0.08 | 920 |
| Muscle | 58.8 | 0.84 | 1040 |

were performed inside a simplified three-layer tissue (skin, fat, muscle) model shown in Fig. 6.2. A similar three-layer tissue model was used to simulate low-profile antennas on human chest implants in [17]. The phantom dimensions, the thickness of the skin and fat, the antenna position within the three-layer model are similar to those reported in the literature [17]. We chose this phantom to compare the performance of our antenna with the one reported. Both antennas resonate at 402 MHz, however, the size and the volume of our antenna is 97% smaller as compared to [17].

Table 6.1 shows the electrical properties of the tissues taken from [17]. The antenna was implanted at h=10 mm within the muscle layer as shown in Fig. 6.2 and tuned to the resonant frequency by optimising the positions of the shorting pin S and feed F. The antenna was also placed in different positions to observe its response and robustness.

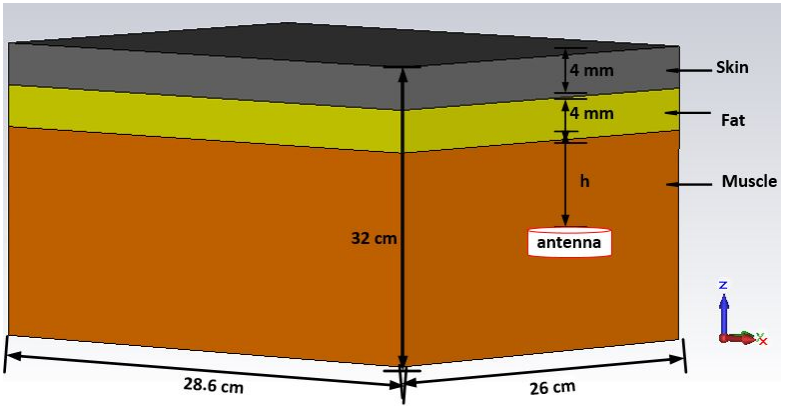


FIGURE 6.2: Three-layer simulation model (phantom) made up of skin, fat, and muscle used for implanted antenna in human chest

As shown in Fig. 6.3, the proposed antenna resonates at 402 MHz when implanted inside the muscle layer at depth h=10 mm, and its $S_{11}$ is -29.58 dB. The -10 dB impedance bandwidth is 100.45 MHz (356.56-457.01). The -10dB bandwidth shows a wider bandwidth as compare to similar antennas reported in [15, 17, 18]. The antenna was also implanted at different positions within the tissue to observe its response, characteristics and robustness. At the implantation depth h= 5 mm, the antenna resonates at 403 MHz with return loss of -29.58 dB, the same -10dB bandwidth as obtained for h=10 mm. When the antenna was positioned between the skin and fat layer, the resonant frequency shifted upwards to 553.6 MHz with $S_{11}$ of -8.9 dB. The detuning of the antenna to such

high frequency is attributed to the low permittivity and conductivity values of the fat tissue. Furthermore, waves scattered from the body will induce additional currents on the antenna thereby distorting the resonance and resulting in frequency detuning and degradation of the return loss.

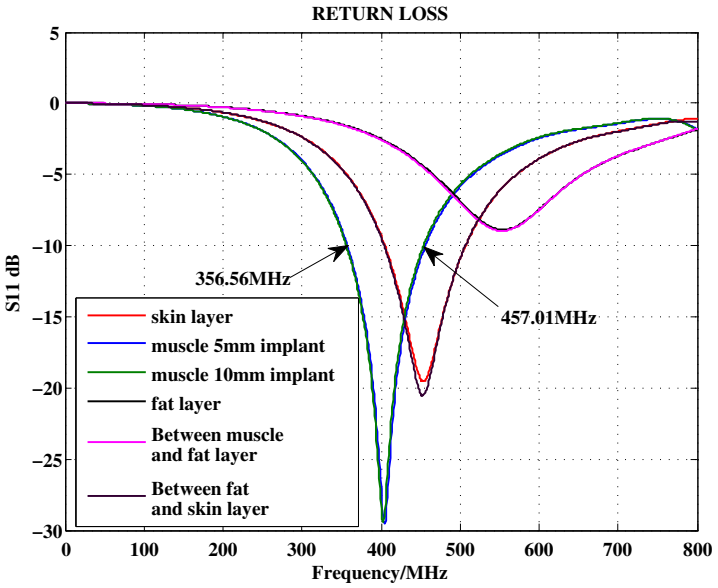


FIGURE 6.3: Return loss for different positions of CC-PIFA inside the three-layer phantom of Fig. 6.2

We observed similar responses when the antenna was placed at the centre of the fat layer or the interface between muscle layer and fat layer. When the antenna was placed at the skin/fat interface or the skin layer, the resonant frequency shifts to 453 MHz with $S_{11}$ around -21.5 dB. As seen from Table 6.1 the electrical properties of skin and muscle are very close, leading to similar resonant frequencies for the antenna operation even though the return loss at the skin layer is relatively weak.

The input impedance and voltage standing wave ratio (VSWR) have been shown in Fig.6.4. The radiation pattern has been shown in Fig. 6.5. The antenna gain is 1.86 dBi. As has been discussed in the previous chapter, electrically small antenna suffers from low radiation efficiency as result of decrease in size. We acknowledge the fact that this low gain is due to the low efficiency of the antenna, although the gain value is typical for antennas of this type with values around 1.5 dBi [19].

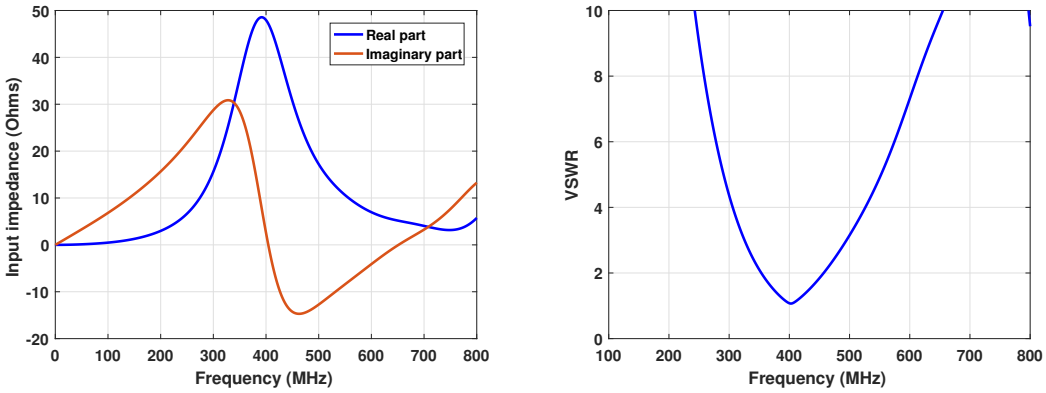


FIGURE 6.4: Input Impedance (left) VSWR (right)

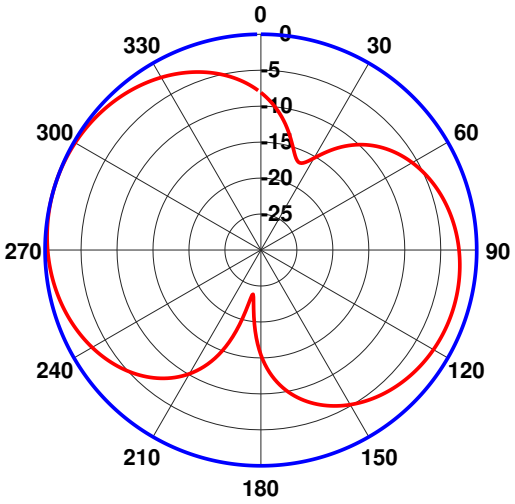


FIGURE 6.5: Normalised radiation patterns of the Compact Circular PIFA. (Red solid line: azimuth plane) and (blue solid line: elevation plane)

### 6.2.2 Compact Spiral PIFA (CS-PIFA)

In [17], a low profile spiral antenna was developed for human chest implants. However, the physical size of the antenna as compared to the proposed antenna is bigger. A new three-layer stacked PIFA antenna with the advantage of wide impedance bandwidth, compact size, and good radiation characteristics suitable for use in the biotelemetry communication when operating at the 402-405 MHz frequency band is proposed. For instance, the proposed Compact Spiral PIFA has overall volume of 251 $mm^3$ which is a reduction of about 97% compared to the reported work in [20] with a volume of $10240mm^3$ and also a third of recently reported PIFA with volume of 692 $mm^3$ [21], and about half a fraction of 458 $mm^3$ reported in [22].

TABLE 6.2: Design parameters of CS-PIFA

| Parameters | Dimensions(mm) |
|---|---|
| L1 | 11.05 |
| L2 | 12 |
| L3 | 10.6 |
| L4 | 11 |
| L5 | 10.6 |
| L6 | 8.2 |
| L7 | 7.5 |
| L8 | 5.7 |
| L9 | 5.2 |
| L10 | 3.2 |
| L11 | 2 |

The proposed antenna is a multi-layered structure with a rectangular ground plane and two vertically stacked meandered patches as shown in Fig. 6.6. Each radiating patch is etched on Rogers 3210 substrates ($\varepsilon_r = 10.2, \delta = 0.0027$) and thickness 0.635 mm. A superstrate with the same dimensions and properties as the substrates covers the structure to prevent direct contact of the patch and human tissue. The dimensions of the antenna is given in Table 6.2.

Both radiating patches have the same dimensions but the upper patch is the mirror image of the lower patch (i.e. the upper patch is 180° rotation of lower patch). The centre of the ground plane is set as the origin of the coordinate system unless stated otherwise. A 50 Ω coaxial probe **F** (x= 4.7 mm, 4.5y mm) is used to feed the antenna , while a 0.3 mm-radius shorting pin **S** (x= 2.3 mm, y= 2.3 mm) connects the ground plane with the lower patch to further reduce the size of the antenna. The inner conductor of the feed connects the lower patch which then excites the upper patch through electromagnetic coupling.

#### 6.2.2.1 Simulation Studies of Compact Spiral PIFA

The antenna was simulated using the same phantom Fig. 6.2 as used for the CC-PIFA studied previously with the same dimensions and tissue properties. The antenna was implanted 10 mm inside the muscle tissue and tuned to the required resonant frequency 404 MHz. Furthermore, the antenna was implanted in the fat and skin tissues to observe its performance and robustness. Fig. 6.7 shows the return loss when the antenna was positioned in the tissue. As observed from Fig. 6.7 the antenna also resonates at MedRadio frequency 433 MHz when implanted in the skin tissue. The resonant frequency has been shifted from 404 MHz to 433 MHz because the antenna is directly implanted beneath the skin layer in the body model. In the fat layer, the antenna resonates at 525.6 MHz with

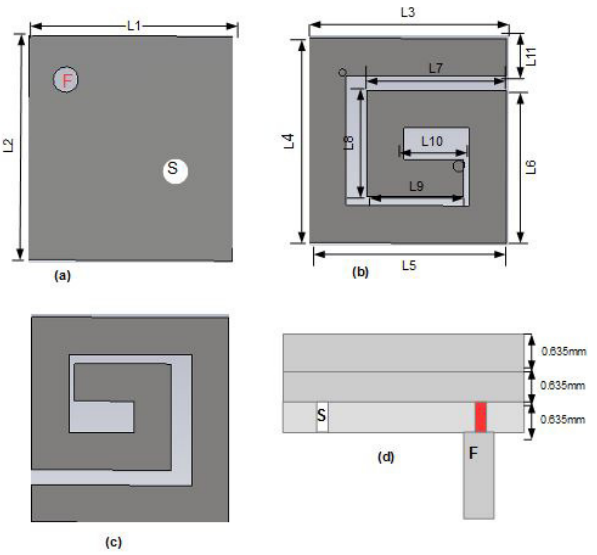


FIGURE 6.6: Geometry of Compact Spiral PIFA: (a) ground plane (b) lower patch (c) upper patch and (d) view of the vertically stacked antenna

deteriorating return loss of -2.8 dB. This is due to the larger equivalent permittivity and conductivity of muscle in comparison with skin and fat tissues which have smaller permittivities and conductivities. Fig. 6.8. depicts the input impedance, voltage standing ratio (Vswr) and the radiation pattern.

Table 6.3 shows the comparisons of the two proposed implantable antennas. There is no much difference between the two antennas in terms of performance, however, the circular type resonates at 402 MHz whiles the meandered type resonates at 404 MHz. The choice of any of these antennas for any application will be based on IMD configuration rather than performance.

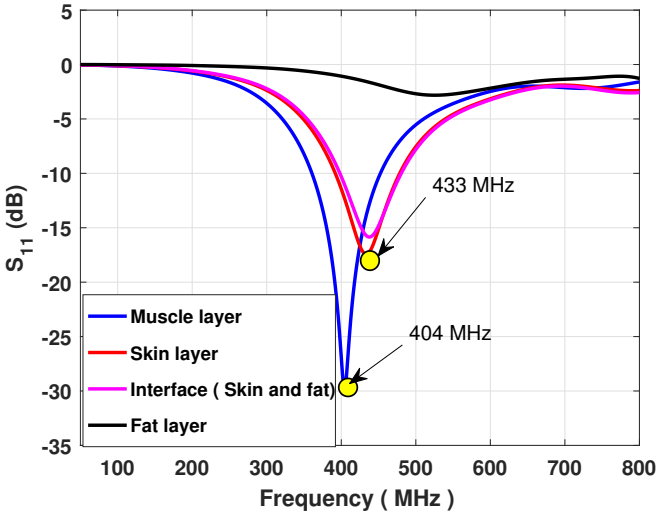


FIGURE 6.7: Return loss of Compact Spiral PIFA

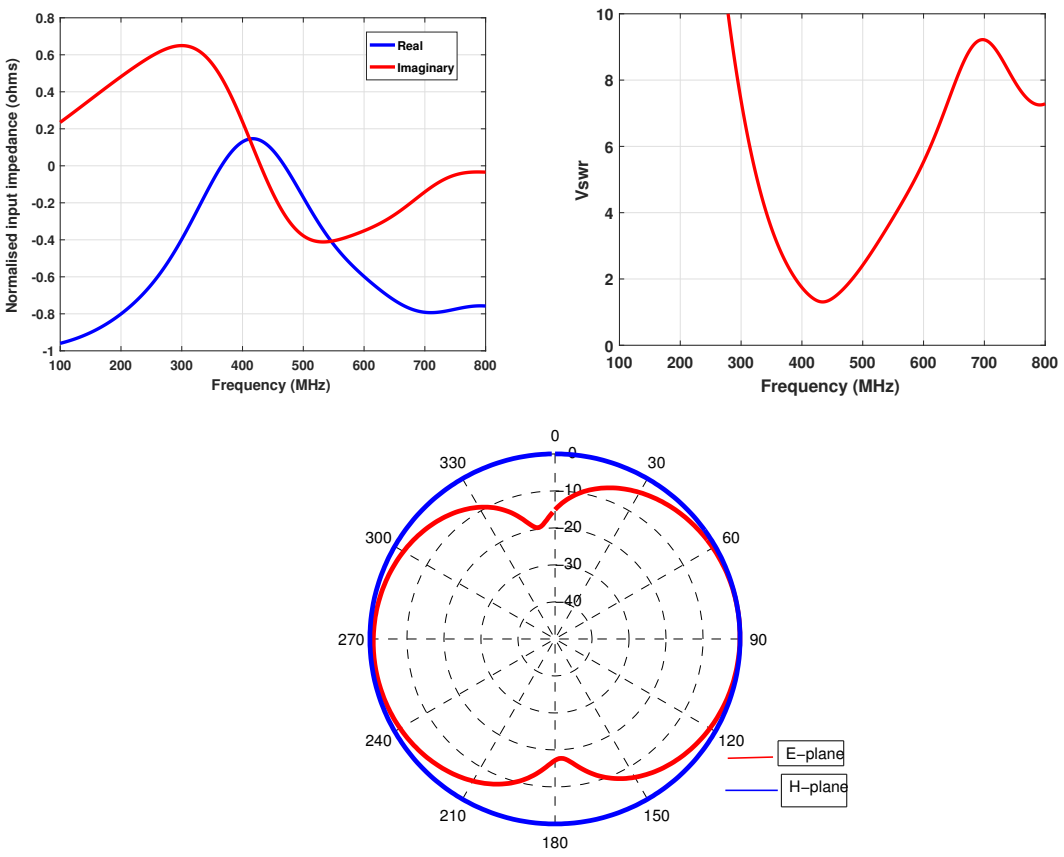


FIGURE 6.8: Other results of CS PIFA. Top (left) normalised input impedance, Vswr (top right), and (radiation pattern (bottom), red solid line in azimuth plane, and blue solid line in elevation plane)

TABLE 6.3: Comparisons of the two proposed implantable antennas

| Antenna | Tissue | $\varepsilon_r$ | $\sigma$ | $f_r$(MHz) | $S_{11}$ | -10 dB BW | Directivity |
|---|---|---|---|---|---|---|---|
| CC-PIFA | Muscle | 58.8 | 0.84 | 402 | -29.58 | 356.56-457.01 | 1.86 dBi |
| | Fat | 11.6 | 0.08 | 553 | -8.9 | - | |
| | Skin | 47.7 | 0.69 | 453 | -21.55 | - | |
| CS-PIFA | Muscle | 58.8 | 0.84 | 404 | -29.82 | 357.76-452.17 | 2.74 dBi |
| | Fat | 11.6 | 0.08 | 525 | -2.82 | - | |
| | Skin | 47.7 | 0.69 | 433 | -17.4 | 392.87-477.37 | |

## 6.3 Operation Principles of our CC and CS PIFA Designs

As has been described in the previous sections, the proposed implantable antennas are multi-layered structures with a lower and upper patch. Both patches are mirror image of each other. Naturally, both structures will resonate at certain point if deployed as individual elements without using our mirror image arrangement (i.e without orienting both patches in opposite direction). Here we show the $S_{11}$ results of CS PIFA (Refer to Fig. 6.9) with the lower and upper patch in the same orientation.

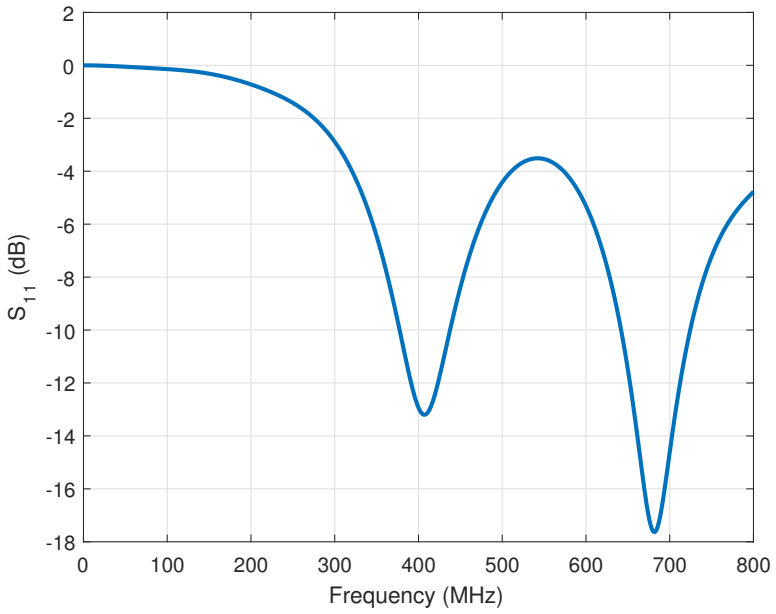


FIGURE 6.9: $S_{11}$ results for compact spiral PIFA with both lower and upper patches in the same orientation.

Fig. 6.10 shows the surface current contours and vector fields of both patches. After careful analysis of the surface current contours and vectors fields, it became apparent that by using mirror image arrangement the two patches were forced to act as a single element. Also it has been observed that by using the mirror image orientation approach, the surface currents of both patches flow in opposite directions just as for the CC PIFA (See Fig. 6.1 (f)), and also coupling to reinforce the two closely frequencies to overlap.

Furthermore, as has been shown in Fig. 6.10 (a) and (b), at each phase considered i.e 0° and 90°, the equipotential fields are on opposite sides on the outer arms of the patches, but with the same phase-shift. It follows that if radiators were considered as circuit elements, the inductive part balances the capacitive part, hence the structure working as a resonant element. It is also interesting to note that the vector fields diverge from the lower patch at 0° (See Fig. 6.10 (c)), and at 90° the fields on the upper patch begun to

converge Fig. 6.10 (d). We note that the shorting pin and high permittivity superstrate also contribute to the shift of the resonant frequency lower.

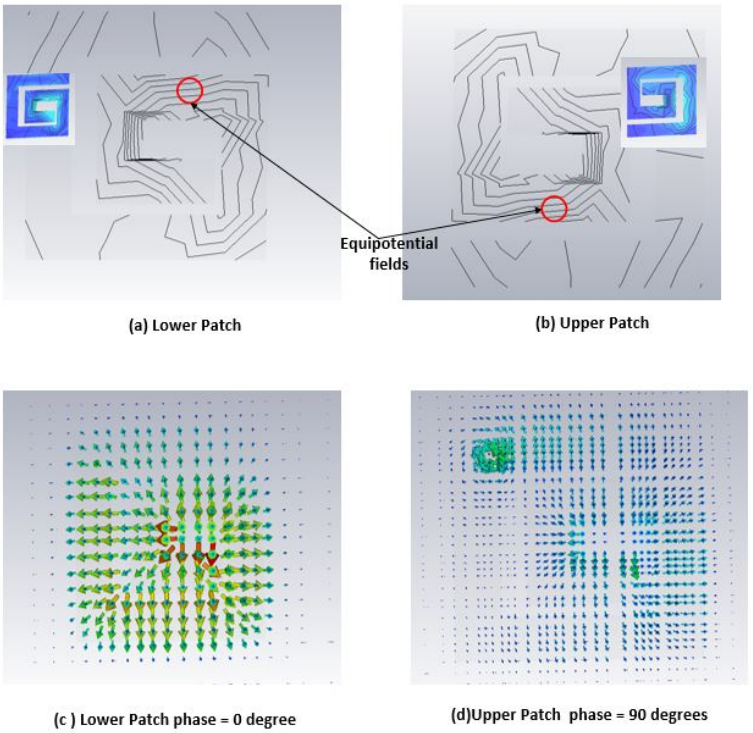


FIGURE 6.10: Surface current contours and vector fields of the Compact Spiral PIFA.

Fig. 6.11 shows the CS PIFA $S_{11}$ results comparing the two configurations of the radiators (i.e radiators arrange in the same direction, and radiators arranged using mirror image approach).

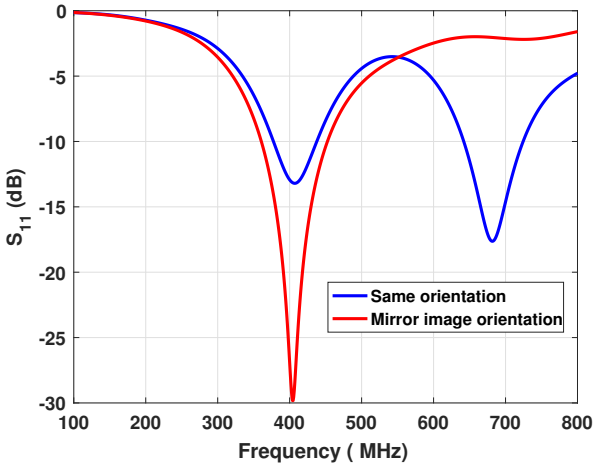


FIGURE 6.11: CS-PIFA $S_{11}$ results comparing the arrangements of the radiators (lower patch and upper patch). The results show the lower and upper patches in the same orientation and mirror image approach as described in the section.

## 6.4 Summary

In this chapter, two miniaturised implantable antennas have been presented. A literature review on implantable antennas highlighted the need of developing compact and conformal antennas, and understand their behaviour when placed in proximity of the human body. The chapter demonstrated miniaturisation techniques that involve; high permittivity substrate, multi-layered radiators, meandering and shoring pin to design implantable antennas. Two different structural configurations were studied i.e circular PIFA and spiral PIFA using the aforementioned techniques. The antennas were simulated in a human-mimicking phantom and numerically analysed for implantable communication. The results demonstrated that changes in position of the antenna in different tissues shift the resonant frequency.

The operation principles (mirror image approach) behind the designs have been explained. For this approach two radiators with the same dimensions and configuration, but different orientations were used. We explained that by using this approach, the radiators with closely resonance overlap to enhance the operational bandwidth. The initial findings demonstrate the potential suitability and usefulness of the underlying approach. The set of data and the design in this study could serve as a template for future studies of implantable antennas.

# References


[1] A. Kiourti, J. Costa, C. Fernandes, A. Santiago, and K. Nikita, "Miniature implantable antennas for biomedical telemetry: From simulation to realization," *Biomedical Engineering, IEEE Transactions on*, vol. 59, pp. 3140–3147, Nov 2012.

[2] W. Liu, S. Chen, and C. . Wu, "Implantable broadband circular stacked pifa antenna for biotelemetry communication," *Electromagnetic Waves and Applications*, vol. 22, no. 13, pp. 1791–1800, 2008.

[3] A. Kiourti and K. Nikita, "Miniature scalp-implantable antennas for telemetry in the mics and ism bands: Design, safety considerations and link budget analysis," *Antennas and Propagation, IEEE Transactions on*, vol. 60, pp. 3568–3575, Aug 2012.

[4] C. M. Lee, T. C. Yo, and C. H. Luo, "Compact broadband stacked implantable antenna for biotelemetry with medical devices," in *Wireless and Microwave Technology Conference, 2006. WAMICON '06. IEEE Annual*, pp. 1–4, Dec 2006.

[5] C. Wu, K. Wong, and W. Chen, "Slot-coupled meandered microstrip antenna for compact dual-frequency operation," *Electron Lett*, vol. 34, pp. 1047–1048, May 1998.

[6] K. Wong, C. Tang, and H. Chen, "A compact meandered circular microstrip antenna with a shorting pin," *Microwave Opt. Technol. Lett.*, vol. 15, pp. 147–149, June 1997.

[7] S. Dey and R. Mittra, "A compact microstrip patch antenna," *Microwave Opt. Technol. Lett.*, vol. 13, pp. 12–14, Sept. 1996.

[8] J. Lu, k. Wong, and H. Chen, "Slot-loaded, meandered rectangular microstrip antenna with compact dual-frequency operation," *Electron Lett*, vol. 34, pp. 1048–1050, May 1998.

[9] J. Dahele, K.-F. Lee, and D. Wong, "Dual-frequency stacked annular-ring microstrip antenna," *IEEE Trans. Antennas Propagat.*, vol. 35, pp. 1281–1285, Nov 1987.

[10] S. Long and M. Walton, "A dual-frequency stacked circular-disc antenna," *IEEE Trans. Antennas Propagat*, vol. 27, pp. 270–273, Mar 1979.

[11] J. Volakis, *Antenna Engineering Handbook*. McGraw-Hill, fourth ed., 2007.

[12] A. Kiourti, M. Christopoulou, and K. Nikita, "Performance of a novel miniature antenna implanted in the human head for wireless biotelemetry," pp. 392–395, July 2011.

[13] W. C. Liu, F. Yeh, and M. Ghavami, "Miniaturized implantable broadband antenna for biotelemetry communication," *Microwave and Optical Technology Letters*, vol. 50, pp. 2407–2409, Sept 2008.

[14] C. Lee, T. Yo, F. Huang, and C. Luo, "Rectenna application of miniaturized implantable antenna design for triple-band biotelemetry communication," *Antennas and Propagation, IEEE Transactions on*, vol. 59, pp. 2646–2653, July 2011.

[15] C. Lee, T. Yo, F. Huang, and C. Luo, "Bandwidth enhancement of planar inverted-f antenna for implant able biotelemetry," *Microwave and Optical Technology Letters*, vol. 51, pp. 749–752, March 2009.

[16] "url: http://maxwells-equations.com/materials/permittivity,"

[17] J. Kim and Y. Rahmat-Samii, "Implanted antennas inside a human body: simulations, designs, and characterizations," *Microwave Theory and Techniques, IEEE Transactions*, vol. 52, pp. 1934–1943, 2004.

[18] P. Soontornpipit, C. M. Furse, and C. Y. Chung, "Design of implantable microstrip antenna for communication with medical implants," *Microwave Theory and Techniques, IEEE Transaction*, vol. 52, pp. 1944–1951, 2004.

[19] A. Kiourti and K. Nikita, "A review of implantable patch antennas for biomedical telemetry: Challenges and solutions," *IEEE Antenna and Propagation Magazine*, vol. 54, pp. 210–228, June 2012.

[20] Y. Rahmat-Samii, "Wearable and implantable antennas in body-centric communications," in *Antennas and Propagation, 2007. EuCAP 2007. The Second European Conference on*, pp. 1–5, Nov 2007.

[21] C. Liu, Y. X. Guo, and S. Xiao, "Compact dual-band antenna for implantable devices," *IEEE Antennas and Wireless Propagation Letters*, vol. 11, pp. 1508–1511, 2012.

[22] L. Xu, Y. Guo, and W. Wu, "Dual-band implantable antenna with open-end slots on ground," *IEEE Antennas and Wireless Propagation Letters*, vol. 11, pp. 1564–1567, 2012.

# Chapter 7

# Conclusions and Future works

## 7.1 Summary

This thesis presented six new antenna designs for body-centric applications. The proposed antennas have been designed and simulated in free space and human body environments to assess their performance. The spectra covered for this study include the medical implant communication services band (MICS) of 402-405 MHz, the Industrial, Scientific and Medical band (ISM) 2.45 GHz and the Ultra Wideband (UWB) spectrum 3.1-10.6 GHz.

A printed rectangular monopole antenna (PRMA) with Q-slot for UWB spectrum with large bandwidth for on-body and microwave imaging applications has been presented and discussed. The wideband operation was achieved by etching a Q-slot on the antenna. Numerical investigations were carried out to analyse the design parameters of the antenna. The results presented in this study show that the proposed PRMA with Q-slot provides high immunity in close proximity to human body. The simulated and measured results were in reasonable agreement over the entire UWB spectrum band considered.

Two new compact spline-curve UWB antennas for microwave imaging were presented. UWB signal analysis in the presence of breast phantoms was carried out. In this study, it has been shown that the transmission and reception of UWB signals differ from phantom without tumor and with tumor. The changes in transient signal amplitudes suggest that the tumor signals could be distinguished with the use of an appropriate imaging algorithm.

A new printed monopole antenna designed for ISM band at 2.45 GHz has also been presented. A circular slot on the patch has been used to control the resonant frequency of the antenna. The size of the circular slot has an impact on the antenna performance as it distributes the surface current along the edges of the patch without degrading the antenna performance. The ground plane size also plays an important role as it affects the input the impedance of the antenna. We have also demonstrated a stable performance of the antenna in close proximity to human body.

Two new miniaturised implantable antennas have been proposed for biotelemetry. The study illustrates the advantages of using high permittivity substrate, meandering, stacking and shorting pins to miniaturise the proposed implantable antennas. The combined miniaturisation techniques reduce the size of the antenna to a fraction of the operating frequencies. All the antenna design parameters including the location of the feed and shorting pins had to be selected appropriately to optimise the design. The position of the antenna in the human tissue was crucial as deeper implantation in the muscle tissue, for example, led to further degradation of gain and efficiency to -47.8 dBi and 0.000283% respectively. The performance of implantable antennas within different body tissues has been demonstrated through this studies. It has been observed through this studies that the permittivity and conductivity of the tissues have effect on the resonance of the antenna. Furthermore, we had to trade-off the size of the antennas with those parameters such as efficiency and radiation patterns.

## 7.2 Key Contributions

The work in this thesis has introduced some novel antennas for body-centric applications. The major contributions to this work are :

(i) Six new antennas have been proposed, designed, simulated and four of those measured for body-centric applications. Parametric and numerical studies have been performed to investigate the effects of human body on the proposed antennas. We also provided the necessary guidelines for the designed antennas.

(ii) This work has also demonstrated the use of combined miniaturisation techniques (high permittivity substrates, meandering, stacking and shorting pins) to reduce the size of the antennas considerably. We have demonstrated the guidelines needed to reduce the size of the antennas at the given frequencies.

(iii) We studied two miniaturised implantable antennas for biotelemetry. Two different configurations were proposed for implantable devices. We have proposed a compact circular structure as well as spiral design for implantable devices. The operation principles and miniaturisation techniques have been explained for both designs. Furthermore, we studied the radiation characteristics of implantable antennas in body tissues. Operation in the presence of numerical phantom models has also been investigated presenting initial results for future works. The results could be extended further for system integration to model realistic scenarios.

We also characterised a narrowband antenna at 2.45 GHz for body-centric application. We have demonstrated the use of a circular slot to control the resonant

frequency of the proposed antenna as well as its input impedance. Based on this design concept a novel printed monoploe antenna was presented, fabricated and measured. The antenna was simply tuned to the required frequency by manipulating a circular slot on the radiator.

(iv) A simple PRMA with Q-slot for UWB spectrum has been proposed for on-body operation as well as possible application to microwave imaging for breast cancer. The antenna was designed to overcome the challenges of antenna detuning in the close proximity of human tissues. The presented work in the thesis shows that the proposed PRMA with Q-slot maintains high immunity in close proximity to the human body. We have also shown similar characteristics of the antenna in the presence of a breast phantom and matching liquids. The simulated and measured results agreed in all the cases.

(v) Two compact printed monopoles for UWB spectrum for microwave imaging have been proposed. The dimensions of both antennas measure 16 mm x 25 mm for imaging applications. This very small size suggests that these antennas can be used to image small volumes (e.g. small animal imaging), or can be integrated in an array with a large number of elements. The first antenna was designed to operate in the lower spectrum of UWB i.e from 3.1 GHz to 6 GHz. The second antenna was designed to cover the whole UWB spectrum as defined by FCC of U.S.A. The simulated and measured results agree for both antennas.

## 7.3 Future Work

The work presented in this thesis opens up many potential areas for further research. The millimetre wave frequency band has the advantages of a large bandwidth and small antennas with high gains. The are possibilities of reducing the size of the antenna in the high frequency millimetre wave band (e.g 60 GHz) which is desirable for ultra-small body-centric devices. Further studies on the miniaturisation and immunity of UWB antennas should be exploited. As has been demonstrated in the thesis, by using spline curves and slots, good time-domain performance can be realised even for small antennas.

Other major areas that could be exploited include:

(i) This study presented numerical artifacts of the proposed antennas. The results presented in the thesis are generic for on-body and imaging applications. The proposed antennas could be investigated further for different human test cases that may include system integration for specific cases like health, sports and military applications.

(ii) The efficiencies of the antennas could be investigated further by using meta-materials and techniques such as electromagnetic band gap (EBG) to reduce radiations towards the human body and minimise the detuning effect.

(iii) UWB antennas array have shown great potentials for imaging applications. In this study, we used fewer antenna elements in our simulations and measurements. As has been shown in the thesis the coupling between the antenna elements is very low which suggests that more UWB antenna array could be optimised and deployed for farfield imaging applications such as through-wall and ground penetrating radar.

# Appendix A

# Computer Simulation Technology(CST) software

The software CST is a a general purpose electromagnetic simulator based on the Finite integral Technique (FIT)[1]. This numerical method provides universal spatial discretisation scheme applicable to various electromagnetic problems ranging from static field calculations to high frequency applications in time or frequency domain.

The main aspects of the procedures involve are explained in the Fig.A.1 Unlike most numerical methods such as FDTD, FIT discretises the integral form of Maxwell's equations than the differential ones. To solve these equations numerically, you must define a calculation domain, enclosing the application problem. A suitable mesh system splits this domain into many small elements or grid cells. The spatial discretisation of Maxwell's equations is performed where degree of freedom are introduced as integral value.

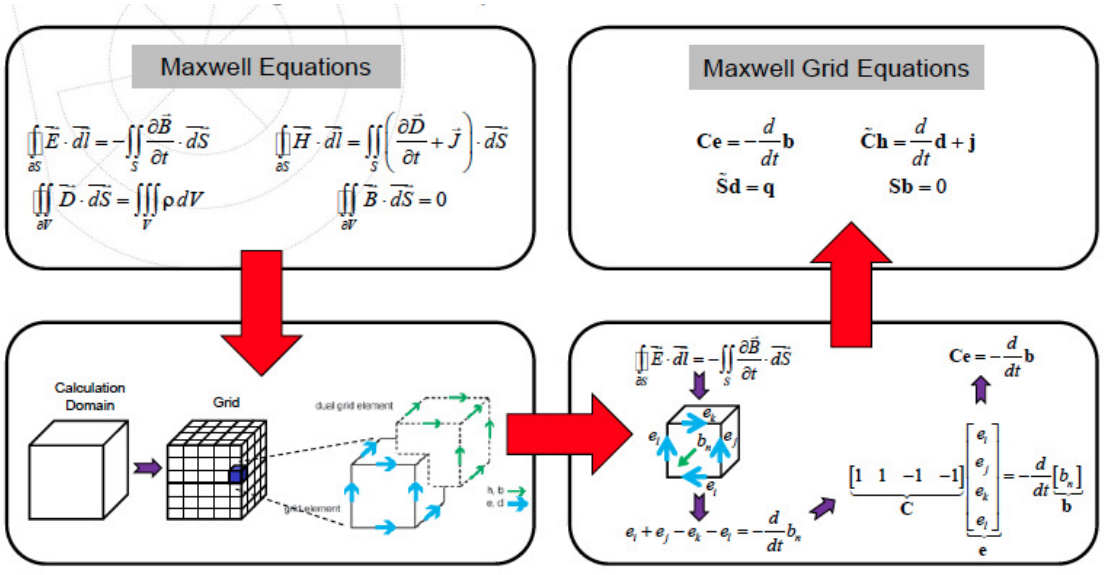


FIGURE A.1: Procedures of CST Simulator

[1]This technique was first proposed by Weiland in 1976/1977

Considering Faraday's Law, the closed integral on the left side of the equation can be rewritten as the sum of four grid voltages **e** without introducing any supplementary errors. Consequently, the time derivative of the magnetic flux defined on the enclosed primary cell facets represents the right -hand side of the equation shown in Fig.A.1.Repeating the procedure for all cell facets summarises the calculation in the matrix formulation , introducing the topological matrix **C** as the discrete equivalent of he analytical curl operator. Apply this scheme to Ampere's Law on the dual grid involves the definition of a corresponding curl operator $\tilde{\mathbf{C}}$ shown in top right of Fig.A.1 i.e Maxwell grid equations.

In defining the necessary voltages and fluxes , their integral values have to be approximated over the edges and cell areas respectively .Consequently,the resulting coefficients depend on the average material parameters as well as the spatial resolution of the grid shown Fig.A.2

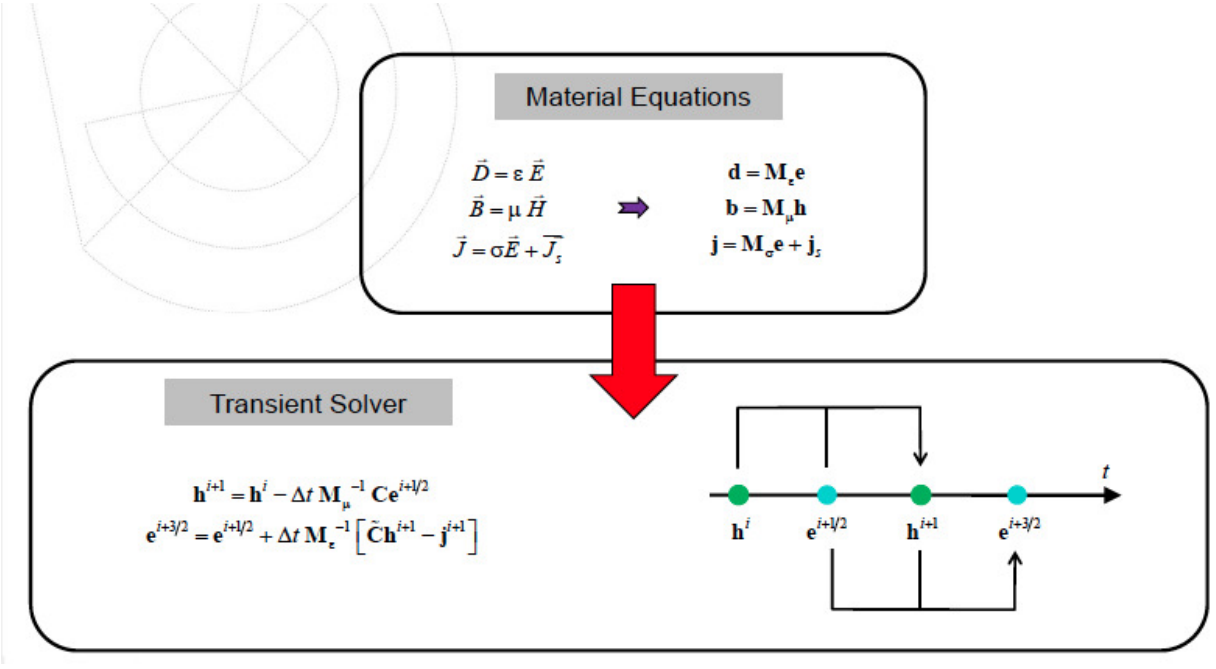


FIGURE A.2: Material Equations

Regarding the above relations , calculation variables are given by electric voltages and magnetic fluxes .Both types of unknown are located alternatively in time , as in well-known leapfrog shown in Fig.A.2. The stability limit for the time step $\Delta t$ is given by Courant-Friedrich-Levy (CFL) criterion which has to be fulfilled by every mesh cell or grid.

$$\Delta t \leq \frac{\sqrt{\varepsilon \mu}}{\sqrt{(\frac{1}{\Delta x})^2 + (\frac{1}{\Delta y})^2 + (\frac{1}{\Delta x})^2}}$$

# Appendix B

# Fabricated Antennas

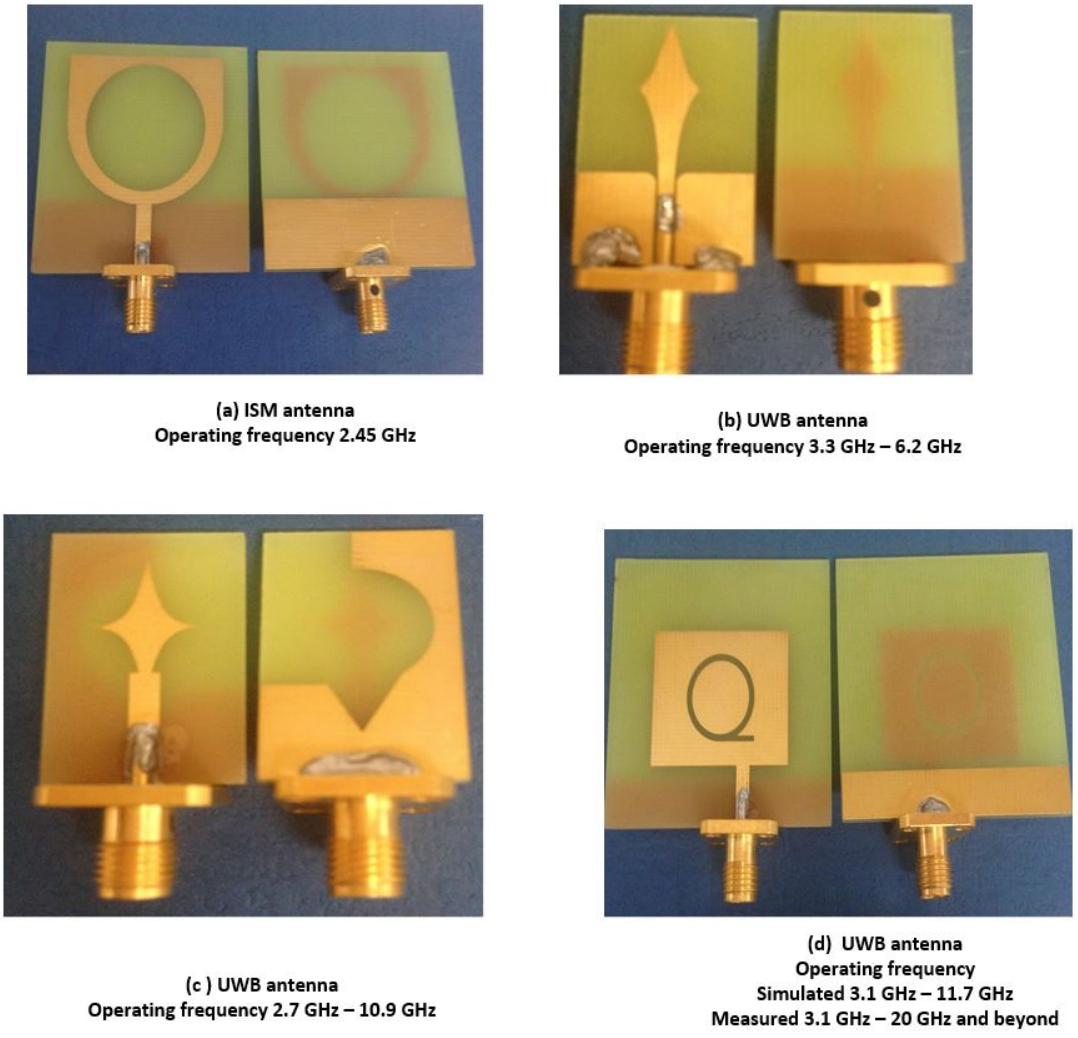


FIGURE B.1: Fabricated antennas for body-centric applications.

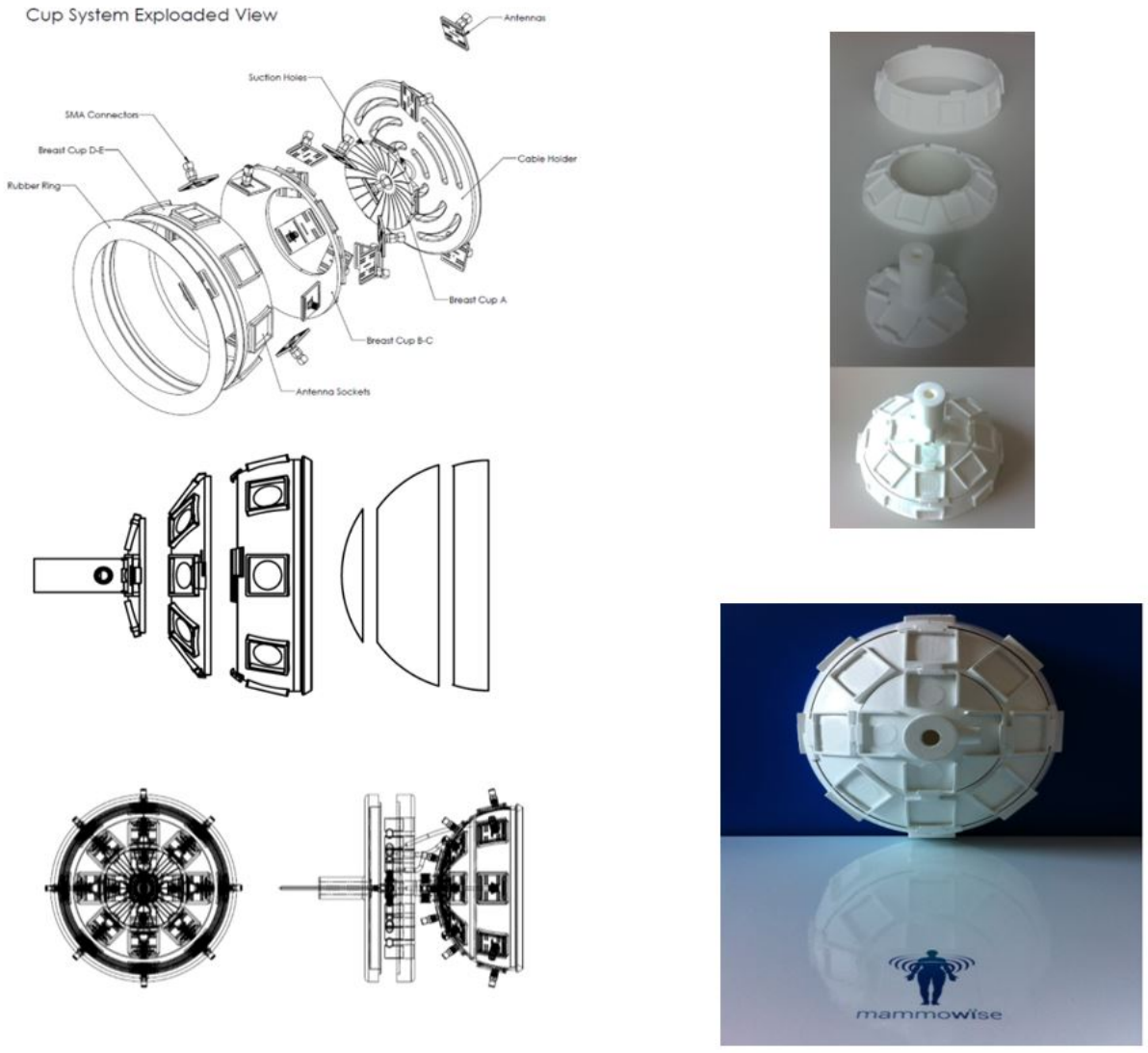


FIGURE B.2: Future integration system for breast cancer using the proposed antennas. The system was designed by the team from MediWise UK